UNIVERSITY OF SAO PAULO

Institute of Physics

Department of Materials Physics and Mechanics

Molecular modeling study of pristine and thermally modified ZIF-8: applications on carbon capture

Matheus Finamor

Advisor: Prof. Dr. Caetano Rodrigues Miranda

São Paulo – SP

2023

Universidade de São Paulo
Instituto de Física

Modelagem molecular de ZIF-8 pristina e modificada termicamente: aplicações para captura de carbono

Matheus Finamor

Orientador: Prof. Dr. Caetano Rodrigues Miranda

Dissertação de mestrado apresentada ao Instituto de Física da Universidade de São Paulo, como requisito parcial para a obtenção do título de Mestre(a) em Ciências.

Banca Examinadora:
Prof. Dr. Caetano Rodrigues Miranda - Orientador (IFUSP)
Profa. Dra. Liane Marcia Rossi (IQUSP)
Prof. Dr. Alexandre Fontes da Fonseca (IFGW – UNICAMP)

São Paulo
2023

FICHA CATALOGRÁFICA
Preparada pelo Serviço de Biblioteca e Informação
do Instituto de Física da Universidade de São Paulo

Finamor, Matheus

Molecular modeling study of pristine and thermally modified ZIF-8: applications on carbon capture / Modelagem molecular de ZIF-8 pristina e modificada termicamente: aplicações para captura de carbono. São Paulo, 2023.

Dissertação (Mestrado) - Universidade de São Paulo. Instituto de Física. Depto. de Física dos Materiais e Mecânica.

Orientador: Prof. Dr. Caetano Rodrigues de Miranda.

Área de Concentração: Simulações Computacionais e Modelagem Molecular.

Unitermos: 1. Física computacional; 2. Carbono; 3. Modelagem computacional.

USP/IF/SBI-097/2023

University of São Paulo
Institute of Physics

Molecular modeling study of pristine and thermally modified ZIF-8: applications on carbon capture

Matheus Finamor

Advisor: Prof. Dr. Caetano Rodrigues Miranda

Dissertation submitted to the Institute of Physics of the University of São Paulo in partial fulfillment of the requirements for the degree of Master of Science.

Examining Committee:
Prof. Dr. Caetano Rodrigues Miranda - Supervisor (University of São Paulo)
Profa. Dra. Liane Marcia Rossi (IQUSP)
Prof. Dr. Alexandre Fontes da Fonseca (IFGW – UNICAMP)

São Paulo
2023

Acknowledgments

This work was possible and financed with the support of CNPq and the Research Centre for Gas Innovation, sponsored by FAPESP (2020/15230-5) and Shell Brasil.

I would like to thank my advisor for the opportunity and all the support through these two years. Thank you, Caetano.

I extend these greetings to all the members of the SAMPA Research Group for the discussions, suggestions, and coffees. In particular, thank you, Carlos, Henrique, Matheus, and Dani, for the very helpful conversations.

I cannot forget to thank all the friends that helped make these years more bearable. In São Paulo, Campinas, Bragança, or any country mountain, thank you, F, Will, Pedro, Renata, and Luca.

Thank you to all my family for all the strengthening and hard effort that let me come this far. Thank you Luigi, Lê, Ana, Lucas, Pai, Mirella, and Mãe.

Last, but most. Thank you, Camilla, for everything.

Però a vent'anni già mi chiedo se son troppo stanco.

Måneskin

Resumo

Nesse trabalho estudamos Estruturas Metal-Orgânicas (MOFs, do inglês Metal-Organic Frameworks) como um novo material capaz de capturar dióxido de carbono (CO_2) eficientemente. Essas estruturas são muito promissoras quanto à captura de carbono devido à sua grande área de superfície, tamanho de poro ajustável e um alto potencial de escalabilidade à nível industrial. Em particular, estudamos uma MOF específica, a Estrutura Zeolítica de Imidazolato 8 (ZIF-8, do inglês Zeolitic Imidazolate Framework 8) composta por zinco coordenado com imidazol, estruturado como uma sodalita. Através de cálculos de primeiros princípios baseados na Teoria do Funcional da Densidade (DFT), utilizando um funcional com correções não locais de van der Waals, optB86b, investigamos a adsorção de CO_2 na ZIF-8, identificando diferentes sítios e as respectivas energias de adsorção. Além disso, por meio de simulações atomísticas, utilizando Monte Carlo no ensemble Grã Canônico, foi calculado a seletividade de carbono considerando reservatórios com diferentes misturas em diferentes concentrações e condições termodinâmicas. Ademais, recentes resultados experimentais indicam que o tratamento térmico da ZIF-8 pode aumentar a sua capacidade de captura de carbono. Assim, modelamos proposições de como os defeitos são induzidos por esses tratamentos e estudamos suas estabilidades e impactos na adsorção. Nossos resultados indicam que os tratamentos térmicos perto de 900 °C podem aumentar a captura de carbono de 15 a 18.5 vezes a adsorção de ZIF-8 pristino. Sendo assim, esses tratamentos podem designar a ZIF-8 tratada como um adequado material a ser usado em membranas de matrizes mistas, permitindo um design de membrana que seja eficiente e economicamente viável para captura de carbono.

Palavras-chave: Estruturas Metal-Orgânicas; Estruturas Zeolíticas de Imidazolato; ZIF-8; Tratamento Térmico; Captura de Carbono

Abstract

In this work, we study Metal-Organic Frameworks (MOFs) as a new material able to capture CO_2 efficiently. These frameworks are promising regarding carbon capture due to high surface areas, tunable pore size, and a high potential for industrial-scale production. In particular, we study a specific MOF, the Zeolitic Imidazolate Framework 8 (ZIF-8), composed of zinc coordinated with imidazole, structured in a sodalite framework. Through first-principles calculations based on the Density Functional Theory (DFT) using a functional with nonlocal van der Waals correction, the optB86b, we investigate CO_2 adsorption in ZIF-8 by identifying different adsorption sites and their respective adsorption energy. Furthermore, using atomistic simulations based on Grand Canonical Monte Carlo, the selectivity of carbon considering reservoirs with different mixtures at distinct concentrations and thermodynamic conditions was calculated. Moreover, recent experimental findings indicate that thermal post-treatment of ZIF-8 can enhance its carbon capture capability. Therefore, we modeled propositions of possible defects induced by this kind of treatment and study their stability and how they affect adsorption. Our results indicate that thermal treatments near 900 °C can enhance carbon capture up to 15 to 18.5 times the CO_2 uptake of pristine ZIF-8. Since thermal treatments are cheap and easy to be scaled, these treatments can designate ZIF-8 treated as a proper filler to be used in mixed-matrix membranes, enabling a membrane design that can be efficient and economically viable to capture carbon.

Keywords: Metal-Organic Frameworks; Zeolitic Imidazolate Frameworks; ZIF-8; Thermal treatment; Carbon capture

List of Figures

List of Tables

List of Abbreviations

BM	Birch-Murnagham
BO	Born-Oppenheimer
CBMC	Configurational Bias Monte Carlo
CCS	Carbon Capture and Storage
DDEC	Density-derived Electrostatic and Chemical charge method
DFT	Density Functional Theory
EOS	Equation of State
FF	Force Field
GCMC	Grand Canonical Monte Carlo
GGA	Generalized Gradient Approximation
HK	Hohenberg-Kohn
IAST	Ideal Adsorbed Solution Theory
KS	Kohn-Sham
LAMMPS	Large-scale Atomic/Molecular Massively Parallel Simulator
LAPW	Linear Augmentend-plane-wave
LDA	Local Density Approximation
LJ	Lennard-Jones
MC	Monte Carlo
MD	Molecular Dynamics
MOF	Metal-Organic Framework
MSD	Mean Squared Displacement
PAW	Projector-augmented-wave
PBC	Periodic Boundary Conditions
PDOS	Projected Density of States
PPPM	Particle-particle Particle-mesh
RV	Rose-Vinet
RMSE	Root mean squared error
UFF	Universal Force Field

USPP	Ultrasoft Pseudopotentials
VASP	Vienna Ab initio Simulation Package
vdW	van der Waals
ZIF	Zeolitic Imidazolate Framework

List of Symbols

$\hat{H}$	Hamiltonian of the many-body problem
$\hat{T}$	Kinetic operator
$\hat{V}$	Potential energy operator considering electron-nuclei interactions
$\hat{U}$	Potential energy operator considering electron-electron interactions
$\|\Psi\rangle$	Eigenstate of the many-body problem
ε	Eigenvalue of the many-body problem
A	Quantum observable operator
m	Mass
$\hbar$	Reduced Planck's Constant
$\mathbf{r}_i$	Coordinate of electron i
q	Charge
Q_k	Charge of nuclei k
$\mathbf{R}_k$	Coordinates of nuclei k
U	Potential energy for electron-electron interaction
ν	Potential energy for electron-nuclei interaction
$\mathbf{\Psi}$	Wave function
n	Particle density
E	Energy functional
F	Universal functional from HK theorem
F_{KS}	Kohn-Sham functional
T_s	Kinetic energy functional for noninteracting particles
E_{xc}	Exchange and correlation energy functional
ϕ_i	Kohm-Sham orbitals
e	Fundamental charge
ν_s	Noninteracting particles local potential
ν_H	Hartree potential energy
ν_{xc}	Exchange-correlation energy
ϵ_{xc}^{hom}	Exchange-correlation energy of a homogeneous gas of electrons
$E_{\text{disp}}^{\text{D2}}$	Dispersion energy at the $D2$ level of correction

s_6	Global parameter
$C_{6,AB}$	Empirical atomic coefficients
R_{AB}	Distance between atoms A and B
$f_{\text{dump}}^{\text{D2}}$	Dumping function for short-range interactions
$R_{0,AB}$	Sum of the vdW radii of atoms A and B
E_c^{nl}	Nonlocal term for the correlation functional
$\mathcal{T}$	Linear transformation mapping real wave into auxiliary functions
$\mathcal{T}_R$	Linear transformation acting only in an augmented region R
$\|\tilde{\mathbf{\Psi}}\rangle$	Smooth auxiliary wave function
$\|\varphi_i\rangle$	Solution of the Schrödinger's equation for the isolated atom
$\|\tilde{\varphi}_i\rangle$	Auxiliary partial wave function
$\|\mathbf{\Psi^1}\rangle$	Wave function exact in the augmented region and zero outside of it
$\|\tilde{\mathbf{\Psi}}^{\mathbf{1}}\rangle$	Wave function smooth, identical to $\|\tilde{\mathbf{\Psi}}\rangle$ in R and to $\|\mathbf{\Psi^1}\rangle$ outside
η	Relation between volume and volume of equilibrium
E_0	Energy at the volume of equilibrium
B_0	Bulk modulus
B_0'	Derivative of the bulk modulus in relation to pressure
E_{ads}	Adsorption energy
$\mathcal{U}$	Total interaction energy
σ_{ij}	LJ parameter for Collision diameter
ϵ_{ij}	LJ parameter for well depth
N	Number of atoms in the system
$\mathbf{r}^N$	Atomic coordinates
k_B	Boltzmann constant
T	Temperature
β	Thermodynamic beta, inverse of k_BT
$\mathcal{A}$	Statistical observable
$\mathcal{H}$	Hamiltonian from statistical mechanics
$\mathcal{N}$	State distribution
N_{steps}	Number of stems in MC
$\pi(o \to n)$	Transition probability from state o to n
$\alpha(o \to n)$	Probability of occuring transition from state o to n
$\text{acc}(o \to n)$	Probability of accepting transition from state o to n
V	Volume
P	Pressure
μ	Chemical potential
Q	Heat

Λ	Thermal de Broglie wavelength
μ^{ex}	Excess chemical potential
$\mathcal{V}_{\text{test}}$	Potential energy after adding test particle
N_{ex}	Excess number of moleclues adsorbed
N_{abs}	Absolute number of molecules adsorbed
ρ_{bulk}	Density at bulk phase
V_{free}	Free volume
L	Amount adsorbed
M	Plateau of adsorption
K	Energy of adsorption
S_{ij}	Selectivity of species i over j
x_i	Molar fraction of species i in the adsorbed phase
y_i	Molar fraction of species i in the gas phase
$\mathbf{F_i}$	Forces on particle i
$\mathbf{v}$	Velocity
t	Time
D	Self-diffusion coefficient

Contents

1 Introduction

1.1 Climate Change

Human activity drastically impacted the average global surface temperature as stated by the Sixth Assessment Report by the Working Group I of the International Panel on Climate Change (IPCC) reporting the physical understanding of the climate system and climate change [1]. Figure 1.1a shows that the temperature change averaged annually observed and simulated using human and natural drivers agree. Moreover, scenarios considering only natural drivers were conducted and agreed with the changes in temperature of the pre-industrial era, indicating that human activity has influenced global warming [1]

By 2020 we reached a relative increase of 1.3 °C in relation to the temperature simulated using only natural drivers [1]. Impacts on natural and human systems have already been observed and are very concerning, including sea level rise, species loss and extinction in several ecosystems, and risks to food security and water supply, among many other consequences. With global warming exceeding 1.5 °C these impacts might be long-lasting or irreversible [2]. Thus, strategies for reverting these increases and mitigating climate change are urgent.

Figure 1.1b shows the contributions of individual components in the temperature change relative to 1850-1900 using an assessment of radiative forcing and climate sensitivity. Emissions of greenhouse gases, aerosols and their precursors, land-use changes, and aviation contrails are represented. Carbon dioxide is considered one of the main responsible, with an increase reaching almost 1.0 °C. Besides being one of the principal greenhouse gas component, its concentration in the atmosphere keeps increasing due to fossil fuel burning. It is also interesting to stress that methane is another concerning component with a significant increase. Contrarily, some components contribute to a decrease in the global surface temperature, such as nitrogen oxides and sulphur dioxides [1]. Given this anthropocenic contribution, it is evident that we need to look for ways to mitigate this issue.

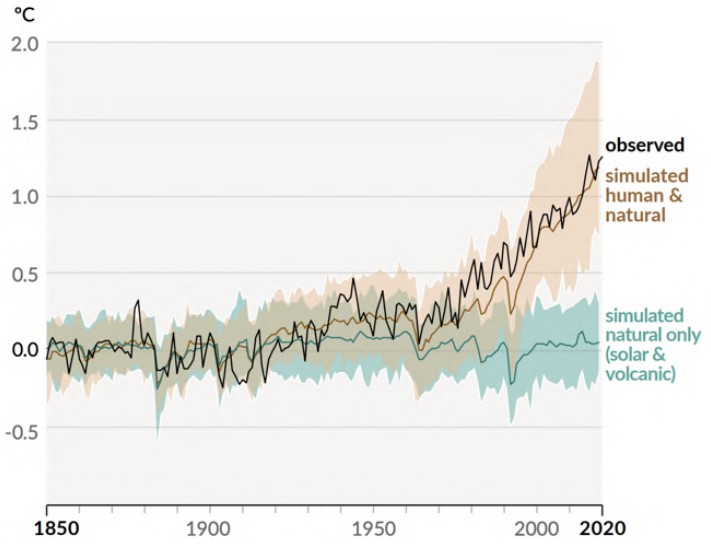

(a)

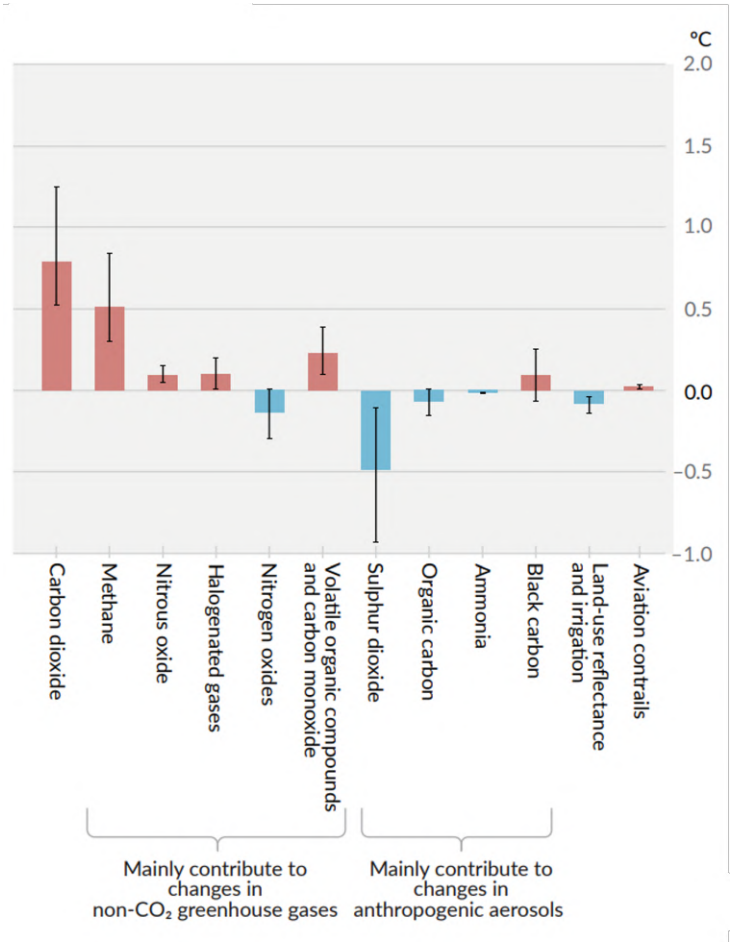

(b)

Figure 1.1: (a) Change in global surface temperature from 1850 to 2020 observed (black line) and simulated using human and natural drivers (brown line) and only natural drivers (green line). Solid lines represent the average, and colored shades show the very likely range of simulations. (b) Temperature changes relative to 1850-1900 from individual components of human influence taken from the assessment of radiative forcing and climate sensitivity. Images from [3].

1.2 Carbon Capture and Storage

With carbon dioxide being the most threatening component, one of the most relevant mitigation strategies is Carbon Capture and Storage (CCS). The idea is to capture carbon at power plants or industrial facilities before it reaches the atmosphere and then transport and store it in long-term. Figure 1.2 illustrates the process schematically which is also discussed below [4].

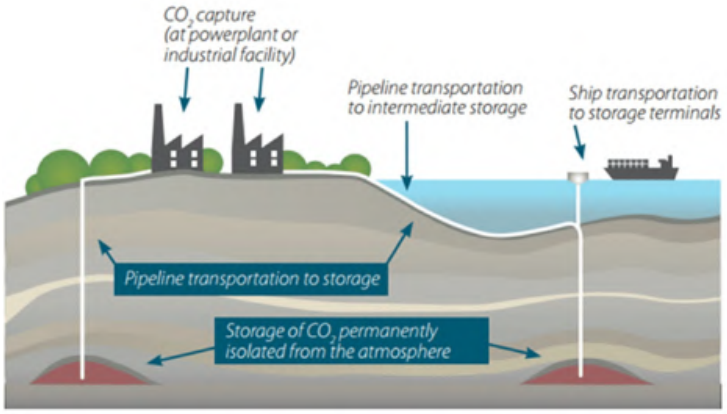

Figure 1.2: Illustration of Carbon Capture and Storage. Carbon is captured before entering the atmosphere at power plants or industrial facilities. Then it is transported to geological formations or the ocean, where it can be stored. Image from [5].

Regarding carbon capture, there are three approaches to the problem: post-combustion capture systems, pre-combustion capture systems, and oxy-fuel capture systems [6]. Nowadays, cryogenic distillation, pressure swing adsorption, and chemical absorption techniques are the most common technologies used for gas separations. However, these methods rely on high energy-dependent processes. Hence, a transition toward alternative low-energy methods implies reducing the carbon footprint of current operations.

For gas separation, one alternative method is using membranes technologies that rely on differences in diffusion and sorption coefficients to separate different species [7, 8, 9]. Concerning transport of CO_2, it is well established; it can be done by pipelines, ships, or tanker trucks. Pipelines are considered to be the most efficient for transporting high loads of CO_2 [10].

As for carbon storage it can be done in geological formations, oceans, or through a mineralization process. Examples of storage options are oil and gas reservoirs, saline aquifers, and unmineable coal seams. In these formations, we can also use carbon in enhanced oil/gas recovery and enhanced coal bed methane recovery. Store CO_2 in oceans consists of injecting the gas at great depths where it dissolves or forms hydrates or heavier-than-water plumes that sinks at the bottom of the ocean. Despite having a great storage capacity, increasing CO_2 concentration in the oceans can have serious environmental

impacts on marine biodiversity [11]. Meanwhile, mineralization processes are related to converting CO_2 to solid inorganic carbonates; it offers permanent and safe storage of CO_2, but with a high-cost procedure [11].

This work focuses on post-combustion capture systems, where CO_2 needs to be separated and captured from flue gas. The challenges are related to the low concentration of CO_2 and the high concentration of N_2 in the flue gas. Different separation technologies can be applied to separate CO_2 from N_2. To capture carbon from the post-combustion flue gas the market is dominated by amine adsorption [12]. Although, due to amine toxicity and the challenges related to scaling this method at larger plants, there is space for a less costly energetic transition using membrane methods. To be economically competitive with amine absorption, membranes with a permeance of 1000–5000 GPU and a selectivity of 30–50 must be achieved [13]. Usually, polymer and zeolite-based membranes are used. However, alternative materials are being explored to overcome challenges related to achieving this performance.

1.3 Metal-Organic Frameworks

As stated, there is an extensive search for promising materials to capture and separate carbon from flue gas. Metal-Organic Frameworks (MOFs) is a very promising class of material for gas separation. MOFs consists in a porous structure with very good durability and resistance, presenting outstanding performing indexes for capturing and separating carbon [14].

MOFs are composed of metals coordinated with organic linkers in a crystalline structure, as Figure 1.3 indicates. It is possible to grow different MOFs with distinct properties by changing the metals or the organic linkers. In particular, there is a specific class of MOF called Zeolitic Imidazolate Frameworks (ZIFs) composed of M-Im-M, where M is a metallic cation and Im is the imidazolate organic linker (variations of this organic linker can also be used). As the name suggests, these materials are topologically isomorph to zeolites, aluminosilicate materials commonly used as adsorbents. It has great mechanical and chemical stability with a high surface area, becoming a very promising material to capture carbon from the adsorption process [15].

Especially the ZIF-8 has been very explored in the literature [15, 17, 18]. With several advances regarding the synthesis and characterization of this material, together with a very good capability of adsorbing and selecting CO_2 from other gases, it becomes a high-potential material for CO_2 capture [17]. It is composed of zinc with 2-methyl-imidazole, forming a sodalite structure, as Figure 1.4 illustrates. It also shows a capability of scaling up the production at industrial levels due to easy and cheap synthesis methods [18].

Two approaches might be considered when using MOFs in end application devices for gas separation. Thin-film MOF-based membranes can be used, or MOFs can be fillers

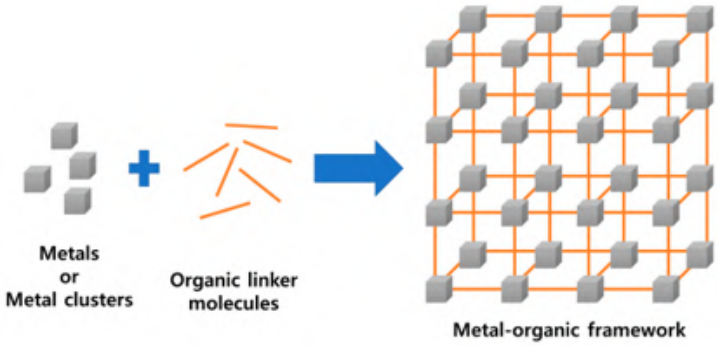

Figure 1.3: Illustration of a Metal-Organic Framework indicating how the metals and organic linkers are coordinated to build a crystalline structure. Figure adapted from [16].

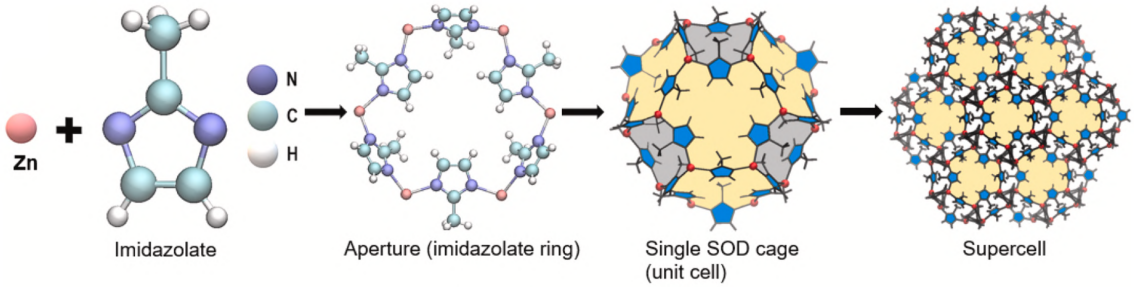

Figure 1.4: Illustration of ZIF-8 indicating its components, the pore aperture, the sodalite unit cell, and a supercell. Figure adapted from [19].

in Mixed-Matrix Membranes. Figure 1.5 illustrates both possibilities. Since thin-film MOF-based membranes are hard and more expensive to synthesize, using MOFs as fillers in Mixed-Matrix Membranes is more suggestive. The idea is to have a polymer-based membrane with nanoparticles dispersed to increase its durability, resistance, selectivity, and permeability [7, 8, 9].

It is also interesting to remark that MOFs have several other applications than gas capture and separation. It can be used in drug delivery mechanisms [20], in agriculture [21], as catalysts, and as sensors [22].

1.4 State of the Art and Contributions

In this work, our main objective is related to investigating ZIF-8 as a potential material to capture and select carbon from the flue gas. There is a vast literature that comprehends to the synthesis of ZIF-8 to experimental and simulation results in the adsorption and transport of greenhouse gases [8].

On the modeling, it comprehends first-principles calculations such as Density Function Theory (DFT), and also atomistic simulations such as Monte Carlo and Molecular Dynamics. A recent study explores the adsorption and transport of greenhouse gases in ZIF-8 using the DFT [23]. However, the functional employed only considers empirical corrections for

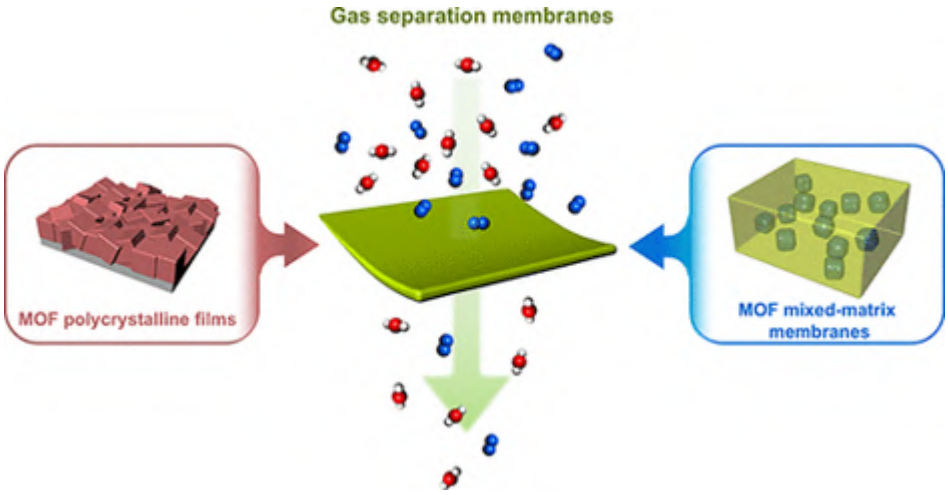

Figure 1.5: Illustration of MOF-based membranes for gas separation. MOF-based membranes can be constructed based on MOF's polycrystalline films or in mixed-matrix membranes. Figure adapted from [7]

.

dispersion energies. Thus, we contribute by systematically studying the framework and its interactions with guest molecules using a non-local functional to get a more fundamental description of van der Waals interactions. Moreover, results from DFT can be used to validate the classical force fields used in atomistic simulations.

Regarding molecular simulations, several force fields are reported to describe adsorption [24, 25, 26] and transport [27, 28, 29, 30] properties with outstanding accuracy, being able to reproduce experimental results [31, 32]. Using this well-established methodology, one of our contributions is related to obtaining the selectivity of ZIF-8 for distinct mixtures of greenhouse gases with N_2. We define selectivity as usual, using the following equation:

$$S_{ij} = \frac{x_i}{x_j}\frac{y_j}{y_i}, \tag{1.1}$$

where S_{ij} is the selectivity of species i over j, x_i is the molar fraction of the species i in the adsorbed phase, and y_i is the molar fraction of the species i in the gas phase.

Furthermore, experimental results indicate enhancement in CO_2 capture for thermally treated ZIF-8 [33]. Gadipelli et al. investigate an enhancement in CO_2 uptake and selectivity over N_2 treating ZIF-8 samples in a range of temperature from 400 °C to 600 °C. They report an increase in the CO_2 uptake that reaches about two times the adsorption of pristine ZIF-8 using treatments near 525 °C. As for the selectivity, the highest increase was observed for treatments near 500 °C, where they report a selectivity of 34 compared with 10 for pristine ZIF-8. Moreover, thermal gravimetric analysis results indicate that the sample starts to decompose/carbonize near 580 °C. Thus, they justify this huge increases by samples treated just below this carbonization temperature considering that it creates local defects from partial dissociation of the rotationally free methyl groups on the framework and partly broken coordination between Zn-N bonds, as Figure 1.6a shows.

Wang et al. [34] also details an investigation on thermal treatments on a controlled atmosphere, ranging from 500 °C to 900 °C. Results from Zn L-edge and Zn K-edge X-ray absorption spectroscopy reveal that tetrahedral ZnN_4 centers transform to porphyrin-like ZnN_4 centers, i.e., Zn and N are now coordinated in a plane, as Figure 1.6b illustrates.

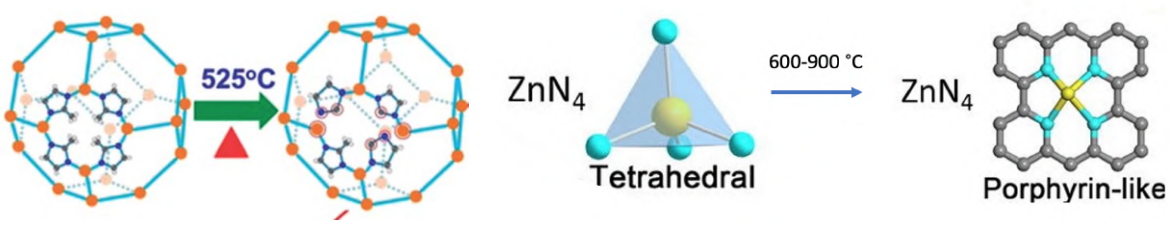

(a) (b)

Figure 1.6: Schematic of structures induced by thermal treatments. (a) Indicates the methyl vacancies induced by thermal treatments near 525 °C. Image adapted from [33]. (b) Shows the transformation of tetrahedral ZnN_4 to porphyrin-like centers. Image adapted from [34].

To the best of our knowledge, simulations using proposed models of these thermally treated frameworks have not been yet fully explored. Therefore, we contributed by modeling ZIF-8 with methyl vacancies and planar porphyrin-like structures as experimentally suggested by Gadipelli et al. and Wang et al. [33, 34]. With these models, we determine CO_2 adsorption in these frameworks to explain the enhancement in CO_2 capture. In that way, we aim to contribute to this extensive searching for proper materials to capture carbon to achieve a net zero and carbon-neutral economy.

This dissertation is organized as follows: In the next chapter, the theoretical foundations of the Density Functional Theory (DFT) are explored, followed by a discussion on atomistic simulations using Monte Carlo and Molecular Dynamics. Afterwards, we explain how DFT and atomistic simulations will be used to explore the systems of interest of this work, detailing what calculations have been done and how they were done. Subsequently, we present the results obtained for pristine ZIF-8 regarding adsorption and transport properties. Next, the models proposed for thermally treated ZIF-8 are presented together with results for CO_2 adsorption within these structures. Finally, we conclude and present possible future perspectives for extensions of the study.

2 | First-principles Calculations

In this chapter we explore the theoretical foundations of the Density Functional Theory, one of the methodologies used in this work to explore pristine and thermally modified ZIF-8.

2.1 Density Functional Theory

In first-principles, also called *ab initio*, calculations, the idea is to solve the problem using the most fundamental description. Thus, to solve the system considering the quantum mechanics formulation. In other words, to solve the Schrödinger's equation to obtain the ground and possible excited states of the system [35, 36, 37]. Usually, in a first approximation, nuclear positions are considered fixed, and the influence in the electronic structure is given as a potential depending only on electronic coordinates. This is known as the Born-Oppenheimer (BO) or the adiabatic approximation [38]. Considering this within a nonrelativistic approach, the time-independent Schrödinger's equation for the electronic structure is given by:

$$\hat{H}\,|\Psi\rangle = (\hat{T} + \hat{V} + \hat{U})\,|\Psi\rangle = \varepsilon\,|\Psi\rangle\,, \tag{2.1}$$

where $\hat{H}$ is the Hamiltonian of the system that can be decomposed on the following three operators: $\hat{T}$ for the kinetic energy of the electrons, $\hat{V}$ for potential energy considering the electrons-nuclei interactions, and $\hat{U}$ for the potential energy considering electrons-electrons interactions. $|\Psi\rangle$ is the eigenstate, and ε are the eigenvalues that solve the equation, giving the allowed energies of the system.

Given $|\Psi\rangle$, obtained by solving the equation, it is possible to obtain any physical observables (e.g., position, momentum, and particle density) by taking the expectation values of the observable operator $\hat{A}$ with the eigenstate as follows:

$$\langle\Psi|\hat{A}|\Psi\rangle\,. \tag{2.2}$$

The kinetic operator shown in Equation 2.1 projected into the space basis can be written as:

$$\hat{T} = -\frac{\hbar^2}{2m}\sum_i \nabla_i^2, \tag{2.3}$$

where $\hbar$ is the reduced Planck's constant, m is the mass of the electron, and ∇_i represents the derivative with respect to the coordinates of electron i. The electron-electron interaction projected into the space basis, considering a Coulombic system, is given by:

$$\hat{U} = \sum_{i<j} U(\boldsymbol{r}_i, \boldsymbol{r}_j) = \sum_{i<j} \frac{q^2}{|\boldsymbol{r}_i - \boldsymbol{r}_j|}, \tag{2.4}$$

where q is the charge of the electron and $\boldsymbol{r}_i$ is the coordinate of electron i. Considering the BO approximation, the electron-nuclei interaction term can be decoupled and written in the space basis:

$$\hat{V} = \sum_i \nu(\boldsymbol{r}_i) = \sum_{ik} \frac{Q_k q}{|\boldsymbol{r}_i - \boldsymbol{R}_k|}, \tag{2.5}$$

where Q_k is the charge of the nuclei and $\boldsymbol{R}_k$ the respective coordinates. Therefore, the Schrödinger's equation projected into the space basis will be given as:

$$\left[\sum_i \left(-\frac{\hbar^2}{2m}\nabla_i^2 + \nu(\boldsymbol{r}_i)\right) + \sum_{i<j} U(\boldsymbol{r}_i, \boldsymbol{r}_j)\right] \boldsymbol{\Psi}(\boldsymbol{r}_1, \boldsymbol{r}_2, \ldots, \boldsymbol{r}_n) = \varepsilon \boldsymbol{\Psi}(\boldsymbol{r}_1, \boldsymbol{r}_2, \ldots, \boldsymbol{r}_n). \tag{2.6}$$

One can see that this is a complex many-body problem, consequently, hard to solve. Hartree-Fock [39], Diagrammatic perturbation theory [40], and configuration interaction (CI) [41] are some powerful methods to deal with this problem. However, they are usually very computationally demanding. Most methods scale nominally as N^4 (N being a relative measure of the system size related to the number of particles in the system).

The DFT, as proposed by Kohn and Sham [42], brings a new approach to the problem based on mapping the many-body problem onto many single-body problems. In DFT, based in the Kohn-Sham theorems and equations, the fundamental object is the total electron density $n(\boldsymbol{r})$ instead of the electron wave function $\boldsymbol{\Psi}(\boldsymbol{r}_1, \boldsymbol{r}_2, \ldots, \boldsymbol{r}_n)$. So the Schrödinger equation for N electrons changes from a dependent wave function of $3N$ variables to be written as an electron density equation with only three variables. The scaling factor is N^3, considerably reducing the computational cost depending on the system studied. It is possible to obtain the wave functions from the density and, consequently, any other observable. This can be done exactly as a theory, but in practice, DFT can only be used with approximations, depending on the functionals employed [35, 36, 37].

2.1.1 Hohenberg-Kohn Theorems

Hohenberg-Kohn (HK) theorems must be introduced to ensure that the particle density can be used and that it is possible to map the many-body problem onto single-body problems [43].

The first HK theorem implies that the ground state particle density ($n(\boldsymbol{r})$) determines the external potential $\nu(\boldsymbol{r})$ uniquely less than an additive constant. This means that the external potential is a functional of the density, written as $\nu[n(\boldsymbol{r})]$. This first theorem implies that the Hamiltonian is entirely determined less than an additive constant. All the wave functions are also determined for all states. Lastly, all properties of the system can be determined by the density.

The second HK theorem states that an energy functional can be defined ($E[n(\boldsymbol{r})]$) in a way that the energy of the ground state is exactly the minimum value of this functional. The definition of the energy functional is given by:

$$E[n(\boldsymbol{r})] = \int \nu(\boldsymbol{r}) n(\boldsymbol{r}) d\boldsymbol{r} + F[n(\boldsymbol{r})], \tag{2.7}$$

where $F[n(\boldsymbol{r})]$ is a universal functional independent from $\nu(\boldsymbol{r})$ and including all terms of kinetic and potential energy:

$$F[n(\boldsymbol{r})] = \langle \Psi | \hat{T} + \hat{U} | \Psi \rangle = T[n(\boldsymbol{r})] + U[n(\boldsymbol{r})]. \tag{2.8}$$

This theorem implies that obtaining the density and exact energies from the ground state is possible if the HK functional is known. This functional determines the properties of the ground state. The proofs of the theorems were originally given in [43].

2.1.2 Kohn-Sham Equations

According to the HK theorems, if the functional form of the energy that needs to be minimized to obtain the ground state properties is know, we can obtain any other desirable observable. However, this functional form depends on an universal functional $F[n(\boldsymbol{r})]$ that, so far, does not have a known analytical form.

Kohn and Sham (KS) [42] proposed a way to describe this functional, considering an auxiliary system with noninteracting particles to describe the real system with interacting particles. This auxiliary system has the same density as the original one, and the wave functions of the particles from this auxiliary system will be described as $\phi_i(\boldsymbol{r})$, the Kohn-Sham orbitals. The functional proposed by Kohn and Sham is written as follows:

$$F_{KS}[n(\boldsymbol{r})] = \frac{e^2}{2} \iint \frac{n(\boldsymbol{r}) n(\boldsymbol{r'})}{|\boldsymbol{r} - \boldsymbol{r'}|} d\boldsymbol{r} d\boldsymbol{r'} + T_s[n(\boldsymbol{r})] + E_{xc}[n(\boldsymbol{r})], \tag{2.9}$$

where the first term corresponds to the coulombic electron-electron interactions (also

known as Hartree term), $T_s[n(\boldsymbol{r})]$ is the functional for the kinetic energy of a system with noninteracting particles with density $n(\boldsymbol{r})$ (the subscript s stands for single-particle), and $E_{xc}[n(\boldsymbol{r})]$ is the energy functional for the exchange and correlation terms, which includes all the effects for the many-body problem.

This expression is formally exact, but an analytical form of the exchange-correlation functional is unknown. The following section is going to discuss approximations for this functional. For now, however, lets continue by assuming that it is possible to calculate the exchange-correlation. The kinetic energy functional can be written in terms of the wave functions of the noninteracting particles:

$$T_s[n(\boldsymbol{r})] = -\frac{\hbar^2}{2m}\sum_i \int \phi_i^*(\boldsymbol{r})\nabla^2\phi_i(\boldsymbol{r}), \tag{2.10}$$

then, using this proposed universal functional, the energy functional would be:

$$E[n(\boldsymbol{r})] = \int \nu(\boldsymbol{r})n(\boldsymbol{r})d\boldsymbol{r} + \frac{e^2}{2}\iint \frac{n(\boldsymbol{r})n(\boldsymbol{r'})}{|\boldsymbol{r}-\boldsymbol{r'}|}d\boldsymbol{r}d\boldsymbol{r'} + T_s[n(\boldsymbol{r})] + E_{xc}[n(\boldsymbol{r})], \tag{2.11}$$

minimizing this functional holding the constrain that the number of electrons in the system must be equal to $N = \int n(\boldsymbol{r})d\boldsymbol{r}$ we obtain the Kohn-Sham equations which are equivalent to solving the Schrödinger equation for those noninteracting particles under a local potential $\nu_s(\boldsymbol{r})$:

$$\left[-\frac{\hbar^2\nabla^2}{2m} + \nu_s(\boldsymbol{r})\right]\phi_i(\boldsymbol{r}) = \varepsilon_i\phi_i(\boldsymbol{r}), \tag{2.12}$$

$$\nu_s(\boldsymbol{r}) = \nu(\boldsymbol{r}) + \nu_H(\boldsymbol{r}) + \nu_{xc}(\boldsymbol{r}), \tag{2.13}$$

where $\nu(\boldsymbol{r})$ is the external potential, $\nu_H(\boldsymbol{r}) = e^2\int \frac{n(\boldsymbol{r'})}{|\boldsymbol{r}-\boldsymbol{r'}|}d\boldsymbol{r'}$ is the Hartree potential energy , and $\nu_{xc}(\boldsymbol{r}) = \frac{\delta E_{xc}}{\delta n}$ is the exchange-correlation energy.

The idea, as illustrated in Figure 2.1 is: given an initial density $n^{(0)}(\boldsymbol{r})$, the effective potential ν_s is constructed and then solves the KS self-consistently to get the KS orbitals and then a new density $n^{(1)}(\boldsymbol{r})$, repeating the process until a convergence criterion is reached. Obtaining, in the end, the electronic density $n(\boldsymbol{r})$ that will describe the physical system.

The wave functions and the energies from this noninteracting system are said to have a semi-quantitative value. Although in principle, they should not have a physical meaning since it is just an equivalent system, the eigenvalues can be interpreted as an approximation of order zero to obtain the energy spectra, while the eigenfunctions can be interpreted as auxiliary functions to obtain the density of states or as approximations of order zero to

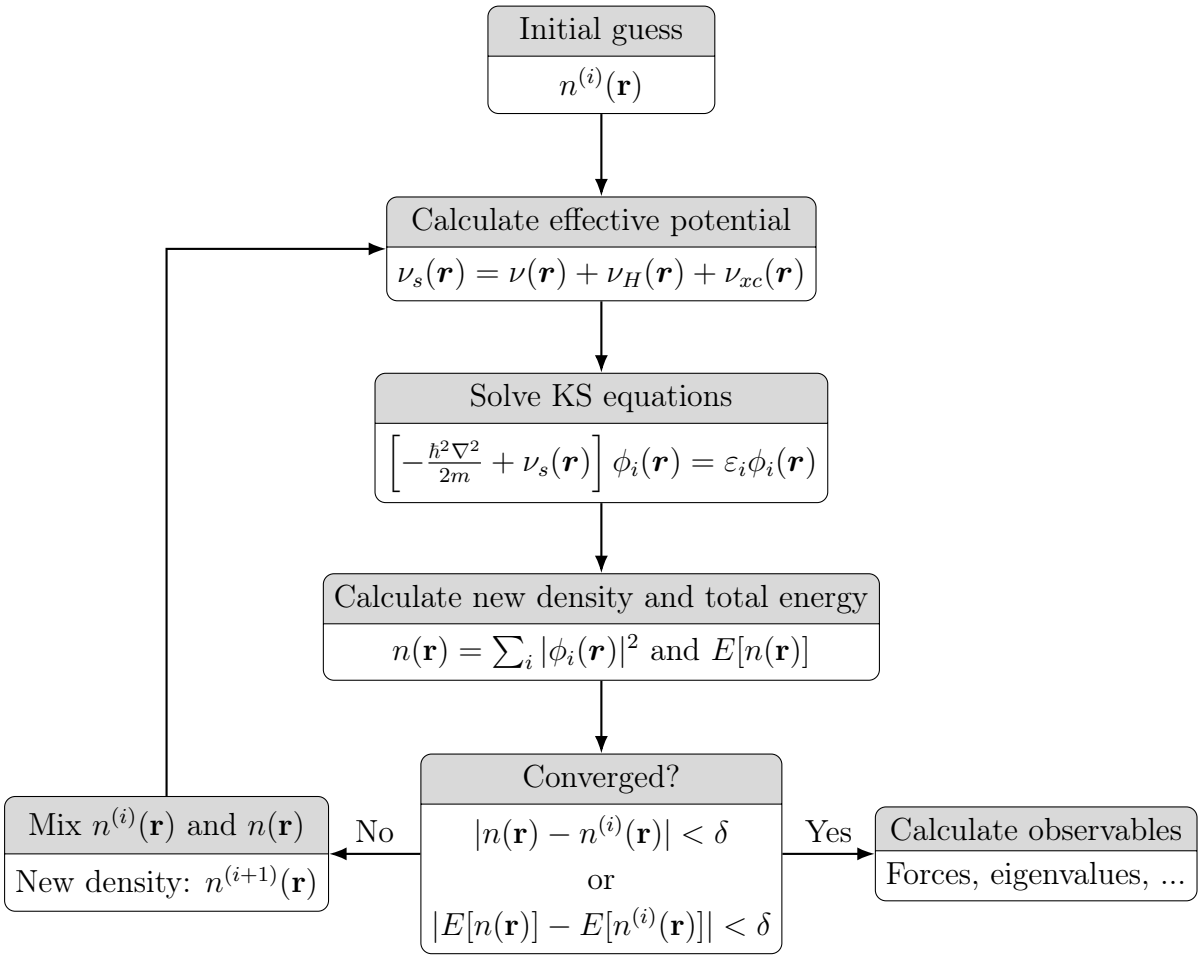

Figure 2.1: Flowchart of KS Self-consistent cycles.

the quasi-particle functions [42].

It is important to remark that this theory can be generalized to consider spin effects considering two different densities for each spin: $n_\uparrow(\boldsymbol{r})$ and $n_\downarrow(\boldsymbol{r})$. Solving both sets of Kohn-Sham equations for each spin self-consistently allows us to calculate these densities.

2.1.3 Exchange-correlation Approximations

The last section assumed that the exchange-correlation energy could be calculated to obtain the Kohn-Sham equations. However, a universal analytical form is not known for this energy, enforcing the use of approximations. Here it will be discussed the two most commons approximations used: Local Density Approximation (LDA) and Generalized Gradient Approximation (GGA).

Local Density Approximation

The idea of the LDA approximation is consider an infinitesimal volume of the system. The functional E_{xc} on this volume can be treated as the energy of exchange and correlation from a homogeneous gas of electrons with the same local density as the original system [44, 45]:

$$E_{xc}^{\mathrm{LDA}}[n(\boldsymbol{r})] = \int n(\boldsymbol{r})\epsilon_{xc}^{hom}(n)d\boldsymbol{r}, \tag{2.14}$$

where $\epsilon_{xc}^{hom}(n)$ is the exchange and correlation energy, in the infinitesimal volume, of a homogeneous gas of electrons with density n. The exchange part of this term can be calculated exactly. For the correlation part, an analytical function is not known. However, there are approximations made by very accurate simulations using quantum Monte-Carlo [46].

This approximation is expected to work in systems where the electronic density slowly varies. It yields useful results for many crystalline systems, predicting several properties of these systems. Generally, it underestimates total energies and bond lengths or lattice parameters, while bond or cohesive energies are overestimated. However, usually, for molecular systems, the LDA approximation is not suitable since molecular systems tend to have more inhomogeneity in electron density (spartial) and also polarizabilities effects [35].

Generalized Gradient Approximation

The GGA approximation will also consider the rate of variation of the density in the infinitesimal volume. The first attempt was to expand the density in gradients, but it did not show to be efficient. Hence general functions of the density were introduced. The exchange-correlation functional will be written as:

$$E_{xc}^{\mathrm{GGA}}[n(\boldsymbol{r})] = \int n(\boldsymbol{r})\epsilon_{xc}^{hom}(n(\boldsymbol{r}), \nabla n(\boldsymbol{r}))d\boldsymbol{r}, \tag{2.15}$$

where now ϵ_{xc}^{hom} can be a general function of the density $n(\boldsymbol{r})$ and its gradient $\nabla n(\boldsymbol{r})$. There are different GGAs functionals employed in the literature. It can be based on non-empirical or empirical assumptions. Non-empirical uses restrictions and limits from quantum mechanics to correct parameters, whereas empirical uses a test set to correct the parameters. One of the most common GGA's functional is the PBE, which is non-empirical [47].

Hybrid functionals can also be used. It generally mixes a fraction of the exchange term calculated from exact theories (like Hartree-Fock) with GGA approximations. Some examples are B3LYP [48, 49, 50, 51] and PBE0 [52].

2.1.4 Nonlocal Corrections

So far, the approximations discussed for the exchange-correlation energy only considered the semi-local nature of electron density, in a sense that it only considers approximations of a local density or the gradient of the density locally. Interactions that can happen within a long-range (not local) are not considered. Thus, the "standard" DFT approximation does not describe van der Waals (vdW) dispersion interactions very well since they are nonlocal forces in nature.

The first correction level would be to consider empirical corrections (known as DFT-D, the D for dispersion) to the system's total energy. A more accurate description contemplate nonlocal corrections in the correlation functional. These two levels of corrections will be discussed further.

Empirical Corrections: DFT-D

At this level of correction, the idea is simply adding an empirical dispersion-type contribution to total energy within the Kohn-Sham energy to calculate the final energy of the system [53, 54]:

$$E_{\text{DFT-D}} = E_{\text{DFT-KS}} + E_{\text{disp}}. \tag{2.16}$$

This dispersion energy can be calculated at different levels. The first one is called $D2$, where the dispersion energy is given as [55]:

$$E_{\text{disp}}^{\text{D2}} = -s_6 \sum_{A} \sum_{B<A} \left(\frac{C_{6,AB}}{R_{AB}^6} f_{\text{dump}}^{\text{D2}}(R_{AB}) \right), \tag{2.17}$$

where s_6 is a global parameter that can be optimized for each functional used, R_{AB} is the distance between atoms A and B, $C_{6,AB}$ are empirical atomic coefficients, and $f_{\text{dump}}^{\text{D2}}$ is a

dumping function for short-range interactions given by:

$$f_{\text{dump}}^{\text{D2}}(R_{AB}) = [1 + e^{-d(R_{AB}/R_{0,AB}-1)}]^{-1} \tag{2.18}$$

where $R_{0,AB}$ is the sum of the vdW radii of atoms A and B, and d is an additional parameter that can be optimized.

These corrections can get more complex, such as $D3$, where a new term C_8 is considered, with new dumping functions and more parameters [56]. There are also modifications of these corrections in the literature [57]. Despite being a very fast correction in calculations, it depends on empirical parameters.

Nonlocal Correlation Functionals

A more sophisticated description can be made considering nonlocal corrections in the correlation part of the functional. In this case, the correlation functional has an additional nonlocal term described by:

$$E_c^{nl}[n(\boldsymbol{r})] = \int \nu_c^{nl}(\boldsymbol{r}) n(\boldsymbol{r}) d\boldsymbol{r} = \iint n(\boldsymbol{r}) f(\boldsymbol{r}, \boldsymbol{r'}) n(\boldsymbol{r'}) d\boldsymbol{r} d\boldsymbol{r'} \tag{2.19}$$

where $f(\boldsymbol{r}, \boldsymbol{r'})$ is the vdW kernel, with a not known analytical function. Hence, approximations must also be made to consider these corrections.

Dion et al. [58] proposed a promising method based directly on the electronic density of these approximations. It considers a LDA approximation for the correlation functional and a GGA approximation for the exchange functional. More details on the functional used will be explored further. The exchange-correlation functional is given by:

$$E_{xc}[n(\boldsymbol{r})] = E_x^{\text{GGA}}[n(\boldsymbol{r})] + E_c^{\text{LDA}}[n(\boldsymbol{r})] + E_c^{nl}[n(\boldsymbol{r})] \tag{2.20}$$

where the general function $f(\boldsymbol{r}, \boldsymbol{r'})$ from Equation 2.19 depends on $\boldsymbol{r} - \boldsymbol{r'}$ and on the neighborhoods of the density at $\boldsymbol{r}$ and $\boldsymbol{r'}$, this considers only pair interactions.

Despite not depending on empirical parameters, this functional presents a low accuracy compared to other methods. This low accuracy is due to the exchange functional used, which overestimates equilibrium distances and intramolecular energies [35, 36, 37]. Klimes et al. [59] and Hamada [60] proposed optimizations to the exchange functional in order to the vdW functional describes satisfactorily different studied systems.

In this work we opted to use the optB86b-vdW functional, a nonlocal correlation functional developed by Klimes et al. [59]. The choice of the exchange functional in Equation 2.20 was widely explored in the literature. Using the original revPBE led to too large intermolecular binding distances and inaccurate binding energies [61]. Klimes et al. proposed an optimized version to address these problems using the optB86b exchange functional, with an outstanding performance for a wide range of systems with a systematic

improvement in cohesive properties [59]. We also chose this functional due to the experience of our research group with this functional, where other works were developed exploring the interaction of greenhouse gases with several nanostructures using DFT and nonlocal functionals.

More accurate descriptions can be made considering hybrid functionals along with nonlocal corrections or even nonlocal interactions such as many-body interactions. However, these descriptions are out of the scope of this work.

2.1.5 Basis and Projector-augmented-wave formalism

It is necessary to choose basis functions to solve the Kohn-Sham equations (Equations 2.12). Different options, such as plane waves or localized atomic orbitals, might be used. In this work, we chose plane waves since it forms a complete set and are ideal for describing wave functions for a crystal (Bloch's theorem). However, many functions are necessary to get a good description of the oscillations near atomic nuclei, making calculus very expensive in terms of computational cost. In practice, due to computational limitations, a cutoff energy is chosen so that all plane waves with kinetic energy smaller than this cutoff are included in the basis.

Instead of considering the dynamics of core electrons, an effective potential is considered to approximate the system, called a pseudopotential approximation [62]. Different types are reported in the literature, such as norm-conserving [63] or ultrasoft pseudopotentials[1] [64].

In this work, the projector-augmented-wave (PAW) formalism was used [65]. It is a generalization of ultrasoft pseudopotentials (USPP) and the linear augmented-plane-wave (LAPW) [66] method. The LAPW method is an approximation based on solving the Kohn-Sham equations subject to periodic conditions that treat core and valence electrons differently. The PAW method consists in mapping the real wave functions into auxiliary functions that are numerically useful. This linear transformation $\mathcal{T}$ is written using Dirac's notation:

$$|\mathbf{\Psi_n}\rangle = \mathcal{T}\,|\tilde{\mathbf{\Psi}}_\mathbf{n}\rangle\,, \tag{2.21}$$

where $|\mathbf{\Psi}\rangle$ are the real wave functions, $|\tilde{\mathbf{\Psi}}\rangle$ the smooth auxiliary functions, and the subscripts are related to the state of the particle. The linear transformation $\mathcal{T}$ must modify the auxiliary function in each atomic region to have the correct nodal structure. Thus, it must differ from the identity to a sum of local contributions in atomic sites R such as:

[1]Despite the high computational cost, calculations can also be done without the pseudopotential approximations. These are all-electron calculations.

$$\mathcal{T} = 1 + \sum_R \mathcal{T}_R. \tag{2.22}$$

For each atom, $\mathcal{T}_R$ adds a difference between the real and auxiliary functions acting only in an augmented region. Outside these regions, the auxiliary and real functions are the same. $\mathcal{T}_R$ is defined in each region in terms of $|\varphi_i\rangle$, solutions of the Schrödinger's equation for the isolated atom and includes only valence states that are orthogonal to core states:

$$|\varphi_i\rangle = (1 + \mathcal{T}_R)\,|\tilde{\varphi}_i\rangle\,, \quad \text{with} \quad \mathcal{T}_R\,|\tilde{\varphi}_i\rangle = |\varphi_i\rangle - |\tilde{\varphi}_i\rangle\,, \tag{2.23}$$

where $|\tilde{\varphi}_i\rangle$ is an auxiliary partial wave function that outside the augmentation region must be equal to $|\varphi_i\rangle$ and inside it can be any smooth continuation.

Inside each augmented region, each auxiliary wave function might be expanded in terms of partial auxiliary wave functions:

$$|\tilde{\mathbf{\Psi}}\rangle = \sum_i c_i\,|\tilde{\varphi}_i\rangle\,, \tag{2.24}$$

which means the real wave function can be obtained through:

$$|\mathbf{\Psi}\rangle = \mathcal{T}\,|\tilde{\mathbf{\Psi}}\rangle = \sum_i c_i\,|\varphi_i\rangle\,, \tag{2.25}$$

with identical coefficients. Then, the wave function can be written as:

$$|\mathbf{\Psi}\rangle = |\tilde{\mathbf{\Psi}}\rangle - \sum_i c_i\,|\tilde{\varphi}_i\rangle + \sum_i c_i\,|\varphi_i\rangle\,. \tag{2.26}$$

Considering a set of projectors into the basis given by $|p_i\rangle$ the coefficients might be given as

$$c_i = \langle p_i|\tilde{\mathbf{\Psi}}\rangle\,. \tag{2.27}$$

Thus, the real wave function can be written, finally, as:

$$|\mathbf{\Psi}\rangle = |\tilde{\mathbf{\Psi}}\rangle + \sum_R (|\mathbf{\Psi^1_R}\rangle - |\tilde{\mathbf{\Psi}}\mathbf{^1_R}\rangle), \tag{2.28}$$

where:

$$|\mathbf{\Psi^1_R}\rangle = \sum_i |\varphi_i\rangle\,\langle p_i|\tilde{\mathbf{\Psi}}\rangle\,, \tag{2.29}$$

$$|\tilde{\mathbf{\Psi}}\mathbf{^1_R}\rangle = \sum_i |\tilde{\varphi}_i\rangle\,\langle p_i|\tilde{\mathbf{\Psi}}\rangle\,. \tag{2.30}$$

It is possible to understand, from Equation 2.28, that the real wave function is decomposed in terms of a combination of three wave functions. $|\tilde{\Psi}\rangle$ is smooth in the augmented region and exact out of it. $|\Psi^1\rangle$ is exact in the augmented region and goes to zero outside of it. And finally, $|\tilde{\Psi}^1\rangle$ is smooth in the region, being identical to $|\tilde{\Psi}\rangle$ in the region and to $|\Psi^1\rangle$ outside of it.

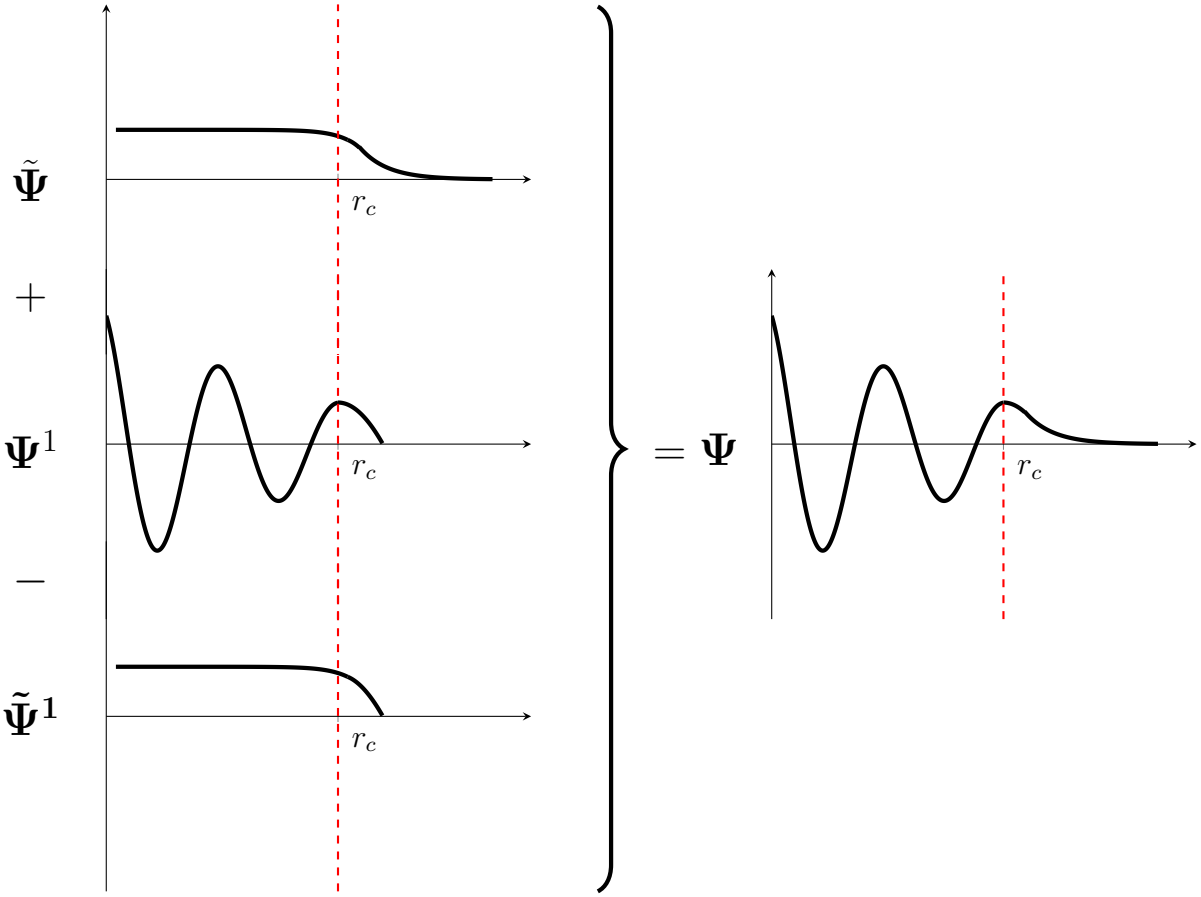

Figure 2.2: PAW auxiliary wave functions illustration indicating how each function behaves inside and outside the augmented region and how they sum up to the real wave function.

Therefore, DFT is a very powerful method and it will be used to explore electronic properties together with a systematic exploration of the interaction between greenhouse gases with ZIF-8. To the best of our knowledge, ZIF-8 and its interaction with guest molecules have only been explored with DFT using empirical corrections to account for vdW interactions [23]. We used a nonlocal correlation functional developed by Klimes et al., [59] advancing in the understading of carbon capture with MOFs. In the following section we explore the computational implementation and the parameters used in our calculations.

2.2 Computational Implementation

DFT calculations were performed using the Vienna Ab initio Simulation Package (VASP) [67, 68]. It uses a plane wave basis set together with the PAW method for pseudopotentials. It is a widely used and very efficient package to perform DFT calculations in several systems.

We opted to use the usual electronic configuration for each atomic species. This approximation was stressed out testing harder pseudopotentials where no significant changes were observed. The electronic configuration is as following for each atomic specie: Zn: [Ar] d10 p2, N: [He] s2 p3, C: [He] s2 p2, H: s1, O: [He] s2 p4.

Calculations were performed using the PAW method with the nonlocal optB86b-vdW functional [59]. Periodic boundary conditions were considered in all directions. A converged cutoff energy of 440 eV was considered. The convergence criteria were chosen to be 10^{-6} eV and 0.01 eV Å^{-1} for the self-consistency cycles and structural optimizations, respectively.

For pristine ZIF-8 and ZIF-8 with methyl vacancies a $2 \times 2 \times 2$ k-point sampling in the Brillouin zone obtained with the Monkhorst-Pack grid. It is important to remark that these conditions were tested and were sufficient to guarantee convergence in energy (tests with a larger sample yields very similar results within our accuracy). For the projected density of states (PDOS) calculations, it was necessary an $8 \times 8 \times 8$ k-points sampling obtained with the Monkhorst-Pack grid. While for the band structure, we considered a path of symmetry considering the group symmetry of the ZIF-8 (I-43M) with 10 points from each point to another. The path chosen was Γ-P-H-PA-Γ.

For calculations with the two-dimensional structures, a $5 \times 5 \times 1$ k-point sampling in the Brillouin zone obtained with the Monkhorst-Pack grid. We considered a unit cell with 20 Å in the axis perpendicular to the sheet. This distance was also tested until the interaction with the image from PBC was irrelevant. It is important to remark that to obtain the PDOS we used more k-points sampling with $20 \times 20 \times 1$ in the Brillouin zone with the Monkhorst-Pack grid.

3 | Atomistic Simulations

In this chapter we address the theoretical foundations of atomistic simulations such as Monte Carlo and Molecular Dynamics, both used in this work. Using these methodologies we can simulate adsorption and transport properties in different systems involving ZIF-8 structures more efficiently.

3.1 Force Fields

Despite accurately describing systems, ab initio methods are computationally costly. Systems involving the adsorption of greenhouse gases in MOFs might have hundreds or even thousands of atoms, which makes it too expensive to simulate by only ab initio methods. Therefore, the use of classical methods is necessary to make these studies viable.

In atomistic simulations, one can model the interaction of atoms through classical force fields (FFs). Here, a particular form of FF has been used as introduced by Wu et al. [26]. Bond and angle energies are modeled through harmonic potentials. In contrast, dihedral (proper and improper) energies are modeled via Fourier or Ryckaert-Bellemans functional forms. Moreover, for nonbonded interactions, typically, Coulomb and Lennard-Jones (LJ) interactions are considered [69, 70, 71]. Thus, the total interaction energy of a system would be given by:

$$\mathcal{U}(\mathbf{r}^N) = u_{\text{bond}} + u_{\text{angle}} + u_{\text{torsional}} + u_{\text{improper}} + u_{\text{non-bonded}}, \tag{3.1}$$

where $\mathbf{r}^N$ are the coordinates of the N atoms in the system, u_{bond} describes the vibration between bonded atoms, u_{angle} the vibration of bonded angles, $u_{\text{torsional}}$ proper dihedrals, u_{improper} improper dihedrals, and $u_{\text{non-bonded}}$ non-bonded interactions.

In this work, the functional form of those potentials was considered as follows [26]:

$$u_{\text{bond}} = K_b(b - b_0)^2 \tag{3.2}$$

$$u_{\text{angle}} = K_\theta(\theta - \theta_0)^2 \tag{3.3}$$

$$u_{\text{dihedral}} = K_{\varphi}[1 + \cos(n\varphi - \varphi_0)] \tag{3.4}$$

$$u_{\text{improper}} = K_{\psi}[1 + \cos(n\psi - \psi_0)] \tag{3.5}$$

$$u_{\text{non-bonded}} = u_{LJ} + u_{\text{Coul}} = 4\varepsilon_{ij}\left[\left(\frac{\sigma_{ij}}{r}\right)^{12} - \left(\frac{\sigma_{ij}}{r}\right)^{6}\right] + \frac{q_i q_j}{4\pi\varepsilon_0 r} \tag{3.6}$$

K_b, K_θ, K_φ, and K_ψ are constants that determine the depth of the well of the potential. b, θ, φ, and ψ are bond lengths, angles, proper and improper dihedrals, respectively. n is the multiplicity and was set to two or three usually. b_0, θ_0, φ_0, and ψ_0 corresponds to equilibrium points. Each parameter is specified for the type of atoms involved. For the nonbonded interactions, σ_{ij} is the collision diameter, and ε_{ij} is the energy well depth for species i interacting with species j. The self-interacting parameters are given, and Lorentz-Berthelot combining rules were used for cross interactions: [72, 73]

$$\sigma_{ij} = \frac{(\sigma_{ii} + \sigma_{jj})}{2} \tag{3.7}$$

$$\varepsilon_{ij} = \sqrt{\varepsilon_{ii} + \varepsilon_{jj}} \tag{3.8}$$

A scaled 1-4 policy was considered for nonbonded interactions between bonded atoms. Interactions between couples of bonded atoms (1-2) or the second neighbors (1-3) are excluded, while interactions between atoms separated by two other atoms (1-4) are scaled by 0.5 [26].

Three different greenhouse gases were modeled, CO_2, CH_4, and N_2. Carbon dioxide molecules were modeled using the rigid EPM2 model [74], methane molecules were modeled with the TraPPE united-atom model [75], and nitrogen gas was modeled using the TraPPE three-site rigid model (two sites for the N atoms and one site at the center of mass labeled "M") to include quadrupole moment and charges [76]. Together with bond length information, all LJ parameters and Coulombic partial charges are given in Appendix A.

Regarding the interactions of ZIF-8 with greenhouse gases, several FFs are reported in the literature [24, 27, 25, 77, 26, 28, 78, 31, 29, 30, 32]. Some of them are focused on describing well adsorption properties [24, 25, 77, 26], while others describe better the flexibility of the structure leading to more accurate transport properties [27, 78, 30]. However, it is quite hard to simultaneously describe both properties with satisfactory accuracy. Since the main objective of this work is to study the adsorption properties of this nanostructure, we considered the FF built by Wu et al., which is capable of accurately describing adsorption isotherms of the three gases explored in this work while keeping a reasonable description of the structure flexibility [26]. Wu et al. validate their FF

by reproducing experimental lattice parameters at different temperatures, adsorption isotherms of CO_2, CH_4, N_2, and H_2, and experimental self-diffusion coefficients for all these gases.

It is based on the AMBER FF [79], the Universal Force Field (UFF) [80], and experimental data. Parameters for the organic linkers were adapted from the AMBER FF, and interactions of tetrahedral ZnN_4 were based on quantum chemical calculations and experimental ad hoc parameters. The LJ parameters are obtained with a scaling of the UFF parameters done empirically by adjusting simulated adsorption isotherms to experimental isotherms. The scaling constants considered by Wu et al. are

$$\varepsilon = 0.635\varepsilon_{\mathrm{UFF}}, \tag{3.9}$$

$$\sigma = 1.0\sigma_{\mathrm{UFF}}. \tag{3.10}$$

Coulombic partial charges were computed using the density-derived electrostatic and chemical charge method (DDEC) [81]. The LJ parameters and Coulombic partial charges are given in Appendix A.

3.1.1 Periodic Boundary Conditions

In this work, periodic boundary conditions (PBC) were considered in all simulations and in all directions. Using a primitive cell that will be replicated in all directions lets us simulate an infinite periodic system, allowing us to calculate bulk properties properly. Figure 3.1 represents a system replicated. Each particle can interact with all image particles. Nevertheless, to consider all these infinite interactions would be impossible computationally. Therefore, we need to consider the minimum-image convention, where the particle will interact with the nearest image or truncate the interactions with a cutoff radius.

3.1.2 Cutoff Radius and Long Range Corrections

LJ and Coulombic interactions extend to infinite. However, it is not viable to consider these interactions from long term distances computationally. In order to deal with this, a cutoff radius is imposed. The nonbonded interactions are not considered, unless the distance between the atoms is less than the cutoff radius, i.e., both atoms can be included in a sphere with a radius lower or equal to the cutoff radius. However, this cutoff radius must be large enough to be negligible without drastic impacts in the simulation [69, 70]. Note also that the cutoff radius must be lower than half the length of the primitive cell due to PBC, avoiding unwanted effects.

Nevertheless, in periodic systems, long-range electrostatic interactions play important roles. In order to consider these interactions, two common methods are usually applied,

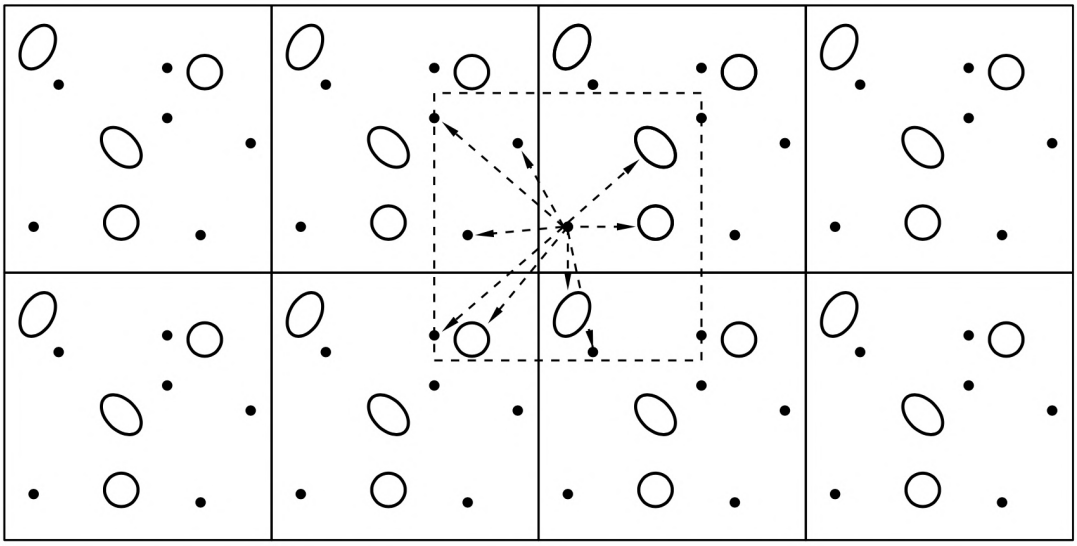

Figure 3.1: Schematic representation of a system replicated with periodic boundary conditions. Image from [69].

Ewald summation [82, 83] or PPPM (particle-particle particle-mesh) method [84]. The idea is to treat short-range interactions differently, which will be calculated in the real space, from long-range interactions that will be calculated in the k-space using Fourier transformations. By doing that, high accuracy and reasonable computational cost are achieved [69, 70]. In this work, the Ewald summation method was employed.

3.2 Monte Carlo

In atomistic simulations, usually, the objective is to obtain the average of an observable $\mathcal{A}$. From statistical mechanics, this average is given by

$$\langle \mathcal{A} \rangle = \frac{\int d\mathbf{p}^N d\mathbf{r}^N \mathcal{A}(\mathbf{p}^N, \mathbf{r}^N) \exp[-\beta \mathcal{H}(\mathbf{p}^N, \mathbf{r}^N)]}{\int d\mathbf{p}^N d\mathbf{r}^N \exp[-\beta \mathcal{H}(\mathbf{p}^N, \mathbf{r}^N)]}, \tag{3.11}$$

where $\mathbf{r}^N$ and $\mathbf{p}^N$ stands for the coordinates and momenta, respectively, of all N particles in the system, $\mathcal{H}(\mathbf{p}^N, \mathbf{r}^N)$ is the Hamiltonian, and $\beta = 1/k_B T$, with k_B as the Boltzmann constant and T the temperature. As usual, the dependence on the momenta is only present in the kinetic energy, which is a quadratic function of the momenta. The integration over momenta can be carried out analytically. The problem arises once one tries to integrate over the particle coordinates. Only in a few particular problems it could be computed analytically. To integrate this expression numerically is also infeasible. Even for small systems in the order of one hundred particles in three dimensions and a small mesh of integration would need the integrand to be evaluated at $\approx 10^{200}$ points, which is an extremely large number, making it impractical [69, 70].

The Monte Carlo (MC) method developed by von Neumann, Ulam, and Metropolis

[85, 86, 87] tries to address this problem with importance sampling. It is based on using random numbers to sample the states of a system using the Boltzmann distribution. Thus, the main idea is to efficiently sample the space phase region by obtaining more points in regions where the Boltzmann factor is relevant and only a few where it will vanish. It is a Markov chain method where new states are generated based on the last state of the system. Each new state might be accepted or not based on an acceptance criterion chosen to reproduce the Boltzmann distribution, which the probability of the system in a given state is given by:

$$\mathcal{N}(\mathbf{r}^N) = \frac{\exp[-\beta\mathcal{U}(\mathbf{r}^N)]}{\int d\mathbf{r}^N \exp[-\beta\mathcal{U}(\mathbf{r}^N)]}, \tag{3.12}$$

where $\mathcal{U}(\mathbf{r}^N)$ is the potential energy of the configuration defined in Equation 3.1 and depends only in the configuration of the N atoms in the system. Note that the integration over momenta and the kinetic energy part of the Hamiltonian were omitted since it has an analytical solution that can be included in the final average value of the observable [88].

Hence, the ensemble average could be written as

$$\langle\mathcal{A}\rangle = \int d\mathbf{r}^N \mathcal{N}(\mathbf{r}^N)\mathcal{A}(\mathbf{r}^N), \tag{3.13}$$

implying that if the configuration space sampling follows $\mathcal{N}(\mathbf{r}^N)$ the average can be calculated approximately as

$$\langle\mathcal{A}\rangle \approx \frac{1}{N_{\text{steps}}} \sum_{i=1}^{N_{\text{steps}}} \mathcal{A}_i, \tag{3.14}$$

where $\mathcal{A}_i$ is the observable value in the state i.

The sampling criteria are based on a Markov chain method. Consider an initial state denoted as o, from old. A trial move in the configuration is applied, generating a new state denoted as n, from new. The transition probability $\pi(o \to n)$ to go from configuration o to n is written as

$$\pi(o \to n) = \alpha(o \to n)\text{acc}(o \to n), \tag{3.15}$$

where $\alpha(o \to n)$ is the probability of generating this trial move and $\text{acc}(o \to n)$ is the probability of accepting this trial move.

We impose that at equilibrium, the average number of accepted moves from o to n is exactly canceled by the number of reverse moves. This implies the detailed balance condition: [69, 70]

$$\mathcal{N}(o)\alpha(o \to n)\text{acc}(o \to n) = \mathcal{N}(n)\alpha(n \to o)\text{acc}(n \to o). \tag{3.16}$$

In the Metropolis method, we choose α to be symmetric ($\alpha(o \to n) = \alpha(n \to o)$),

implying that from Equation 3.16 the acceptance probability can be determined. Metropolis condition that $\text{acc}(o \to n) = 1$ if n has smaller energy than o, leads us to:

$$\text{acc}(o \to n) = \min\left(1, \exp[-\beta\{\mathcal{U}(n) - \mathcal{U}(o)\}]\right). \tag{3.17}$$

It is important to remark that many choices of $\text{acc}(o \to n)$ satisfy Equation 3.16, but the choice of Metropolis et al. seems to result in an efficient sampling of the configuration space [69]. Note also that it is only necessary to calculate the difference in energy between the two states. This is why this method is so efficient. In principle, it has a clear advantage in relation to molecular dynamics, since it is not necessary to calculate the forces in the system. Additionally, it is very useful to simulate systems with very high potential energy barriers since by the generation of new random states it is not necessary to physically surpass the barrier.

In a rigid setting, the trial moves are related to the translation and rotation of the atoms or molecules in the system. The translation moves apply a random translation in each dimension drawn from a uniform distribution between a pre-determined interval. In comparison, the rotation moves are applied by first determining a random axis and then applying a small rotation by this axis, also drawn from a uniform distribution between a pre-determined interval.

Note also that since the Monte Carlo method is based on a Markov chain method, a new state will be highly correlated with the last one. For the averages stated in Equation 3.14, it is important to take uncorrelated configurations to estimate the ensemble average of the observable. Here, we considered the energy as an estimator for the correlation since it is associated with the acceptance criteria. Only configurations that were less than 10% correlated were considered to take ensemble averages.

3.2.1 Ensembles

Since we are following the Boltzmann distribution, a conventional Monte Carlo as described before probes the canonical ensemble (NVT ensemble). It is also important to sample in the isobaric-isothermal (NPT) ensemble and the Grand Canonical (μVT) ensemble to explore adsorption properties using Monte Carlo techniques.

NPT ensemble

Usually, experimentally it is easier to control the pressure and temperature in the system. Therefore, simulating the system in the NPT ensemble is very useful to compare with experimental measurements. In this ensemble, the probability of finding a configuration with constant pressure P at a volume V is proportional to

$$\mathcal{N}(\mathbf{r}^N, V) \propto V^{N+1} \exp\{-\beta[\mathcal{U}(\mathbf{r}^N, V) + PV]\}. \tag{3.18}$$

Note that the volume V now needs to be changed with trial moves the same way as the coordinates. Again, with ΔV chosen from a random uniform interval, the volume will be changed as $V(n) = V(o) + \Delta V$. Note that if $\Delta V > 0$ an artificial vacuum region might be created, and if $\Delta V < 0$ molecules could be expelled . To avoid that, coordinates r^N must be scaled instead of just creating a new region or deleting an existing region (considering a cubic system the coordinates must be multiplied by $(V(n)/V(o))^{1/3}$. With this probability and considering the detailed balance condition, the acceptance probability is given by

$$\begin{aligned} \mathrm{acc}(o \to n) = \min\big(1, \exp\big[&- \beta \{\mathcal{U}(n) - \mathcal{U}(o) \\ &+ P[V(n) - V(o)] - (N+1)\beta^{-1} \ln[V(n)/V(o)]\}\big]\big) . \end{aligned} \tag{3.19}$$

Grand Canonical Ensemble

The Grand Canonical (GC) Ensemble, also known as the μVT ensemble keeps constant the chemical potential μ, the volume V, and the temperature T. It is very useful to simulate adsorption since the number of particles is not constant in the system. Imagine that our system is at equilibrium with a reservoir where the exchange of particles (N) and heat (Q) is allowed, as illustrated by Figure 3.2. Thus, it allows the simulation of the adsorption process without the need to simulate a real huge reservoir. Instead, we consider a fictitious reservoir represented by the chemical potential and the temperature. It is important to remark that the chemical potential can be related to the pressure of the reservoir. We will discuss more on this in Section 4.4. Usually, Monte Carlo simulations in the Grand Canonical ensemble are called Grand Canonical Monte Carlo (GCMC).

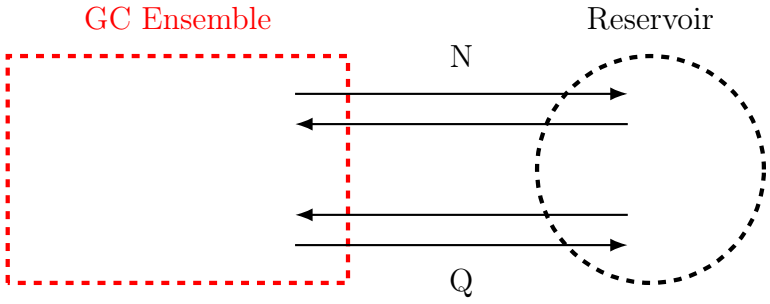

Figure 3.2: Representation of the Grand Canonical Ensemble where the system is in equilibrium with a reservoir allowing exchange of heat and particles.

The probability density is given by

$$\mathcal{N}(\mathbf{r}^N, N) \propto \frac{\exp[\beta\mu N] V^N}{\Lambda^{3N} N!} \exp[-\beta \mathcal{U}(\mathbf{r}^N)], \tag{3.20}$$

where $\Lambda = \sqrt{\beta h^2/(2\pi m)}$ is the thermal de Broglie wavelength, with m being the mass, and h the Planck constant. Therefore, the acceptance criteria can be derived for the

insertion and removal of particles, respectively:

$$\mathrm{acc}(N \to N+1) = \min\left[1, \frac{V}{\Lambda^3(N+1)} \exp\{\beta[\mu - \mathcal{U}(N+1) + \mathcal{U}(N)]\}\right], \tag{3.21}$$

$$\mathrm{acc}(N \to N-1) = \min\left[1, \frac{\Lambda^3 N}{V} \exp\{-\beta[\mu + \mathcal{U}(N-1) - \mathcal{U}(N)]\}\right]. \tag{3.22}$$

The acceptances for the displacement of the particles remain the same as in the NVT ensemble.

3.2.2 Configurational Bias Monte Carlo

Bias Monte Carlo methods are based on the probability of a trial move being not necessarily the same in the reverse operation: $\alpha(o \to n) \neq \alpha(n \to o)$. Consider that the probability will be an arbitrary function of the energy, which means $\alpha(o \to n) = f[\mathcal{U}(n)]$. Following the Metropolis method, using the Boltzmann distribution, we get new criteria of acceptance given by

$$\mathrm{acc}(o \to n) = \min\left(1, \frac{f[\mathcal{U}(o)]}{f[\mathcal{U}(n)]} \exp\{-\beta[\mathcal{U}(n) - \mathcal{U}(o)]\}\right). \tag{3.23}$$

With that bias, Monte Carlo methods allow favoring sampling of more relevant states by defining the function f. This bias can be removed from the acceptance criteria.

3.2.3 Computational implementation

In our calculations, the Cassandra open-source Monte Carlo package was used [89]. Cassandra can simulate several ensembles such as NVT, NPT, μVT, μPT, and Gibbs ensembles. It uses Configurational Bias Monte Carlo (CBMC) based on sampling a library of fragment conformations [90]. For a biased insertion of molecules, the molecule is first divided into fragments, and it is possible to insert atom by atom, for example. Doing that, we avoid inserting problematic configurations, such as ones where atoms are superposed. It also can improve the acceptance ratio by generating several insertion positions for the first fragment and selecting only one of these positions for the total insertion [91].

Usually, flexible structures are more challenging to model using Monte Carlo. Zhang et al. showed using hybrid simulations (Monte Carlo intercalated with Molecular Dynamics simulations) that the flexibility of ZIF-8 does not impact the adsorption. Rigid and flexible structures yield the same adsorption rates [77]. Thus, in this work, all Monte Carlo simulations consider a rigid framework, i.e., only the nonbonded terms are considered in the potential energy described in Equation 3.1.

In our atomistic simulations we used a cutoff radius of 17.0 Å for LJ and Coulombic interactions together with the Ewald sum for long-range interactions with a considered accuracy set to 10^{-5}. For simulations in the NPT ensemble, a probability of 0.485 was used for translation and rotation trial moves, while a probability of 0.03 was used for volume trial moves. The translation had a maximum displacement of 1 Å, the rotation had a maximum of 180°, and the volume a maximum of 2000 $Å^3$ for each step.

As for simulations in the GC ensemble, each trial move (translation, rotation, insertion, removal) had a probability of 0.25. The translation had a maximum displacement of 1 Å and rotation a maximum of 30°. Insertions were done using CBMC as implemented in Cassandra.

3.3 Molecular Dynamics

The use of other classical methods is necessarily to investigate dynamic properties. Monte Carlo is not efficient to capture the dynamics of the system, urging the need to use other methods. In that way, Molecular Dynamics shows as an alternative to investigate other properties of the systems.

To address the problem of averaging out an observable ($\langle \mathcal{A} \rangle$), Molecular Dynamics (MD) are based on the ergodic hypothesis as stated in Equation 3.24, which suggests that the ensemble average is equal to the time average for really large times [69, 70].

$$\langle \mathcal{A} \rangle = \lim_{t \to \infty} \frac{1}{t} \int_{t_0}^{t_0+t} \mathcal{A}(\tau) d\tau. \tag{3.24}$$

Considering a system of N interacting particles, the idea is to solve Newton's equations of motion numerically to obtain the temporal evolution of the system:

$$m_i \frac{\partial^2 \mathbf{r_i}}{\partial t^2} = \mathbf{F_i} = -\frac{\partial \mathcal{U}}{\partial \mathbf{r_i}}, \tag{3.25}$$

where $\mathbf{r_i}$ and m_i are the position and mass of particle i, respectively, and F_i are the forces obtained from the energies given from the FF used ($\mathcal{U}$).

To solve this equation numerically, we must discretize the time interval in time steps (Δt). Among distinct integration schemas, the Verlet algorithm is simple and, usually, the most common algorithm used to integrate equations of motion. The idea is to expand the coordinates of a particle around time t (for simplicity, the index i will be omitted) [69, 70]

$$\mathbf{r}(t + \Delta t) = \mathbf{r}(t) + \mathbf{v}(t)\Delta t + \frac{\mathbf{F}(t)}{2m}\Delta t^2 + \frac{\Delta t^3}{3!}\frac{\partial^3 \mathbf{r}}{\partial t^3} + \mathcal{O}(\Delta t^4), \tag{3.26}$$

similarly,

$$\mathbf{r}(t - \Delta t) = \mathbf{r}(t) - \mathbf{v}(t)\Delta t + \frac{\mathbf{F}(t)}{2m}\Delta t^2 - \frac{\Delta t^3}{3!}\frac{\partial^3 \mathbf{r}}{\partial t^3} + \mathcal{O}(\Delta t^4). \tag{3.27}$$

Summing both equations:

$$\mathbf{r}(t+\Delta t)+\mathbf{r}(t-\Delta t)=2\mathbf{r}(t)+\frac{\mathbf{F}(t)}{m}\Delta t^2+\mathcal{O}(\Delta t^4), \tag{3.28}$$

From where we can approximately get $\mathbf{r}(t+\Delta t)$ with an error of order Δt^4 as

$$\mathbf{r}(t+\Delta t)\approx 2\mathbf{r}(t)-\mathbf{r}(t-\Delta t)+\frac{\mathbf{F}(t)}{m}\Delta t^2. \tag{3.29}$$

Note that in the Verlet algorithm, the velocity is not used to compute new positions, but it can be derived from the trajectory using the following:

$$\mathbf{r}(t+\Delta t)-\mathbf{r}(t-\Delta t)=2\mathbf{v}(t)\Delta t+\mathcal{O}(\Delta t^3), \tag{3.30}$$

which implies the velocity is obtained with an error of order Δt^3 from

$$\mathbf{v}(t)=\frac{\mathbf{r}(t+\Delta t)-\mathbf{r}(t-\Delta t)}{2\Delta t}. \tag{3.31}$$

Note that the Verlet algorithm introduces a problem in the first time step since the coordinates from the two previous time steps are necessary. An equivalent and more commonly used method is the velocity Verlet algorithm [92] that solves the equations of motion in the same order as the basic Verlet but addresses this problem of the first step. The coordinates are obtained from the Taylor expansion:

$$\mathbf{r}(t+\Delta t)=\mathbf{r}(t)+\mathbf{v}(t)\Delta t+\frac{\mathbf{F}(t)}{2m}\Delta t^2, \tag{3.32}$$

and the velocity is obtained from

$$\mathbf{v}(t+\Delta t)=\mathbf{v}(\mathbf{t})+\frac{\mathbf{F}(t+\Delta t)+\mathbf{F}(t)}{2m}\Delta t. \tag{3.33}$$

First we calculate $\mathbf{r}(t+\Delta t)$, using this new coordinates we can calculate $F(t+\Delta t)$ that will be used to compute $\mathbf{v}(t+\Delta t)$.

To show that the velocity Verlet is equivalent to the basic Verlet algorithm, consider

$$\mathbf{r}(t+2\Delta t)=\mathbf{r}(t+\Delta t)+\mathbf{v}(t+\Delta t)\Delta t+\frac{\mathbf{F}(t+\Delta t)}{2m}, \tag{3.34}$$

and note that Equation 3.32 can be written as

$$\mathbf{r}(t)=\mathbf{r}(t+\Delta t)-\mathbf{v}(t)\Delta t-\frac{\mathbf{F}(t)}{2m}\Delta t^2. \tag{3.35}$$

Adding both equations, we get

$$\mathbf{r}(t+2\Delta t)+\mathbf{r}(t)=2\mathbf{r}(t+\Delta t)+[\mathbf{v}(t+\Delta t)-\mathbf{v}(t)]\Delta t+\frac{\mathbf{F}(t+\Delta t)-\mathbf{F}(t)}{2m}\Delta t^2, \tag{3.36}$$

using Equation 3.33 we obtain

$$\mathbf{r}(t + 2\Delta t) + \mathbf{r}(t) = 2\mathbf{r}(t + \Delta t) + \frac{\mathbf{F}(t + \Delta t)}{m}\Delta t^2, \tag{3.37}$$

which is the coordinate version of the basic Verlet algorithm.

3.3.1 Ensembles

Following Newton's equation of motion, Molecular Dynamics immediately describes the NVE ensemble, where the number of particles, volume, and energy are kept constant. However, to simulate conditions obtained experimentally, as discussed in Section 3.2.1, it is useful to simulate the system in the NVT and NPT ensembles. Temperature and pressure might be introduced in Molecular Dynamics using thermostats and barostats, respectively. This can be done through reservoirs in equilibrium with the system.

In this work, we used thermostats, and barostats of Nosé-Hoover [93]. By adding dynamic variables coupled to the particle velocities and simulation domain dimensions to the lagrangian of the system, we control the temperature and pressure in the system. This formulation guarantees sampling in the NVT or NPT ensemble where the target temperature and pressure are achieved oscillatory.

Hence, atomistic simulations help us understand adsorption and transport properties in larger systems more efficiently. Loading a supercell of ZIF-8 with hundreds of guest molecules can make ab initio calculus very time consuming. Consequently, the use of these methodologies seems essential to understand better bigger systems. More details on the use of these methodologies and what calculations have been done in this work are discussed in the next chapter.

3.3.2 Computational Implementation

In this work, we used the Large-scale Atomic/Molecular Massively Parallel Simulator (LAMMPS) [94] to simulate the transport properties of greenhouse gases in ZIF-8. LAMMPS is an open-source code largely used by the scientific community to perform Molecular Dynamics simulations. The integration of the equations of motion was done following the default implemented in LAMMPS, using the velocity Verlet algorithm.

A time step of 1.0 fs was enough to describe the systems explored here accurately, and it was used in all simulations performed. ZIF-8 was modeled with the $2 \times 2 \times 2$ supercell and using the FF as described in Section 3.1.

4 | Pristine ZIF-8

MOFs are a very promissing type of material regarding carbon capture. To understand more on their bulk properties and the interaction with different gases the use of molecular modelling is very propitious. This chapter presents the results obtained for pristine ZIF-8, going from DFT calculations to GCMC and MD simulations. Using DFT, we investigated bulk and electronic properties, followed by an investigation of carbon dioxide adsorption.

Moreover, results obtained through atomistic simulations are also presented. Adsorption isotherms obtained with Monte Carlo and the respective preferable adsorption sites are presented considering several gas atmospheres (single component and mixtures). Dynamic properties are investigated using MD, the pore size relation with temperature and self-diffusion coefficients is explored.

4.1 Bulk Properties

For the calculations of pristine ZIF-8, we considered a unit cell of the ZIF-8, where the initial positions of the atoms were obtained from crystallographic information [95]. The unit cell is represented in Figure 4.1, we see the unit cell in two different views: in the first one the small pore is centered, while in the second the large pore is centered.

The first step was performing a structural relaxation calculation, allowing both the atomic positions' degrees of freedom, and the cell volume and shape to be optimized. We observed that the structure kept its cubic symmetry in all tests. Afterward, we followed a different approach to structural optimization, performing the relaxation only at atomic positions in different volumes, that is, to scale the lattice parameters with 0.05% variation for each calculation and then fit the final energies to an equation of state (EOS). From the EOS, we then obtained the bulk modulus and the volume that minimized the energy for our structure. We considered two different equations of states, the Birch-Murnaghan (BM) [96, 97] and the Rose-Vinet (RV) [98]. Considering $\eta = \left(\frac{V}{V_0}\right)^{1/3}$, where V is the volume and V_0 the volume of equilibrium, the two equations are given respectively by:

$$E = E_0 + \frac{9}{16} B_0 V_0 (\eta^2 - 1)^2 [6 + B_0'(\eta^2 - 1)^2 - 4\eta^2] \tag{4.1}$$

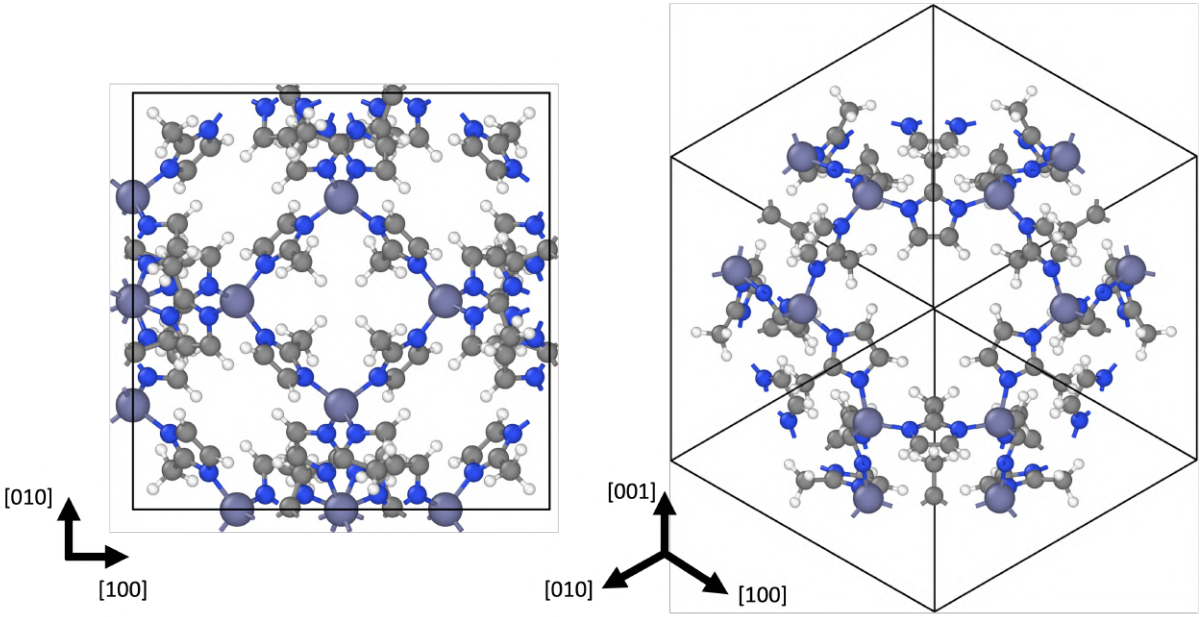

Figure 4.1: Two different views of the ZIF-8 unitary cell constructed based on atomic positions given by crystallographic information [95]. In purple we have zinc atoms, in blue nitrogen atoms, in gray carbon atoms, and in white the hydrogen atoms.

$$E = E_0 + 2\frac{B_0 V_0}{(B_0' - 1)^2}(2 - [5 + 3B_0'(\eta - 1) - 3\eta]e^{-\frac{3}{2}(B_0' - 1)(\eta - 1)}) \tag{4.2}$$

where E is the total energy, E_0 is the minimum energy, B_0 is the bulk modulus, and B_0' is the derivative of the bulk modulus with respect to pressure.

The BM EOS is often used in condensed matter. However, the RV EOS presents a more general description considering an exponential decay rather than a polynomial. Taking this into account, RV EOS better describes the compressibility of extended solid systems. Since MOFs are usually very flexible, RV description tends to be necessary to get an accurate fit [99].

After obtaining the minimum volume V_0, we performed another relaxation calculation with the minimum volume cell, allowing only the atomic positions to change, thus allowing us to obtain the correct relaxed structure from where any desirable observable can be calculated.

Using DFT with experimental crystallographic data [95] to obtain initial atomic positions, we calculated the total energy as a function of the volume of the unit cell as shown in Figure 4.2. Experimental volume is obtained from crystallographic information [95]. The blue curve represents the fit data using the BM EOS, while the green one is the fitting using the RV EOS. Table 4.1 indicates the lattice parameter (a_0) related to the volume that minimizes the energy (V_0), i.e., $a_0 = V_0^{1/3}$ and also the bulk modulus (B_0) obtained through the fit. Moreover, it also shows the R^2 statistical parameter obtained for each fitting.

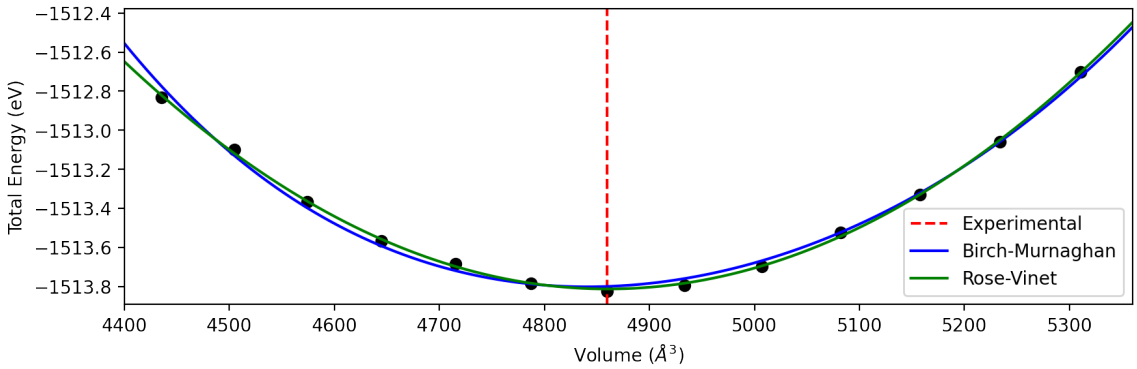

Figure 4.2: Total energy of ZIF-8 in function of the volume of the unit cell each point is obtained allowing the system to relax atomic positions to reach the minimum of energy constrained to that volume. In blue, we see the fitting using the BM EOS, and in green, the RV EOS. Experimental volume is from crystallographic data [95].

Table 4.1: Lattice parameter a_0 related to the volume that minimizes the total energy and the bulk modulus obtained with each EOS used to fit the data. R^2 is also presented to indicate the quality of the fitting.

	a_0 (Å)	B_0 (GPa)	R^2
BM	16.916 ± 0.004	7.76 ± 0.72	0.994
RV	16.939 ± 0.004	8.53 ± 0.09	0.999
Exp.	16.939 [1]	6.52 [2], 7.75 [3]	-

Despite both EOS fitting data very accurately with a good R^2 score, RV is slightly better (which is expected since it has a more complete description of compressibility). We get a lattice parameter in agreement with experimental crystallographic data using the RV fitting. For the bulk modulus, we have some differences regarding experimental data, with the BM fitting presenting a better agreement. These discrepancies could be linked to the fact that the ground state DFT essentially performs calculations at $T = 0$K and thus does not consider the thermal effects present in the experimental data obtained at room temperature.

Thus, this reduction in the bulk modulus might be associated with temperature effects, and these two data are not exactly comparable. Therefore, we opted to use the RV fit to relax our structure due to a better R^2 score and a better agreement for the lattice parameter. In comparison, sodalite zeolites have a Bulk Modulus around 50 GPa [100, 101]. Which means pristine ZIF-8 have a lower Bulk Modulus, corresponding to a higher compressibility compared to these systems.

4.2 Electronic Properties

Using the lattice parameter that minimizes the total energy from the RV fit, we relaxed atomic positions once again and calculated a cycle of self-consistent KS equations. With the relaxed structure and its ground state, we investigated the total electronic density of states together with its partial projection (PDOS). It was necessary an $8 \times 8 \times 8$ k-points sampling obtained with the Monkhorst-Pack grid.

Figure 4.3a presents the results obtained for the PDOS and the band structure of pristine ZIF-8. For the band structure, we considered a path of symmetry considering the group symmetry of the ZIF-8 (I-43M) with 10 points from each point to another. The path chosen was Γ-P-H-PA-Γ. In Figure 4.3b, we see the band structure zoomed into the last valence bands and first conduction bands, from where we can see that the band gap is direct (maximum of the valence band is at the same k-point of the minimum of conduction band).

Specifically, from the PDOS, we can see that the most relevant orbitals in the last valence bands and first conduction bands are associated with C, and N. Orbitals from Zn are not present in these bands. The PDOS and band structure shows that ZIF-8 is a wide band-gap semiconductor, with a calculated band-gap of 3.964 eV. Usually, in the literature we find reports that indicates the optical band-gap of ZIF-8 vary between 3.87 and 5.45 eV [102].

4.3 Carbon Dioxide Adsorption

Adsorption energy is a key property to understand how the framework interacts with a guest molecule, e.g., with information on the strength of the adsorption energy one can determine if the adsorption happens through physical or chemical process.

To calculate the adsorption energy of CO_2 at different adsorption sites, initially, we insert a CO_2 molecule near the desirable site and relax the atomic positions minimizing the total force in the atoms. After the minimization, using the total energy of the system (pristine or thermally treated ZIF-8 + CO_2), we can calculate the adsorption energy (E_{ads}) subtracting the total energy from the energies of the isolated systems, as indicated in the following equation:

$$E_{\text{ads}} = E_{\text{sys+CO}_2} - E_{\text{sys}} - E_{\text{CO}_2}, \tag{4.3}$$

where “sys" labels the system explored, pristine, or thermally treated ZIF-8. For each framework we discuss in details the sites explored.

Additionally, for the preferable sites for each framework, we report the difference of charge observed (Δn), trying to infer which interactions take place in the adsorption

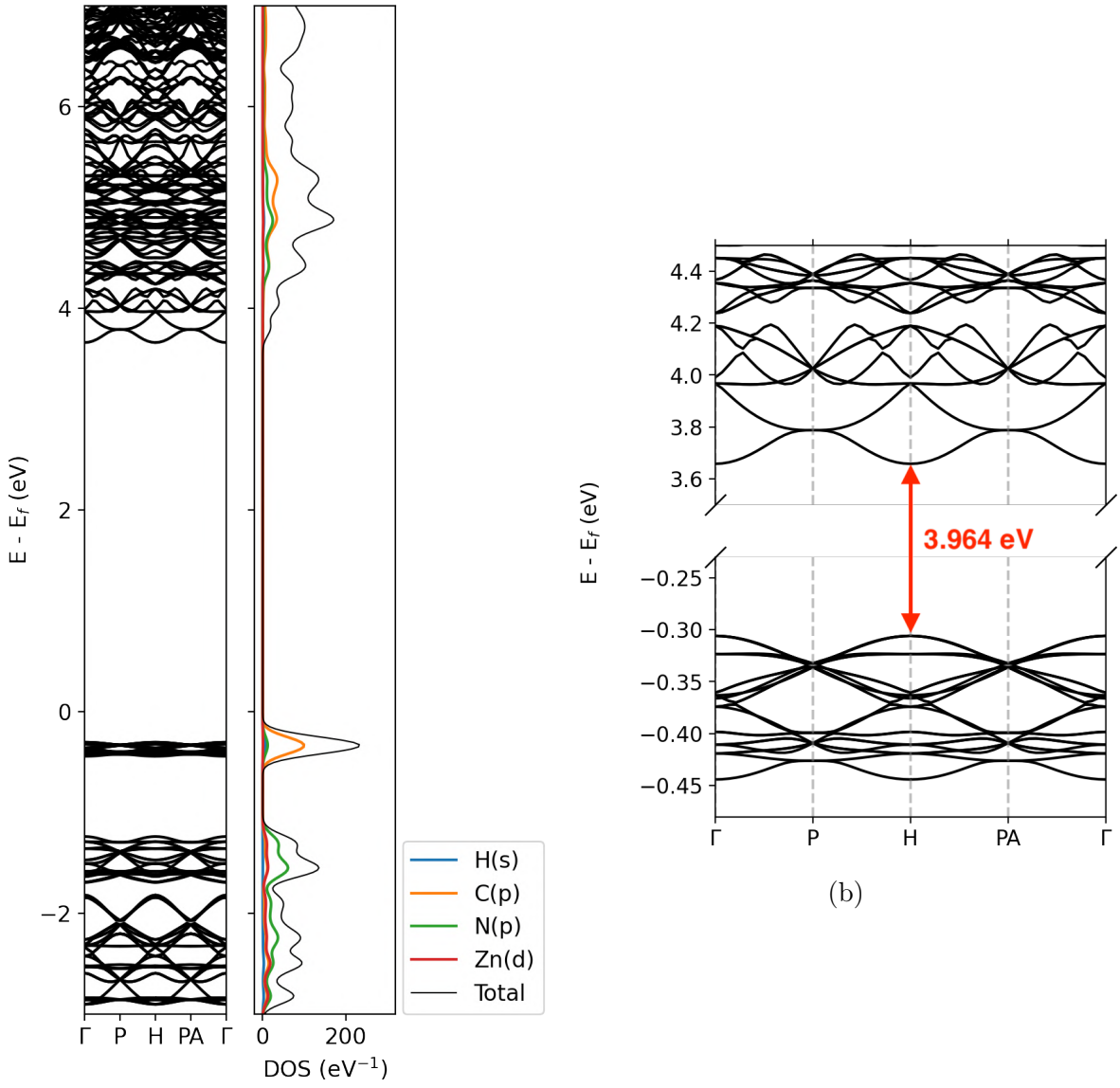

(a)

(b)

Figure 4.3: (a) Band structure alongside the PDOS with the most relevant orbitals for each atomic species in ZIF-8. (b) Band structure is more detailed at the last valence and first conduction bands, indicating that it have a direct band gap.

process. To obtain the charge difference, the electronic density of the system with the guest molecule adsorbed might be subtracted from the electronic densities of the isolated systems, similar to what is done to calculate the adsorption energy, according to the following equation:

$$\Delta n = n_{\text{sys+CO}_2} - n_{\text{sys}} - n_{\text{CO}_2}, \tag{4.4}$$

Regarding carbon adsorption in pristine ZIF-8, we studied five promising sites considering symmetry and previous ab initio works [103, 104, 23]. The metal sites are not favorable for CO_2 adsorption. When trying to position CO_2 molecules near Zn, the forces over the molecule are high, the minimization fast drifts away the guest molecule to another preferable site. Hence, all the Zn related sites were excluded. The first obvious symmetric point is at the center of the cage; this site will be referred to as "cage center" and an illustration is represented in Figure 4.4a.

We also considered orientations within the pores. At the large pore, the stable orientation is when the CO_2 molecule is perpendicular to the pore. This site will be referred to as "large pore" and is represented by Figure 4.4b. At the small pore, we found two different stable positions: the first one is with the CO_2 molecule parallel to the pore and the second one with the CO_2 perpendicular to the pore. These two sites will be referred to as "small pore parallel" and "small pore perp.", and are represented in Figures 4.4c and 4.4d, respectively.

Previous ab initio and our classical simulations indicate that the preferable sites are near the imidazole ring [103, 104, 23]. Different orientations of the CO_2 molecule were taken into account. However, all relaxations led to a preferential orientation of the CO_2 molecule aligned with the organic linker. We will refer to this site as "imidazole ring", and the illustration of the CO_2 molecule at the stable site can be seen in Figure 4.4e.

The adsorption energies are presented in Table 4.2 together with information on the C-O bond length and O-C-O angle at each adsorption site detailed previously. Results from Molecular Mechanics (MM) calculations are also presented; these are calculations made with the classical force field used and discussed in Section 3.1.

At the cage center, the adsorption energy is very small, indicating that the gas and ZIF-8 almost do not interact at this site. At the small pore, the adsorption energy increases, becoming relevant. However, the highest energies are observed in the large pore and near the imidazole ring, which agrees with previous results in the literature [103, 104, 23].

These results are also in agreement with calculations obtained using classical force fields. It is important to note that the increasing trend in energy is maintained, and the imidazole ring is shown to be the preferred site. Even though there is a considerable difference between the absolute energy values in the two methods for each site, this is expected since the use of nonlocal functionals tends to overestimate the adsorption energies.

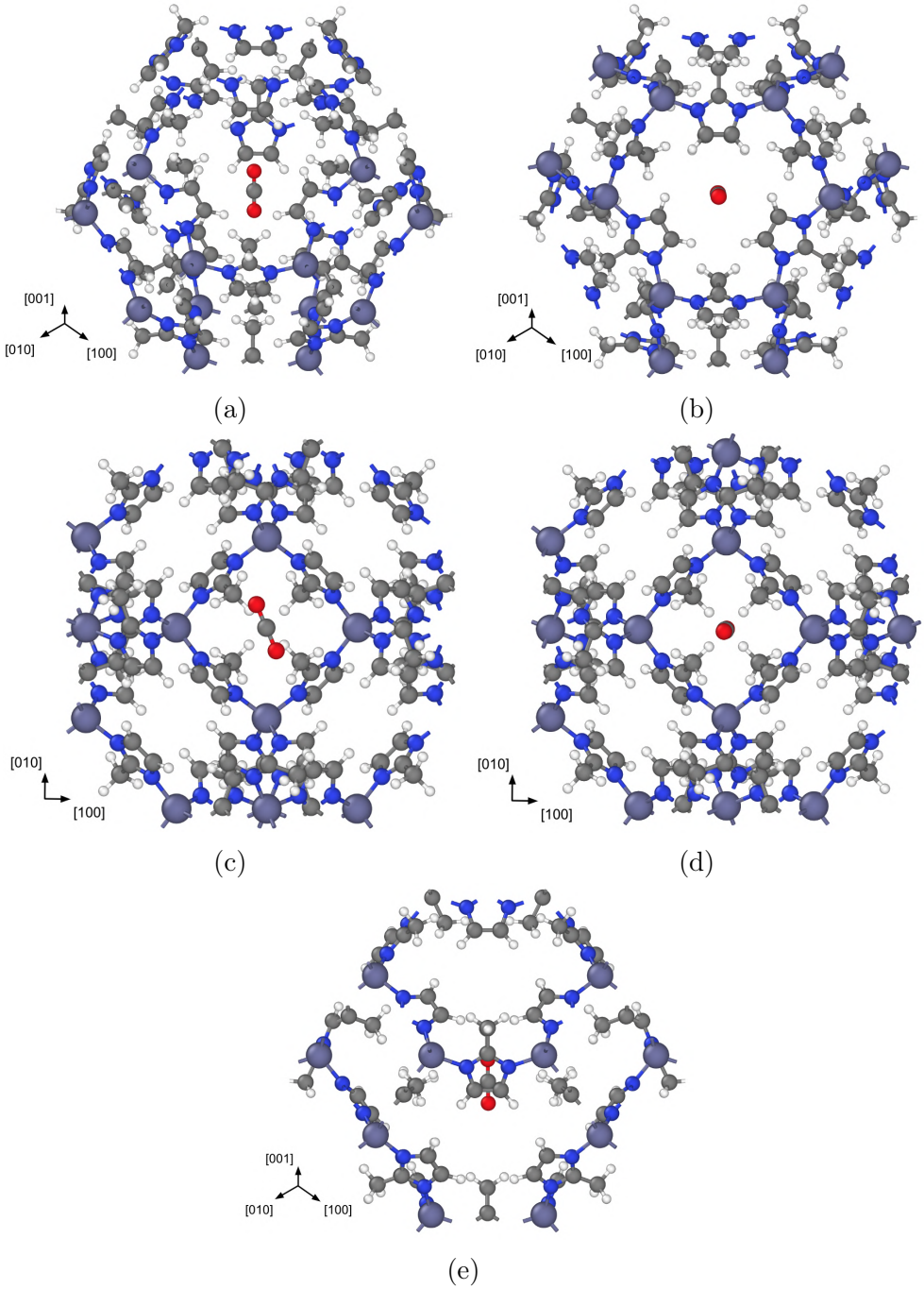

Figure 4.4: Representations of the adsorption sites studied in this work. (a) illustrates the CO_2 molecule at the center of the cage. (b) represents the CO_2 molecule perpendicular to the large pore. (c) and (d) shows the CO_2 parallel and perpendicular to the small pore, respectively. (e) shows the CO_2 near the imidazole ring. Color code is as follows: light purple: Zn; blue: N; gray: C; white: H; red: O.

Table 4.2: Adsorption energy from DFT and Molecular Mechanics (MM) calculations, the C-O bond length, and the O-C-O angle at each adsorption site explored.

		E_{ads} (eV)	C-O bond length (Å)	O-C-O angle (°)
Cage center	DFT	-0.050	1.176	180.0
	MM	-0.038	1.149	180.0
Small pore perp.	DFT	-0.162	1.176	180.0
	MM	-0.110	1.149	180.0
Small pore parallel	DFT	-0.215	1.176	179.8
	MM	-0.177	1.149	180.0
Large pore	DFT	-0.338	1.178 (1.175)	179.9
	MM	-0.222	1.149	180.0
Imidazole ring	DFT	-0.352	1.177	179.9
	MM	-0.252	1.149	180.0

Therefore, these calculations also corroborate to validate this FF, implying that it captures adsorption at a quantum level. Looking for the C-O bond length and the O-C-O angle, it is possible to notice that CO_2 molecules are not distorted in the adsorption, indicating a physisorption process.

Figure 4.5 illustrates the charge density difference. We plot isosurfaces where the density difference equals ± 0.005 e/Bohr^3. Orange isosurfaces are for the positive differences, while pink represents negative charge differences. The color code used for plots considering three-dimensional isosurfaces will follow a different color code. Gray spheres represent Zn atoms, while blue stands for N, cyan for C, and white for H. Note that CO_2 interacts mostly with the two adjacent carbons of the organic linker. The carbon from the CO_2 molecule have a negative density nearby, while the two adjacent carbons of the organic linker have a positive density. It is important to remark that the difference of charge is local, with no significant charge redistribution of long range.

4.4 Single Component Adsorption Isotherms

Initially, to explore adsorption with atomistic simulations, we used GCMC to calculate adsorption isotherms at room temperature (T = 303 K). Experimental adsorption isotherms give the number of molecules adsorbed as a function of pressure, not from the chemical potential. In that way, we need to correlate these two thermodynamic properties [69].

The Widom insertion method allows us to do that. Given a reservoir in a determined temperature and pressure by inserting new molecules in the system and measuring the interaction energy of this new molecule with the system, is possible to infer the chemical

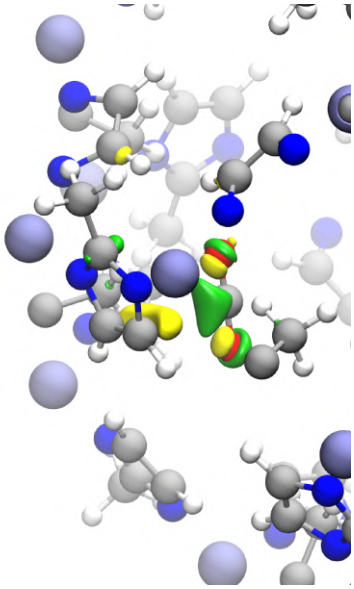

Figure 4.5: Charge density difference for the adsorption of carbon dioxide in pristine ZIF-8 preferable adsorption site, i.e., near imidazole ring. In yellow we have the positive isosurface (0.005 $e/\text{Å}^3$) while in green we have the negative ones (-0.005 $e/\text{Å}^3$). Color code: gray: Zn, blue: N, cyan: C, and white: H.

potential of a desired species in a reservoir [105]. If we define the excess chemical potential $\mu^{\text{ex}} = \mu - \mu^{\text{id}}$, where μ^{id} is the chemical potential for the ideal gas, we can write [70]:

$$\mu^{ex} = \frac{-1}{\beta} \ln \langle \exp(-\beta \mathcal{V}_{\text{test}}) \rangle \,, \tag{4.5}$$

where $\mathcal{V}_{\text{test}}$ is the potential energy from the addition of this new particle, and the average is taken from all the insertions. Note that these trial insertions are never accepted. They are only used to calculate the interaction energy.

It is important to remark that Cassandra only calculates a shifted chemical potential (from where it is possible to obtain the excess chemical potential and consequently the chemical potential) and considers this shifted chemical potential as an input. Therefore, all chemical potentials reported here will refer to this shifted chemical potential.

Several reservoirs were explored in this work, from single components species reservoirs of CO_2, CH_4, and N_2 to binary mixtures of CO_2 with CH_4 and CO_2 with N_2. All the single component species reservoirs studied were at $T = 303$ K, and the pressure range explored goes from 0.1 bar to 50 bar. As for the binary mixtures, we considered equimolar concentrations and explored the same pressure range, fixing a total pressure of 20 bar. Different concentrations were explored, going from 5% of CO_2 and 95% of the other species, increasing 15% of CO_2 and decreasing 15% of the other species until we reach the opposite concentration: 95% of CO_2 with 5% of the other species. All concentrations within this work are expressed as a relation of the number of molecules in the system, and not molecular weight.

For each scenario, first, we simulate the reservoir in the NPT ensemble to equilibrate the system. An initial configuration of 200 molecules was considered in a cubic box with a side length of 100 Å for unique species reservoirs. For mixtures, an initial configuration also with a total of 200 molecules was considered but with each species in the desired concentration. A cubic box with a side length of 100 Å was also considered. In each simulation, 1×10^6 steps were considered for equilibration, and 2×10^6 steps were considered for the Widom insertion method.

Table 4.3 details the results obtained using the Widom insertion method, reporting the resulting shifted chemical potential (μ) and the density at bulk phase (ρ) for each reservoir. The bulk phase density obtained for each reservoir is in agreement with the expected density for these gases.

Table 4.3: Shifted chemical potential (μ) and density at bulk phase (ρ) calculated for each pressure (P) with Monte Carlo at the NPT ensemble using the Widom insertion method for reservoirs of unique species of CO_2, CH_4, and N_2.

P (bar)	CO_2		CH_4		N_2	
	μ (kJ/mol)	ρ (kg/m^3)	μ (kJ/mol)	ρ (kg/m^3)	μ (kJ/mol)	ρ (kg/m^3)
0.1	-46.9	0.2	-43.0	0.1	-45.2	0.1
0.5	-42.8	0.9	-39.0	0.3	-41.1	0.6
1.0	-41.1	1.8	-37.3	0.6	-39.4	1.1
5.0	-37.1	8.9	-33.3	3.2	-35.3	5.6
10.0	-35.4	18.2	-31.5	6.5	-33.6	11.2
20.0	-33.8	38.3	-29.8	13.1	-31.8	22.3
50.0	-31.8	117.9	-27.6	34.4	-29.5	55.7

Through GCMC, it is possible to average how many molecules are adsorbed in a system in equilibrium with a particular reservoir under a determined chemical potential and temperature. As stated before, it is possible to relate this chemical potential with the pressure of the reservoir using the Widom insertion method. With that, from GCMC simulations, we can calculate the number of molecules adsorbed as a function of the pressure keeping the temperature of the reservoir constant. These curves are known as adsorption isotherms and can be compared with experimental measures. We explore adsorption in the ZIF-8 and in the thermally modified frameworks.

The adsorption isotherms of ZIF-8 in all the reservoirs were obtained at $T = 303$ K and in a range of pressure from 0.1 bar to 50 bar. First, it was done an equilibration of 1×10^6 steps of MC followed by 5×10^6 steps as a production phase where the total number of molecules adsorbed were averaged out [1].

Counting the average number of molecules adsorbed in the simulation is equivalent to calculating the absolute number of molecules in the system (N_{abs}). Nevertheless, usually,

[1] Reservoirs at high pressures usually had a higher decorrelation time, needing more steps of production to ensure a good estimate of the number of molecules adsorbed.

adsorption experiments measure the excess adsorption (N_{ex}). Thus, to compare simulations with experimental results, it is necessary to convert from one to another. This can be done as follows:

$$N_{ex} = N_{abs} - \rho_{bulk} V_{free}, \tag{4.6}$$

where ρ_{bulk} is the density of the species at the bulk phase in similar conditions of the reservoir (obtained from the simulations done in the NPT ensemble) and V_{free} is the free volume of the porous structure. In other words, we subtract from the total number of molecules a uniform distribution inside the pore-free volume following the gas density of the reservoir.

To estimate the free volume in ZIF-8, we used a similar method to integration by MC as Herrera et al. proposed [106]. A probe atom is inserted several times inside a unit cell of our framework, and the LJ interaction energy of this atom with the framework is calculated. If this energy is negative, we consider the probe atom inside the free volume. Otherwise, it is out. With the ratio of atoms inside and outside and using the total volume of the unit cell, one can estimate the free volume of the framework. The probe atom must be an inert atom for better results. In this work, we used Helium and Neon. In particular, these simulations to estimate the free volume were done using the Large-scale Atomic/Molecular Massively Parallel Simulator (LAMMPS) [94], and 1×10^6 steps were used to average the free volume.

Since doped graphene and porphyrin-like are two-dimensional structures and not porous, a different approach was considered to calculate the number of molecules adsorbed in the system. Only the adsorption of CO_2 was explored at a constant pressure of 1 bar. Again simulations using GCMC were performed, in which the equilibration phase consisted in 1×10^6 steps and 5×10^6 steps for the production phase. To calculate the excess adsorption, we built the density profile of the number of molecules CO_2 in a function of the direction perpendicular to the plane, from which we can identify adsorption layers. Integrating the density over those layers we obtain the total number of molecules adsorbed in our material.

Generally, experimental results on adsorption are expressed on adsorbed mols over the mass of material considered. From our simulations, we have the total number of molecules adsorbed in the supercell considered. In the pristine ZIF-8 case, we can use the experimental density of ZIF-8 together with the volume of the supercell to do this conversion. For the two-dimensional frameworks, we considered the weight of each atom. From this, we can easily convert adsorption to mols/mass of material used.

Table 4.4 shows the results obtained for the free volume using different probe atoms and the relation of this free volume with the unit cell volume. Even though it is possible to note a significant difference between the volume calculated with He or Ne, this difference was negligible in computing adsorption. Therefore, we opted to use the free volume obtained

using He as a probe atom. It is also important to remark that these calculations are in agreement with experimental measures of the pore volume in ZIF-8 [107].

Table 4.4: Free volume using He and Ne as probe atoms.

Probe atom	Free Volume ($Å^3$)	% of Unit Cell
He	1498.7	30.5 %
Ne	1405.7	28.6 %

Figure 4.6 resumes the insertions of the probe atoms in the ZIF-8 unit cell. Figures 4.6a and 4.6b represent atoms from ZIF-8 in red, probe atoms that were considered out of the free volume in blue and probe atoms considered inside in white. Figure 4.6c represents the ZIF-8 unit cell, and in green, the probe atoms considered in the free volume. As expected, the free volume in the pore is at the center of the unit cell. Note also that probe atoms were considered in the free volume in the corners of the unit cell; due to PBC, these corners will consist another pore. ZIF-8 unit cell comprehends two pores.

Using the chemical potential for each reservoir, the density at the bulk phase, and the free volume, we used GCMC to simulate adsorption isotherms using excess adsorption. Figure 4.7 shows the adsorptions isotherms obtained compared with experimental data provided by Pérez-Pellitero et al. [24]. CO_2 adsorption is described accurately, simulation and experimental data are in agreement. Note also that it is reaching a plateau of adsorption near 50 bar. For CH_4 and N_2, there are minor deviations between simulated and experimental, but adsorption mechanisms in the system are generally captured. It is important to remember that CH_4 is being modeled with a unique atom representation, a very simple model that could explain these deviations. It is important to remark that CO_2 is much more adsorbed in relation to N_2, implying that ZIF-8 might be a proper material to be designed for carbon capture from flue gas.

4.4.1 Preferable Adsorption Sites

To explore the preferable adsorption sites using the GCMC snapshots of the production phase, we discretize the space in small cubes with a side length of 0.34 Å and count atoms of the gas inside each cube, following the procedure done by Wu et al. [26]. Dividing these counts by the total number of gas atoms, we obtain a normalized discrete density from where we can identify more probable sites for adsorption. Note that all data were replicated to a unit cell of the framework facilitating the visualization.

Carbon Dioxide

To study the adsorption sites using GCMC, we can construct a density profile of the molecules adsorbed. Figure 4.8 shows the density of carbon and oxygen atoms from CO_2

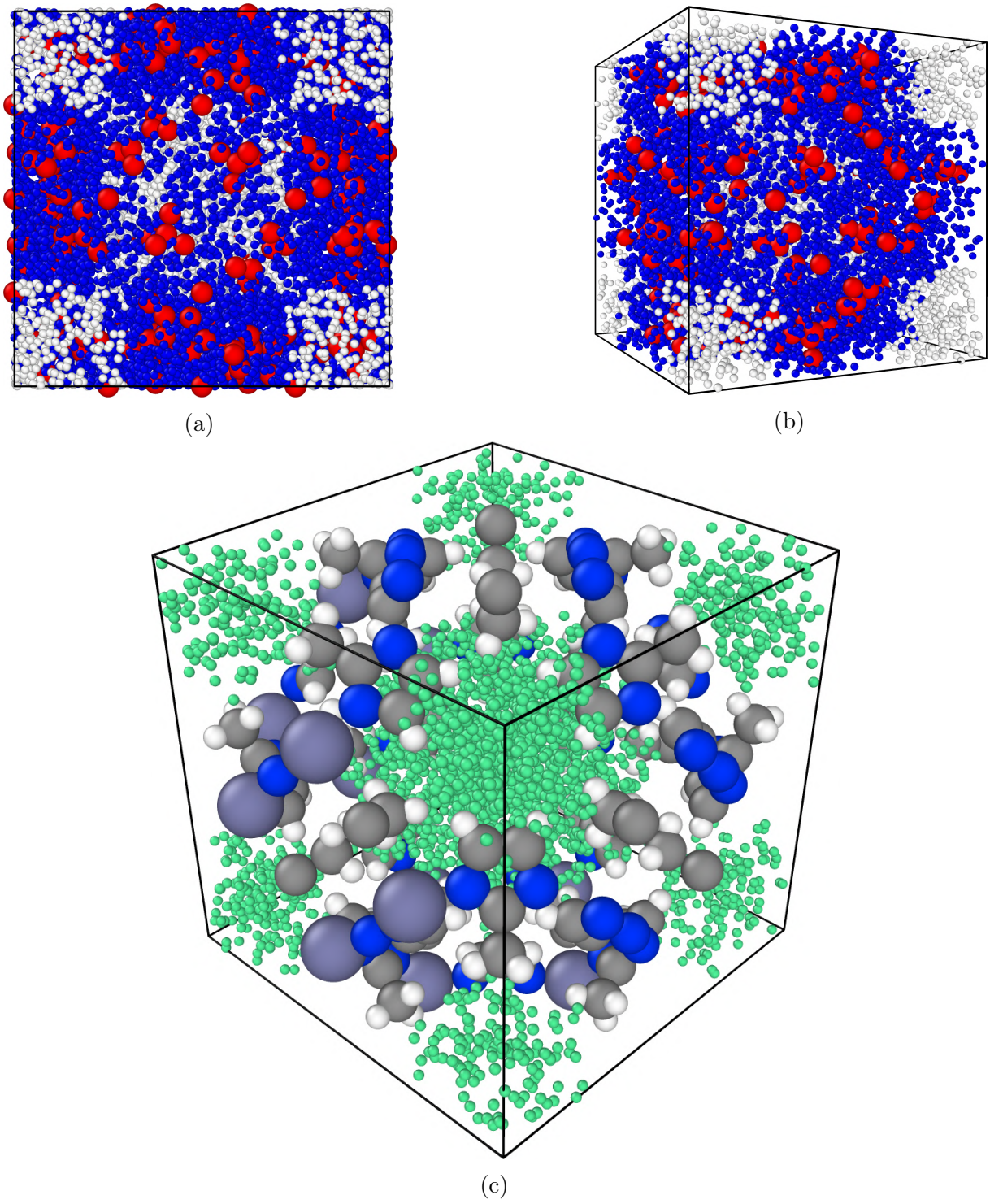

(a) (b) (c)

Figure 4.6: Illustrations of the free volume in relation to the ZIF-8 unit cell. (a) and (b) ZIF-8 atoms in red, probe atoms inside free volume in white, and outside in blue. (c) Only probe atoms inside free volume in green, atoms of ZIF-8 following the conventional color code.

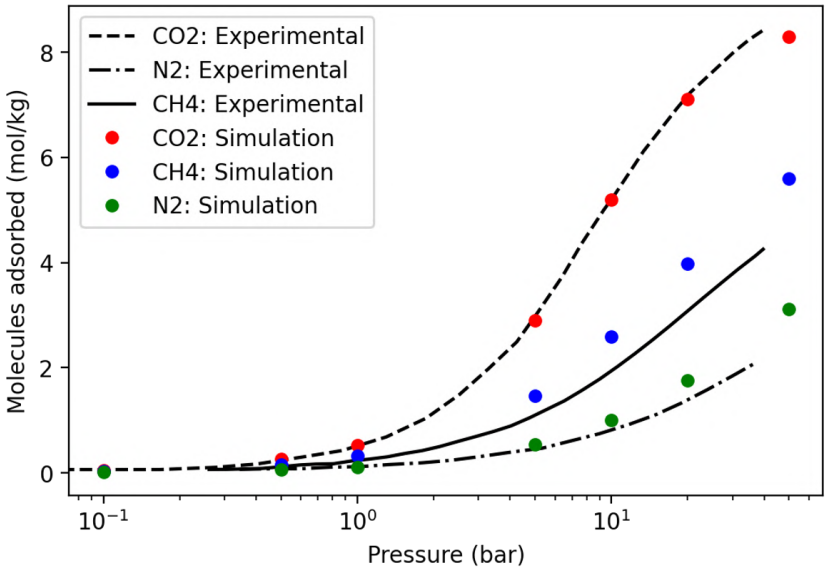

Figure 4.7: Adsorption isotherms simulated with GCMC at 303 K for different greenhouse gases and comparing the results with experimental data. Experimental data from [24].

molecules projected over the (001) plane. The presence of preferable adsorption sites is clearly noted with the presence of well-defined peaks in carbon density (carbon is also the molecule's center of mass). Besides, it is possible to note very well-defined pores, similar to what we observed when calculating the free volume. We can also note defined peaks at the pore edges in the oxygen density profile. However, we do not see two peaks equally distant and radially opposite to the position where we notice the carbon peak. Moreover, oxygen density is outer than carbon, indicating that adsorption probably occurs with one of the oxygens oriented through the MOF, while the other oxygen does not have a well-defined position.

With increasing pressure, we can see more intense peaks (more molecules adsorbed) and a new peak showing up in the center of the projection. This is probably associated with reaching the plateau of adsorption. All preferable sites are occupied, and we start seeing nucleation in the pore's center. This stands with a dual-site sorption mode.

The density profile can also be visualized using isosurfaces. Figure 4.9 shows these isosurfaces obtained for pressures of 10 bar (Figures 4.9a and 4.9b) and 50 bar (Figure 4.9c) in red together with ZIF-8 atoms. For these visualizations, we only plot the surfaces in the center pore, not showing the surfaces at the corners to facilitate the visualization.

Figure 4.9a shows an isosurface for a low value of density (1×10^{-6}Å^{-3}), illustrating the spherical distribution around the center that represents the pore of the framework. In Figure 4.9b, we have the isosurface for a high-density value (8×10^{-5}Å^{-3}) illustrating only the most intense peaks, the preferable sites. We can clearly correlate these sites with the organic linkers rings, i.e., with the imidazole. In agreement with our previous ab initio results that presented this site had the lowest energy of adsorption, and with previous

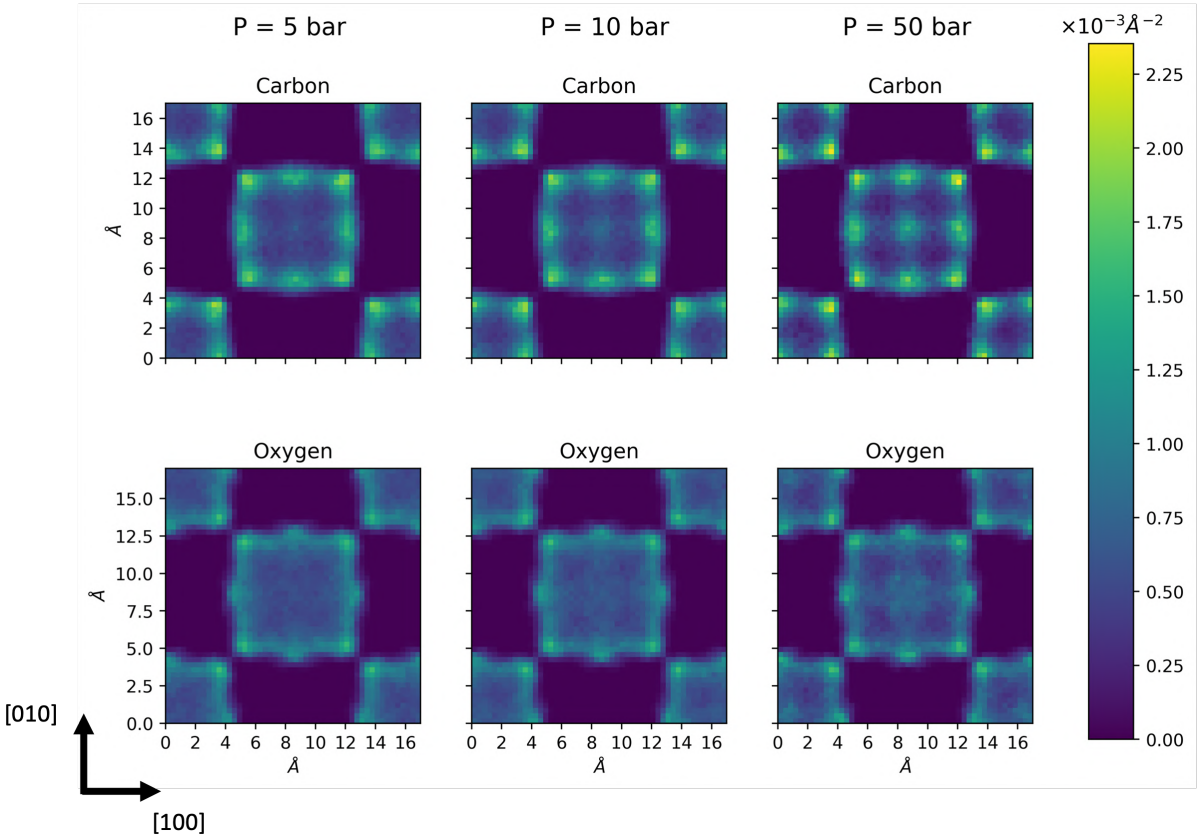

Figure 4.8: Local density of adsorbed CO_2 atoms projected over the (001) plane. Each column corresponds to different pressures, going from 5 to 50 bar. The first row represents the density of carbon atoms, which is also the density of the molecule's center of mass. The second row represents the density of the oxygen atoms.

literature results that indicate the interaction of CO_2 with imidazole is more favorable than with Zn clusters [103, 104]

Lastly, Figure 4.9c shows the high-value isosurface (8×10^{-5}Å^{-3}) for the highest pressure explored (50 bar). In fact, we can see a nucleation at the center of the pore, as the projection suggested.

4.4.2 Methane Adsorption

Extending this analysis through CH_4 adsorption, Figure 4.10a shows a projection of the local density of the adsorbed CH_4 molecules over the (001) plane. A similar adsorption profile is observed, with preferable sites noted at the edges of the pore. Figure 4.10b shows the isosurfaces in yellow for high-density values plotted along with ZIF-8 atoms, indicating that, once again, the preferable sites correlate with the imidazole rings. Note also that for higher pressures, we do not see relevant nucleation at the center of the pore, probably because the plateau of adsorption was not reached in this range of pressure explored.

4.4.3 Nitrogen Adsorption

Similar behavior is observed for N_2 adsorption. Figures 4.11a and 4.11b show the density profile over (001) plane and the high isosurfaces in green, again suggesting preferable sites at the edges of the cavity and correlated with the imidazole rings. Similar to what was seen for CH_4, we do not observe nucleation for higher pressures as we could observe for CO_2.

4.4.4 Interaction Energy

To explore more about the mechanisms of adsorption, the energy profile of the interaction between guest molecules and the framework was calculated, displacing the molecule over the (001) plane at the center of the framework. For the molecules of CO_2 and N_2, modeled as three-site molecules, we minimized the system's energy with the molecule near the imidazole ring to find the orientation of less energy. The molecule aligned parallel to the [001] orientation minimizes the system's energy. Displacing the molecule oriented in that way in the main diagonal, the molecule will be near two imidazole rings at the edges and also will be at the center of the unit cell. That way, high symmetry points are embraced together with preferable adsorption sites. The positions of the guest molecule in the framework over the displacement are illustrated in Fig. 4.12.

The energy profiles are reported in Fig. 4.13. Indeed, the minima of energy happen at the edges of the cavity, near the imidazole rings. Because of the cubic symmetry of the framework, the sites have the same energy, indicating homogeneous sites. Moreover, the energy follows the pattern observed in the adsorption isotherms; the lowest energy,

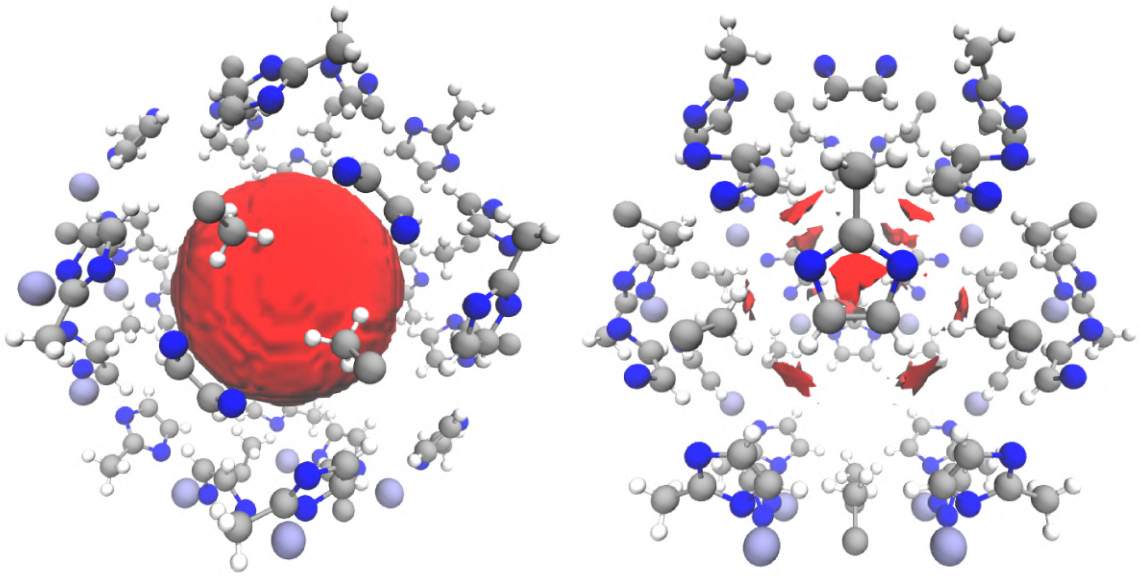

(a) (b)

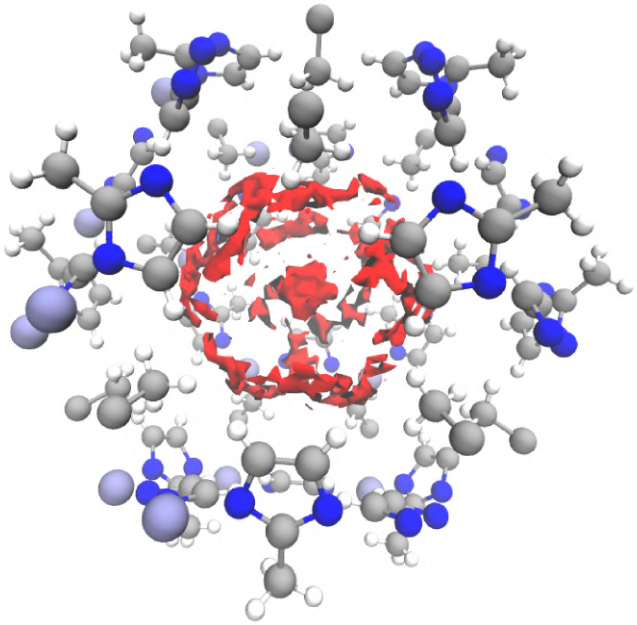

(c)

Figure 4.9: Isosurfaces of the local density of the center of mass of CO_2 molecules in red plotted alongside with the ZIF-8 unit cell following the default color code. (a) and (b) Isosurfaces for a pressure of 10 bar. In (a), we have an isosurface for a low-density value, where it is possible to note that adsorption occurs at the pores. In (b), we have an isosurface of high-density value, showing that the preferable sites are correlated with the imidazole rings. (c) Isosurfaces for high-density values for a pressure of 50 bar, showing nucleation at the center of the pore.

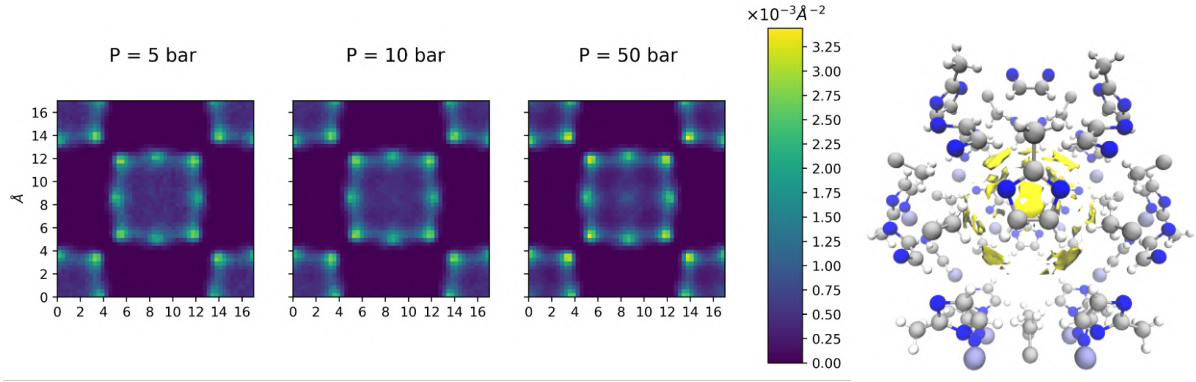

(a) (b)

Figure 4.10: (a) Projection of the local density of atoms of CH_4 over the (001) plane. Each column corresponds to different pressures, as indicated in the figure. (b) Yellow surface: high-value isosurfaces of the local density of atoms of CH_4 indicating the preferable sites where the adsorption occurs.

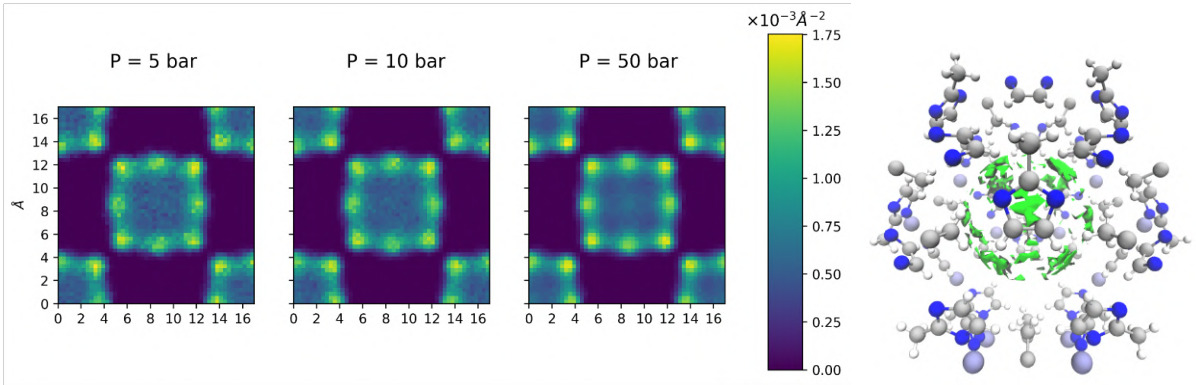

(a) (b)

Figure 4.11: (a) Projection of the local density of atoms of N_2 over the (001) plane. Each column corresponds to different pressures, as indicated in the figure. (b) Green surface: high-value isosurfaces of the local density of atoms of N_2 indicating the preferable sites where the adsorption occurs.

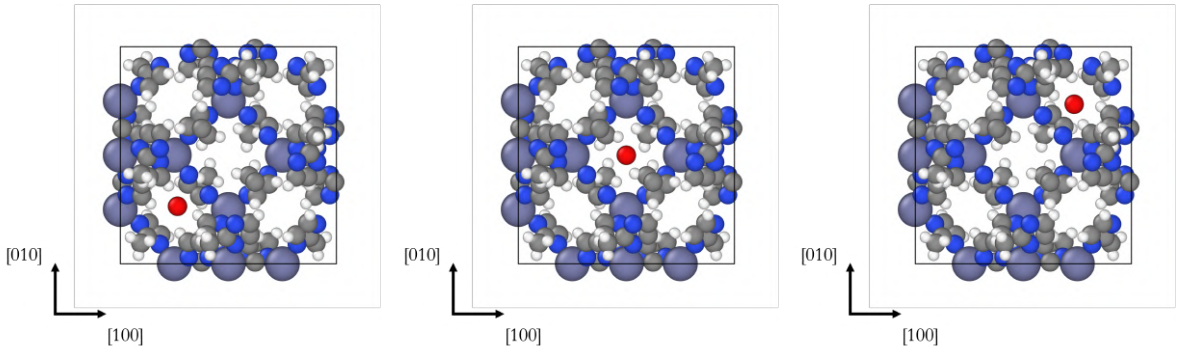

(a) (b) (c)

Figure 4.12: Illustration indicating the positions of guest molecules in calculating the interaction energy between the guest molecule and the framework. Guest molecule is positioned (a) near one imidazole ring (one preferable site) (b) at the center of the unit cell (where the displacement equals 0) (c) over the diametrically opposite imidazole ring.

for CO_2, is the molecule we see adsorbs more. This also indicates that ZIF-8 might have good selectivity for CO_2 over N_2 since there is a considerable difference in the adsorption energy for both species. For higher pressures, nucleation of the CO_2 molecules is seen in the system. For that reason, a local minimum of energy is also expected in the center of the cavity, which was not observed – indicating that nucleation happens because of an interaction of the CO_2 molecules in the adsorbed phase. This interaction was negligible for CH_4 and N_2, where we could not observe the nucleation effect at the pressure range explored.

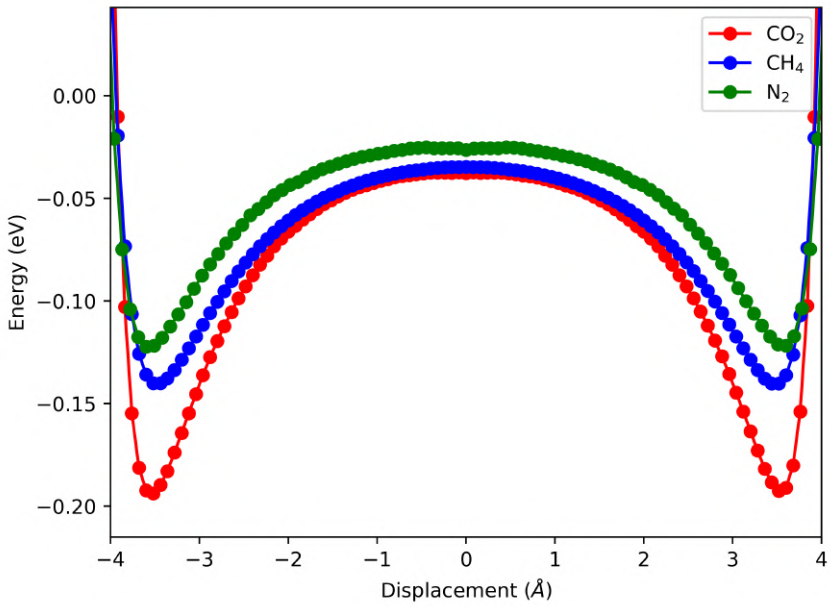

Figure 4.13: Interaction energy considering only van der Waals and Coulombic interactions between different guest molecules and the framework. The displacement is calculated in relation to the center of the unit cell, and the positions where the guest molecules were positioned are detailed in Fig. 4.12.

4.5 Fitted Adsorption Isotherms

Langmuir Isotherm

Adsorption isotherms can be fitted to well-established models in the literature to help understand adsorption mechanisms. In this work, we used the Langmuir model, given as follows [108]:

$$L(P) = M\frac{KP}{1+KP}, \tag{4.7}$$

where $L(P)$ is the amount adsorbed in a given pressure P, the parameter M stands for where the plateau of adsorption happens, while the parameter K is the equilibrium constant. This model predicts homogeneous adsorption sites with the same energy of adsorption. Another model explored was the Quadratic model, given by:

$$L(P) = M\frac{(K_a + 2K_bP)P}{1+K_aP+K_bP^2}, \tag{4.8}$$

a model that generalizes the Langmuir one with to K parameters, indicating two possible adsorption sites with different equilibrium constants. In fact, this model is used when the interaction of molecules in the adsorbed phase originates a new site. We opted to use these models since they resulted in an outstanding fit to the desired curves, helping us understand the adsorption process involved in each case.

Figure 4.14 shows that the Langmuir model was enough to fit very accurate data for CH_4 and N_2 adsorption. As discussed before, for the pressures explored, the interaction between molecules in the adsorbed phase was insufficient for the nucleation process to be seen. As for CO_2 adsorption, the data could not be fitted using only the Langmuir model (root mean squared error (RMSE) = 0.23 mol/kg), being necessary the use of the Quadratic model, indicating, once again, that the interactions of molecules in the adsorption phase are very relevant. The fitted parameters are reported in Table 4.5 together with the RMSE coefficient indicating fitting quality. Note that K_b is relatively low for CO_2 but it starts to be significant, while for the other isotherms only one adsorption energy was capable of capturing the isotherm tendency. Moreover, these fitted isotherms will be used in IAST. Therefore, we fitted the isotherms using absolute adsorption, which means data here is slightly different from data presented in Figure 4.7.

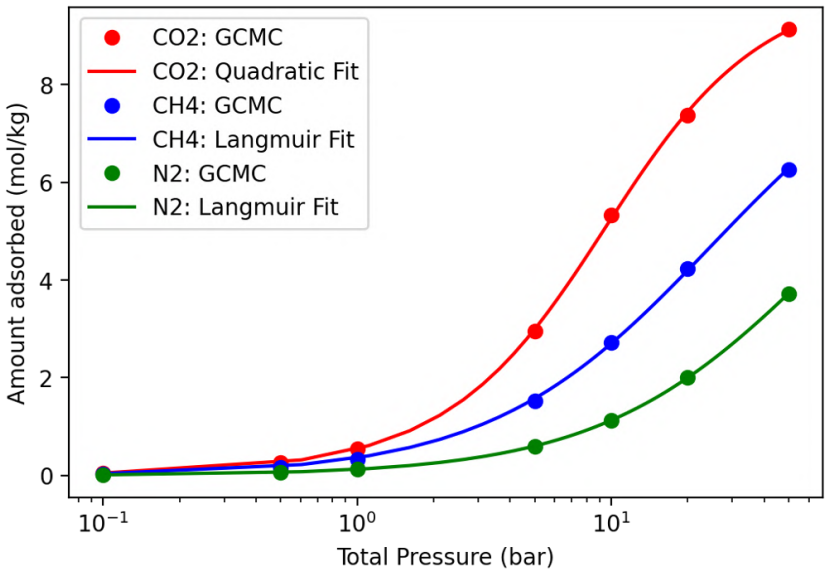

Figure 4.14: Adsorption isotherms calculated with GCMC for 303 K for different greenhouse gases and the respective model that fitted better the data. For CO_2, the best model that fitted our simulations was the Quadratic model, indicating a relevant interaction of molecules in the adsorbed phase. While for CH_4 and N_2, the Langmuir model accurately described the data, indicating homogeneous adsorption.

Table 4.5: Parameters obtained fitting the unique species adsorption isotherms using Langmuir and Quadratic models.

Isotherm	M (mol·kg^{-1})	K (mol·kg^{-1}·bar^{-1})	K_a (mol·kg^{-1}·bar^{-1})	K_b (mol·kg^{-1}·bar^{-2})	RMSE (mol·kg^{-1})
CO_2	5.07	-	0.10	0.01	0.04
CH_4	9.41	0.04	-	-	0.03
N_2	8.76	0.02	-	-	0.001

4.6 Binary Mixtures Adsorption Isotherms

Selectivity

From binary mixture reservoirs, a property of interest is calculating the selectivity of our framework, i.e., how many molecules from a species are selected over the other. We calculated the selectivity, as usual, using the following equation:

$$S_{ij} = \frac{x_i}{x_j}\frac{y_j}{y_i}, \tag{4.9}$$

where S_{ij} is the selectivity of species i over j, x_i is the molar fraction of the species i in the adsorbed phase, and y_i is the molar fraction of the species i in the gas phase.

Ideal Adsorbed Solution Theory

Experimentally, it is not easy to control thermodynamic conditions of mixtures of gases. Consequently, experimental isotherms of binary mixtures are hard to obtain. In order to predict the selectivity based on unique species isotherms the Ideal Adsorbed Solution Theory (IAST) might be used [109]. This theory assumes that thermodynamic properties changes of the adsorbent are negligible in the adsorption process, all adsorbed species have the same surface area available, and the Gibbs definition of adsorption applies. With that approximation of an ideal adsorbed solution, it is possible to obtain the adsorption of each specie in a binary mixture at a determined concentration and total pressure from the unique species experimentally measured isotherms. More details on this theory are explored in Appendix C. To calculate the mixtures adsorptions in this work, we used a Python package: pyIAST [110].

It is important to remark that the absolute adsorption must be considered instead of the excess adsorption to use the IAST. Moreover, a function describing the unique species isotherms is also needed; experimental data on unique species isotherms are not enough. Usually, we need to use an already established model to fit data [2].

The IAST allows us to calculate adsorptions of mixtures faster at different thermodynamic conditions, without the need to simulate several reservoirs. However, the extension of this method depends on the validity of the assumptions made. Therefore, we performed a validation of the use of this method in ZIF-8 for mixtures of CO_2 by comparing its results to results from GCMC.

To validate the IAST model for ZIF-8, we performed binary GCMC calculations in mixtures of CO_2 and CH_4, and also in mixtures of CO_2 and N_2. Shifted chemical potential and partial density obtained for each mixture are reported in Appendix B

[2] In particular, empirical models present a non-linear behavior for low pressures, being not thermodynamically consistent. Hence, the use of empirical models is not recommended in IAST.

CO_2 and CH_4 mixtures

The results considering a 50/50 mixture of CO_2 and CH_4, varying the total pressure, are given in Fig. 4.15a). Binary GCMC results agree with IAST, apart from some deviations for higher pressures. These deviations are expected since information about the unique species isotherms in even higher pressures is needed for a good description of IAST. As for selectivity, Fig. 4.15b) also shows a good agreement, especially for pressures in the range of 1 bar to 20 bar.

In Fig. 4.16, data for a mixture of CO_2 and CH_4 at a fixed total pressure of 20 bar is shown, varying the molar fraction of the gases. Again, the two methodologies agree, satisfactorily describing the isotherms and selectivity. Deviations can be seen for low or high concentrations of CH_4; in these conditions, the mixture is not ideal anymore, violating IAST hypotheses.

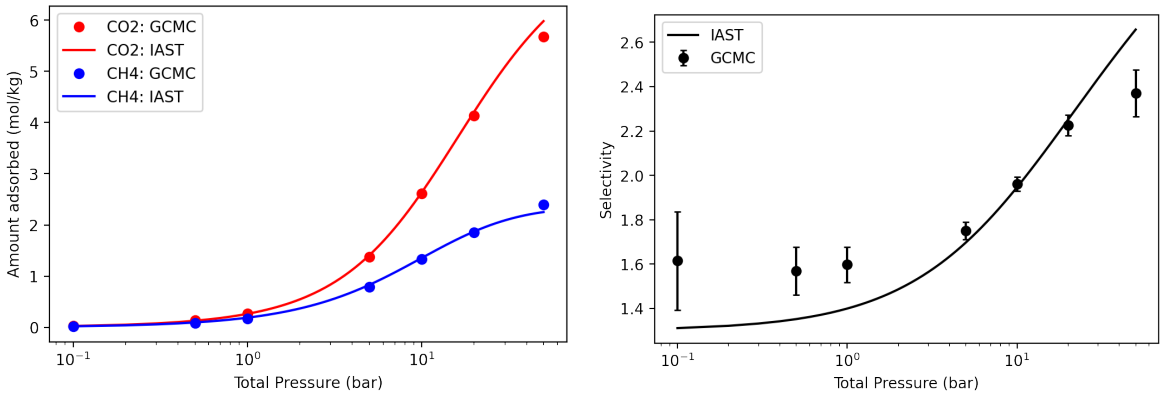

(a) (b)

Figure 4.15: Comparison of the results obtained from binary GCMC and IAST for the mixture's adsorption isotherms for CO_2 and CH_4 in a 50/50 mixture. (a) Direct comparison of the isotherms. (b) Comparison of the selectivity.

CO_2 and N_2 mixtures

In Figures. 4.17 and 4.18, we have data for mixtures of CO_2 and N_2 at a 50/50 mixture and at a fixed pressure of 20 bar, varying the molar fraction, respectively. Once again, IAST can very well capture the isotherms and the system's selectivity. For very low or very high concentrations of N_2, some deviations are seen in relation to binary GCMC. This is expected since the mixture is not ideal in these conditions, making one of the hypotheses from IAST invalid. We highlight that the selectivity for mixtures of CO_2 and N_2 are indeed high, indicating why this is a promising material, even for high concentrations of N_2.

With that we finish the investigation of adsorption properties of several greenhouse gases in pristine ZIF-8. DFT results are in agreement with classical results regarding CO_2 preferable site and energy. Indicating that the FF used describes satisfactorily our system.

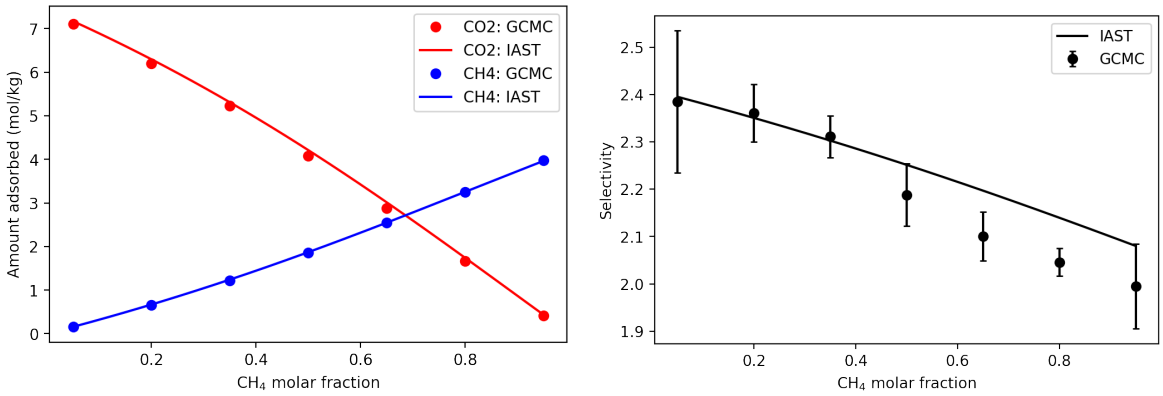

(a) (b)

Figure 4.16: Comparison of the results obtained from binary GCMC and IAST for the mixture's adsorption isotherms for CO_2 and CH_4 in a mixture of total pressure of 20 bar, varying the molar fraction of the components. (a) Direct comparison of the isotherms. (b) Comparison of the selectivity.

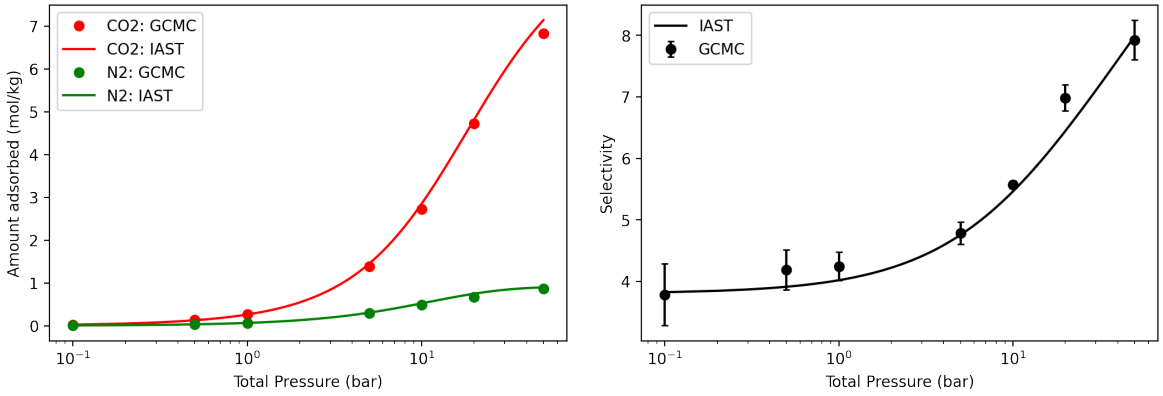

(a) (b)

Figure 4.17: Comparison of the results obtained from binary GCMC and IAST for the mixture's adsorption isotherms for CO_2 and N_2 in a 50/50 mixture. (a) Direct comparison of the isotherms. (b) Comparison of the selectivity.

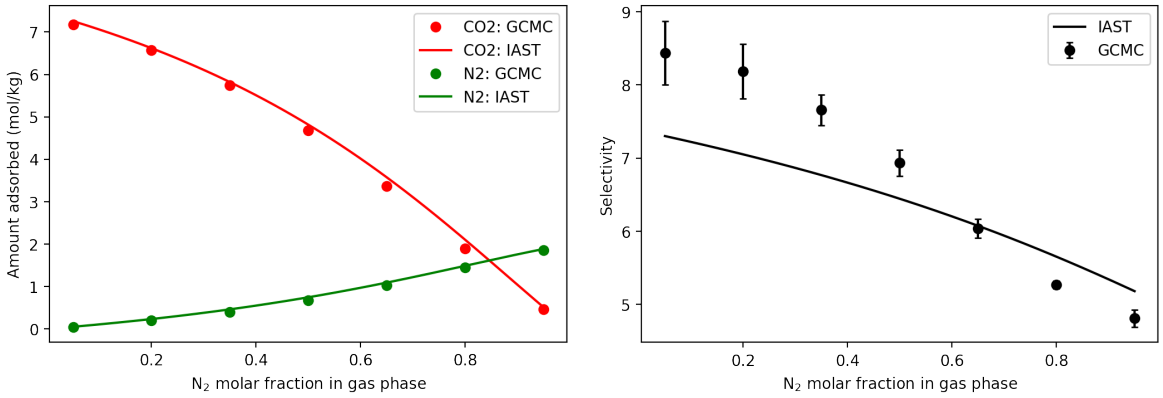

(a) (b)

Figure 4.18: Comparison of the results obtained from binary GCMC and IAST for the mixture's adsorption isotherms for CO_2 and N_2 in a mixture of total pressure of 20 bar, varying the molar fraction of the components. (a) Direct comparison of the isotherms. (b) Comparison of the selectivity.

Moreover, experimental adsorption isotherms can be very accurately be reproduced by GCMC. Using GCMC we could also calculate the selectivity over several mixtures of gases and validate the use of the IAST for this MOF. Comparing selectivity indexes we can infer that in fact it is a very promising material to capture carbon from the flue gas. However, it still needs a higher selectivity to be more competitive with actual technologies that already dominates the market.

4.7 Transport Properties

Transport properties can also help us understand better the interaction of the guest molecule with the framework. Thus, understanding better the separation process and even thinking of new ways of separating gas mixtures. One example will be explored further, we investigated the dynamics of the pore size in ZIF-8. Depending on the size of the pore only a few molecules can diffuse through it, with that, we can separate molecules of different sizes.

The diffusion coefficient for CO_2, CH_4, and N_2 for different loadings were explored. First, to relax the framework using the model proposed, equilibration of the ZIF-8 over 1 ns in the NPT ensemble, at $T = 303$ K and $P = 1$ bar, followed by a 10 ns equilibration in the NVE ensemble was made.

Using this structure, we load the ZIF-8 with a different number of guest molecules per unit cell based on previous simulations with GCMC. In that way, the structure is loaded with a reasonable number of molecules and we know the equivalent pressure in the system. To relax the framework using the model proposed, equilibration of the ZIF-8 over 1 ns in the NPT ensemble, at $T = 303$ K and $P = 1$ bar, followed by a 10 ns equilibration in the

NVE ensemble was made. After loading the system, equilibration in NVT is performed for 0.5 ns to reach the target temperature of 303 K. Following that, a production phase of 11 ns is computed in the NVE ensemble where 10 MSDs are computed over different time origins to average out the self-diffusion coefficient.

In order to investigate the impact of volume changes in ZIF-8 while loaded, we also equilibrated the system in the NPT ensemble at the equivalent pressure in the system after the NVT equilibration. In sequence, a 3 ns production phase in the NPT ensemble was considered to determine the average volume of the framework. The 11 ns production phase in the NVE ensemble was then simulated to compute the MSDs.

4.7.1 Self-diffusion coefficients

The self-diffusion coefficient is a transport property of interest. It might help us understand the dynamics of the guest molecules inside our framework. To obtain this coefficient, we used Einstein's equation, which relates the diffusion coefficient with the mean square displacement (MSD) of the particles [111]

$$D = \lim_{t\to\infty} \frac{1}{6t} \langle \frac{1}{N} \sum_{k=1}^{N} |\mathbf{r}_k(t) - \mathbf{r}_k(t_0)|^2 \rangle \,, \tag{4.10}$$

where D is the self-diffusion coefficient, $\mathbf{r}_k(t)$ is the position vector of guest molecule k at time t. The value of D over all the N sorbed molecules and over multiple time origins t_0 is averaged. The 6 in the denominator is related to the system's dimensionality ($2N$).

Note that Einstein's equation assumes a linear relation between D and the MSD. This is only achieved in a Fickian diffusive regime. Logarithm plots of the MSD over time were also investigated to obtain the diffusion regime of the guest molecules explored.

Calculated diffusion coefficients are shown in Fig. 4.19 for the three gases explored. Firstly, using experimental volume or the average volume obtained from our model does not significantly impact the coefficients. Comparing these results with experimental data, for CO_2, differences of almost three times can be noticed. This is expected and discussed in the article that proposes the FF used in our simulations [26]. The method used for calculating the partial charges in ZIF-8 can capture the adsorption of CO_2, but cannot accurately describe the diffusion of this gas. Even with this FF, the order of the coefficient for different loads can still be estimated. As for CH_4, since it does not have a dipole moment, a better description is given with this FF, in agreement with experimental data. To the best of our knowledge, there is no experimental data for N_2. Therefore, the results were compared with another MD simulation considering a proper FF. Again some deviations can be seen, which is expected since our FF was designed to describe adsorption accurately, not diffusion.

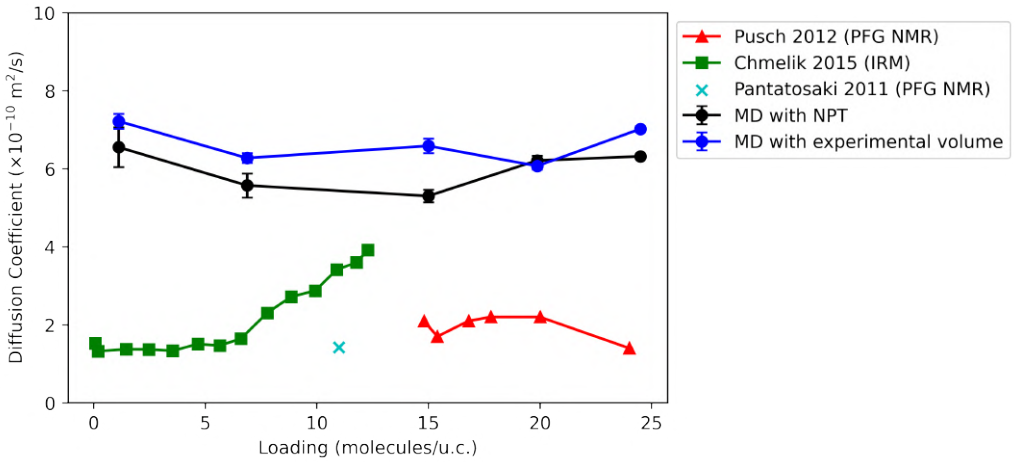

(a)

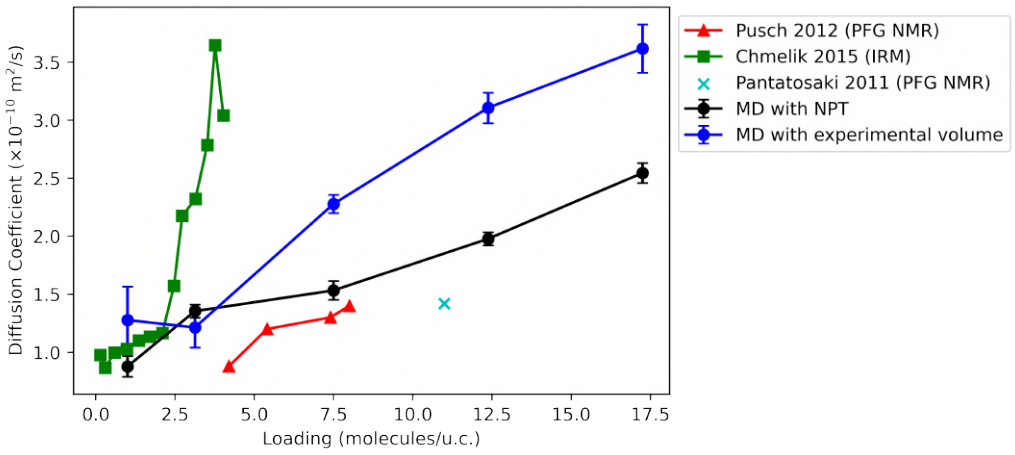

(b)

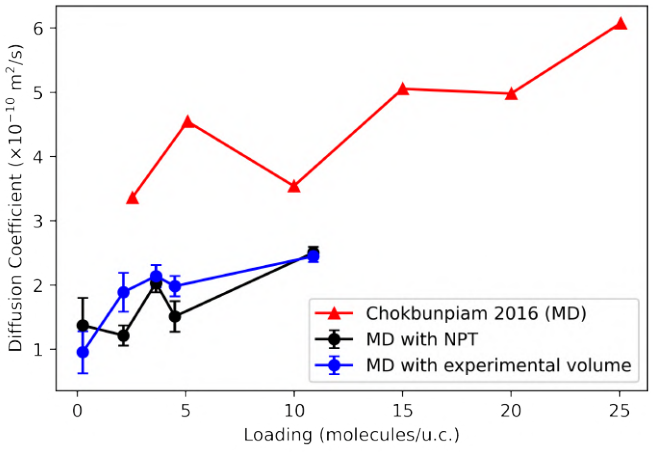

(c)

Figure 4.19: Self-diffusion coefficients calculated for different greenhouse gases at different loadings using the experimental volume and the volume obtained through an NPT relaxation and a comparison with experimental data, when available, or other simulations. (a) Diffusion coefficient for CO_2. Experimental data from [112, 113, 114]. (b) Diffusion coefficient for CH_4. Experimental data from [112, 113, 114]. (c) Diffusion coefficient for N_2. Other simulation data from [78].

4.8 Pore diameter dynamics

The pore diameter in ZIF-8 has a huge impact on the transport of molecules. A small pore might let only a few guest molecules to diffuse through the framework, allowing new methods of selecting certain species. Therefore, we used MD simulations using the NVT, NPT, and NVE ensembles to understand the impact of temperature on the large pore diameter. The diameter d can be estimated from the positions of the hydrogen atoms, as Figure 4.20 suggests, using the following equation [28]

$$d = 2\frac{r_1 r_2 r_3}{\sqrt{(r_1+r_2+r_3)(r_2+r_3-r_1)(r_3+r_1-r_2)(r_1+r_2-r_3)}} - 2r_H, \tag{4.11}$$

where r_1, r_2, and r_3 are the distances highlighted in Figure 4.20, and r_H is the van der Waals radius for hydrogen, considered 1.2 Å.

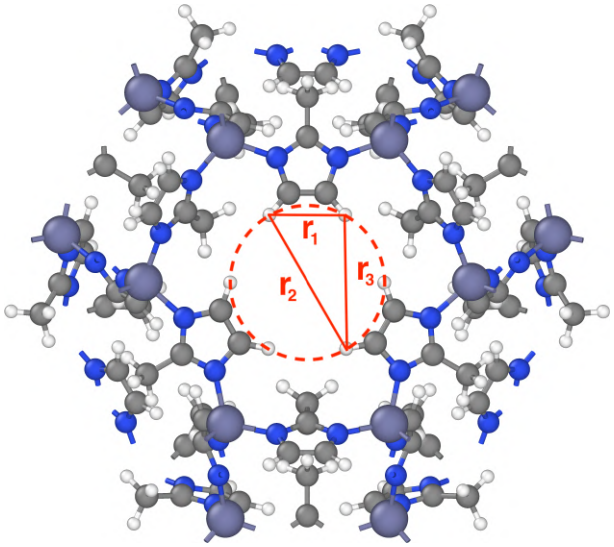

Figure 4.20: Illustration on how to estimate the large pore diameter using the distances from hydrogen atoms.

For 303 K, 350 K, 400 K, 450 K, and 500 K, we simulate ZIF-8 at 0 bar. First, we equilibrate the system for 1 ns in the NVT ensemble to achieve the target temperature, followed by a 1 ns equilibration in the NPT ensemble to achieve the target pressure. In sequence, a 5 ns production phase in the NVE ensemble is considered to average out the diameter.

MD simulations were performed to investigate the temperature response of ZIF-8 in a range of 303 K to 500 K. It was not possible to see considerable thermal expansion in our simulations, in agreement with experimental data at this range of temperature. As for the pore diameter's distribution, the influence of temperature leads to an increase of 0.11 Å in the average and an increase of 0.69 Å in the standard deviation, as seen in Tab. 4.6.

Indicating a broadening of the distribution, which can be seen in Fig. 4.21.

Table 4.6: Average of the pore diameter (d) and the corresponding standard deviation for different temperatures at atmospheric pressure

T (K)	d_{avg}(Å)	σ_d(Å)
303	3.47	1.02
350	3.49	1.38
400	3.53	1.22
450	3.55	1.45
500	3.58	1.71

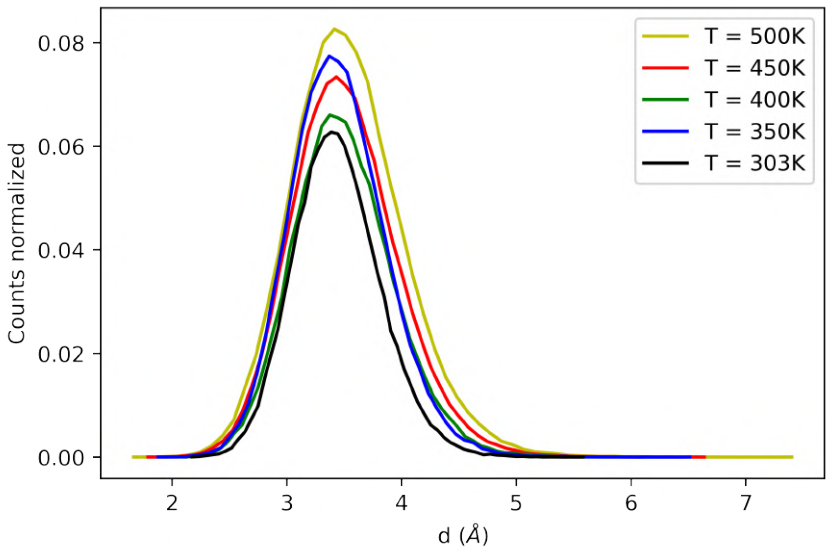

Figure 4.21: Distribution of pore diameter over MD simulations normalized for different temperatures, illustrating the broadening of the distribution as the temperature increases.

These variations in the pore diameter is interesting to induce other methods of separation based on the actual size of molecules. Molecules with a diameter greater than the pore size can not easily diffuse through the material.

Transport and dynamic properties helps us to better understand the dynamic interaction between guest molecules and the framework of interest. We could even get self-diffusion coefficients at the same order of magnitude of experimental measurements using a FF designed to reproduce adsorption properties. Additionally, modelling the pore flexibility we can also think in ZIF-8 as a promising material to induce other separation methods, not only based in adsorption.

4.8.1 Conclusion

In this chapter we explore pristine ZIF-8 using molecular modelling techniques, going from ab initio (DFT) calculations to atomistic simulations (MC and MD). From first-

principles calculations, we characterized ZIF-8 as a wide-gap semiconductor with a direct band gap of 3.964 eV. CO_2 adsorption sites was explored using nonlocal functionals for accounting for van der Waals interactions, pushing the boundaries of literature on this type of calculation for these materials. DFT calculations let us find preferable adsorption sites correlated with the organic linker and also validate the classical force field used.

From atomistic simulations, we obtained adsorption isotherms for CO_2, CH_4, and N_2 using GCMC. The local density of adsorbed atoms preferable sites were obtained and in agreement with first-principles calculations. In particular, for carbon dioxide at higher pressures, a nucleating process at the center of the pores was observed, indicating a dual-sorption mode. Moreover, considering binary mixtures, we validated the use of the IAST, comparing results using this theory with GCMC simulations. From these binary mixtures, we calculate the selectivity regarding carbon capture, where bulk ZIF-8, despite presenting outstanding indicators, is still insufficient to be economically viable versus amine absorption.

5 | Thermally Modified ZIF-8

Bulk ZIF-8 displays notable characteristics for carbon capture. However, it appears to lack economic viability when compared to amine adsorption. Therefore, it becomes imperative to explore alternative methodologies for the modification of these frameworks, with the ultimate goal of enhancing their carbon capture capabilities. Thermal treatments emerge as particularly promising candidates in this pursuit, due to their cost-effectiveness and scalability. The use of molecular modelling to investigate these treatments can help identifying what exactly process enhances carbon capture and thereby guiding future research.

In this chapter we present results of simulations involving thermally modified ZIF-8. Recalling Figure 5.1 we investigated two different possible frameworks. For treatments near 525 °C we investigate the effect of methyl vacancies and its relation with CO_2 adsorption energy. For treatments near 900 °C a transition of the tetrahedral ZnN_4 sites to planar sites is induced. We modelled two possible frameworks to represent this structure. The first one is a doped graphene sheet, the second one a porphyrin-like framework with the less number of carbons possible to respect periodic boundary conditions. For both these structures, we investigate possible sites of CO_2 adsorption and calculate the partial charges to adapt a new classical FF that describes these frameworks. With this approximation we estimate the capacity of these structures to capture carbon and conclude that thermal treatments are really promising due to its small price, easy to scale up production and outstanding results.

5.1 Frameworks explored

As discussed in Chapter 1, ZIF-8 is a very promising material regarding carbon capture. In particular, it presents outstanding numbers regarding separating carbon from nitrogen, which is extremely relevant for capturing carbon from the flue gas. In this work, we explore several ZIF-8 structures in order to investigate better ZIF-8 adsorption properties and how modified structures can enhance carbon capture, going from pristine ZIF-8 to thermally modified frameworks treated at different temperatures.

Figure 5.1 illustrates the frameworks explored. First we start studying pristine ZIF-8, followed by the structures with methyl vacancies induced by treatments near 525 °C.

Finally, we investigate two-dimensional frameworks induced by treatments at much higher temperatures, near 900 °C, where we modelled two different possible structures. One is based on a graphene sheet doped with ZnN_4 sites. The second one models a porphyrin-like cell, which can satisfy periodic boundary conditions.

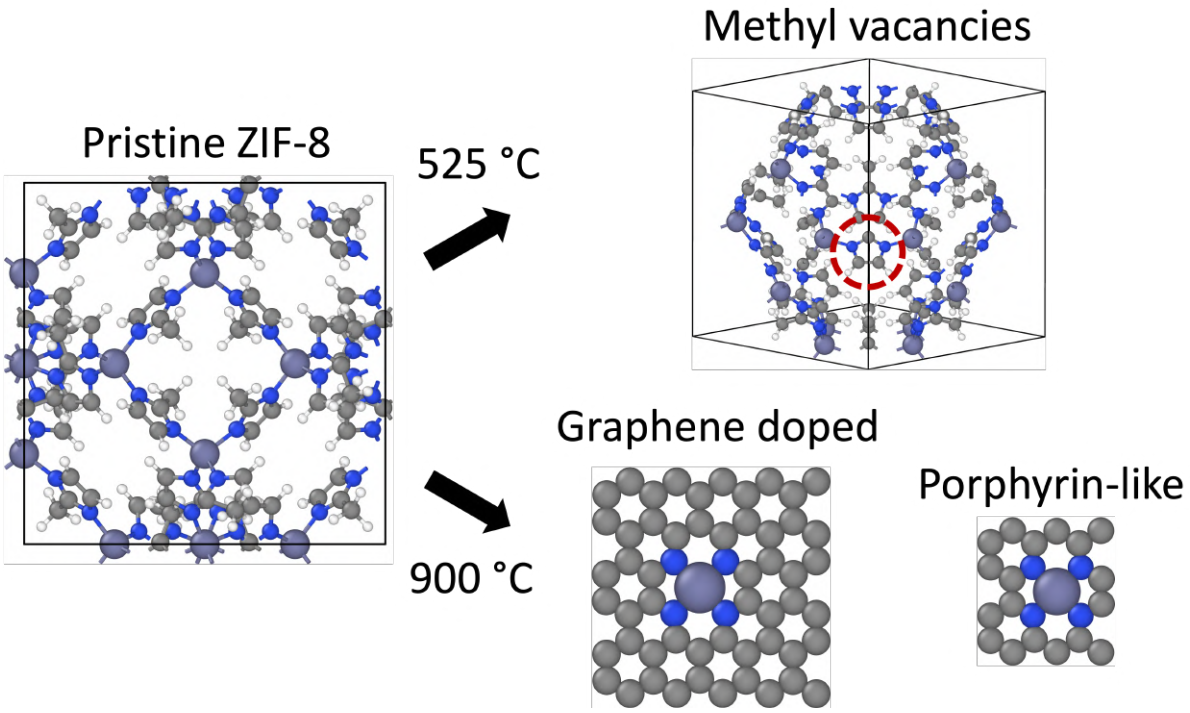

Figure 5.1: Representative schema of the frameworks explored in this work. Going from pristine ZIF-8 and illustrating different frameworks obtained after a thermal treatment. Treatments near 500 °C induces methyl vacancies highlighted inside the red circle. Treatments near 900 °C induces more drastic transformations to two-dimensional frameworks, our models consider two different possible frameworks. One is based in a graphene sheet doped with ZnN_4 sites and the other one is the minimum porphyrin-like cell to reproduce periodic boundary conditions.

5.2 Methyl vacancies

First, considering thermal treatments near 525 °C, we modeled the methyl vacancies proposed by Gadipelli et al. [33]. We considered defects at two different concentrations, one vacancy and three vacancies per unit cell. These vacancies are highlighted in the red dashed circles in Figure 5.2. Initial structural relaxation of both frameworks led to a slight rotation of the organic linkers close to the vacancies, but no significant distortion was noted overall. No changes in the cubic shape of the unit cell and the lattice parameter were observed.

For these frameworks, all the calculation parameters were kept the same as for pristine ZIF-8, and the same protocol was followed. Initially, we relaxed the structure with all

degrees of freedom, followed by an investigation of the electronic properties.

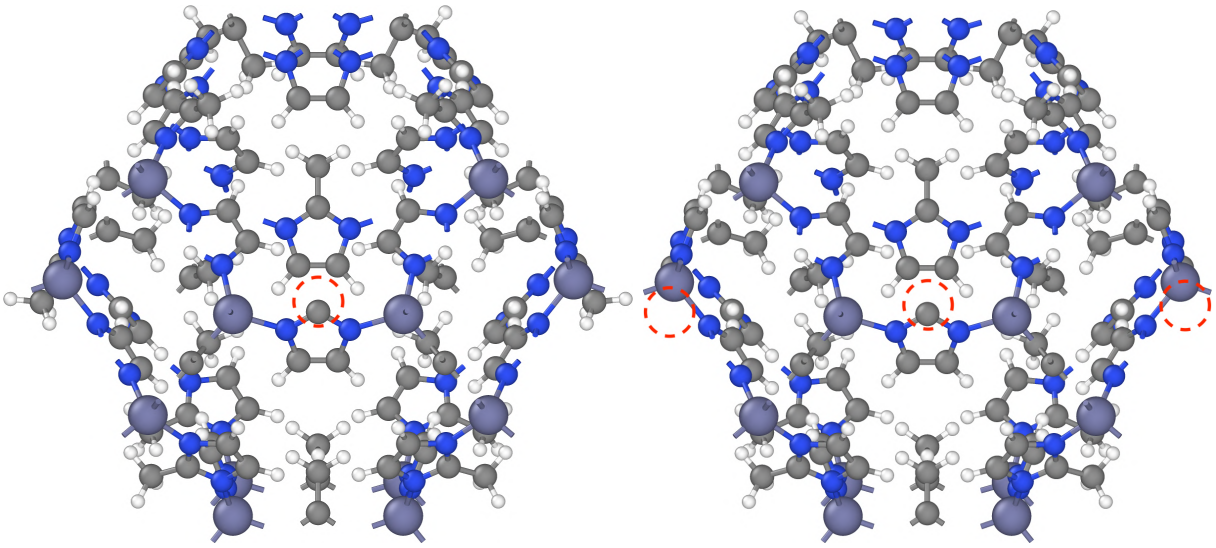

(a) (b)

Figure 5.2: Initial configurations for the structures with (a) 1 and (b) 3 methyl vacancies indicated by the red dashed circle.

Additionally, CO_2 adsorption energy was calculated using as the initial condition the previous preferable site obtained for pristine ZIF-8, near the imidazole ring. As Figure 5.3a shows, for the framework with one vacancy CO_2 preferable site moved slightly away from the vacancy. In contrast, for three vacancies, it moved in the direction of the vacancy. Both adsorption energies obtained are reported in Table 5.1. No significant increase or decrease can be attested compared to the energy for the same site with no defects. Which means even with the position of the preferable site changing slightly, for the different vacancies considered, the adsorption process is not considerably impacted by these defects.

Gadipelli et al. expected these vacancies would change considerably the electronic density of the framework, affecting the chemical bonds between Zn and N. However, this was not observed in our simulations and could possibly be the reason why interaction between CO_2 and the framework did not change significantly. One hypothesis is that despite not seeing an increase in the adsorption energy, methyl vacancies can change the diffusion barriers inside the pore and make more sites available for adsorption, explaining the increase in carbon dioxide uptake. More investigations must be done to understand the defects induced by treatments near 525 °C.

5.3 Two-dimensional frameworks

Since we could not see any major impacts on adsorption with the methyl vacancies we explored frameworks treated at even higher temperatures, where we have experimental evidences of two-dimensional frameworks [34].

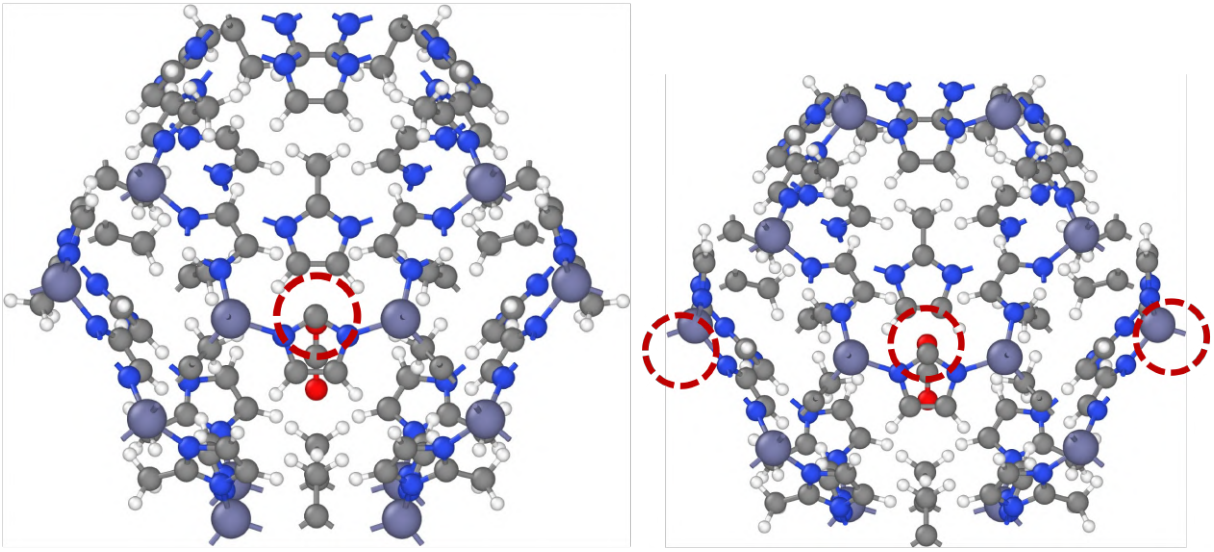

(a) (b)

Figure 5.3: Carbon dioxide adsorption sites explored for the frameworks with different concentrations of vacancies. (a) 1 methyl per unit cell. (b) 3 methyl per unit cell.

Table 5.1: Adsorption energies for carbon dioxide near the vacancies for both concentrations explored compared with the adsorption energy from pristine ZIF-8.

	E_{ads} (eV)
Imidazole ring (Pristine ZIF-8)	-0.352
1 methyl	-0.342
3 methyl	-0.351

We considered two different approaches to model the transformation from tetrahedral to porphyrin-like ZnN_4 centers indicated by Wang et al. [34]. Initially, a larger graphene sheet co-doped with Zn and N, as Figure 5.4a represents, was considered. Since PBC in all directions is being used, considering a larger graphene sheet might allow us to control for interactions of the guest molecules (later explored) with its image. A graphene sheet with 12.28 Å $\times$ 12.76Å was used. Furthermore, graphene properties are very well determined and explored in the literature, allowing us to understand similar properties of this framework compared with graphene results. This framework will be referred as doped graphene throughout this work.

Following, we simulated a porphyrin-like framework trying to be as close as possible to the stoichiometry of ZIF-8 while using PBC. However, even in this small possible unit cell, normalizing by the number of Zn, we still have more carbon than we would have in pristine ZIF-8. Figure 5.4b illustrates the framework modelled. Color code still follows the same pattern used before: zinc in purple, nitrogen in blue, and carbon in gray.

For calculations with these two-dimensional structures, a converged cutoff energy of 440 eV was considered together with a $5 \times 5 \times 1$ k-point sampling in the Brillouin zone obtained with the Monkhorst-Pack grid. The convergence criteria were chosen to be 10^{-6} eV and 0.01 eV $Å^{-1}$ for the electronic self-consistency cycles and structural optimizations, respectively. We considered a unit cell with 20 Å in the axis perpendicular to the sheet. This distance was also tested until the interaction with the image from PBC was negligible.

Additionally, we also calculated the partial charges for each atom in these frameworks using the Bader charge analysis implemented by Henkelman Group [115]. Using the electronic charge density, it uses a zero flux surface to divide atoms.

5.3.1 Electronic properties

Doped graphene

Considering defects induced by treatments near 900 °C as suggested by Wang et al. [34], we modeled two-dimensional structures with planar coordination between Zn and N. First, we modeled a graphene sheet doped with a cluster of Zn and N. An initial relaxation let us optimize the sheet's area and showed a stable structure. Figure 5.4a illustrates the structure obtained.

Figure 5.5 shows the total and partial density of states obtained for doped graphene, indicating a metallic material. The partial density of states indicates that orbitals from carbon are the ones available at the Fermi level.

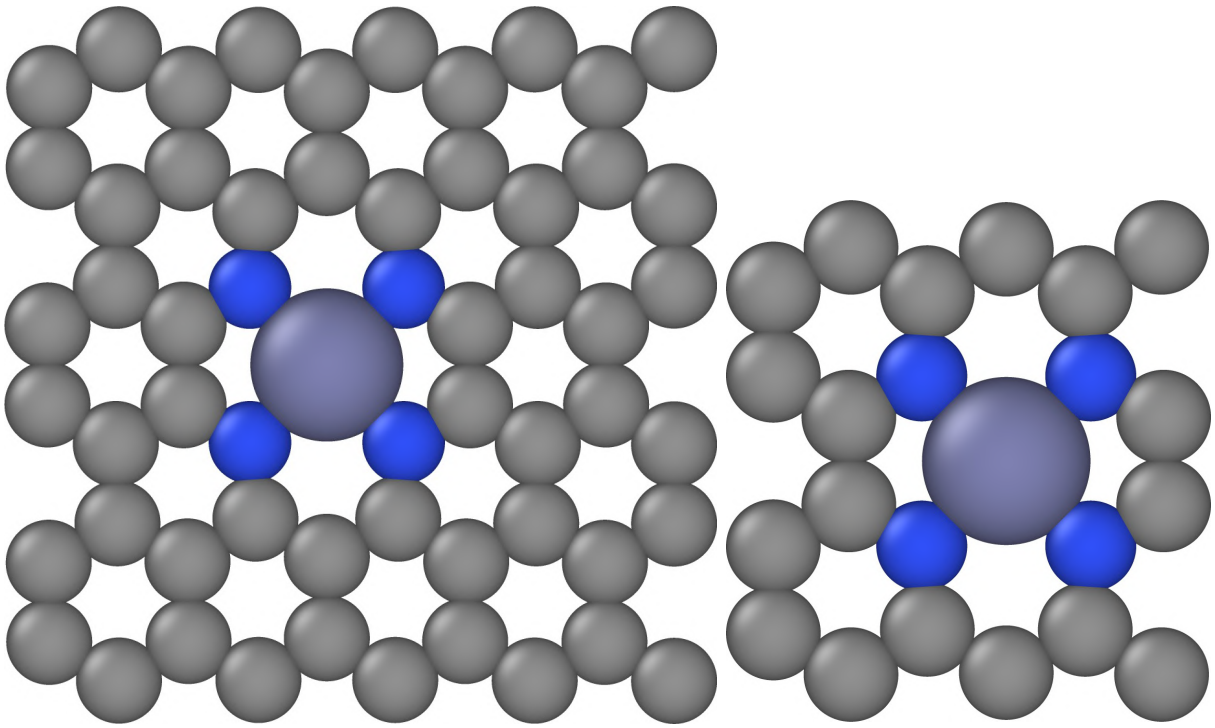

(a) (b)

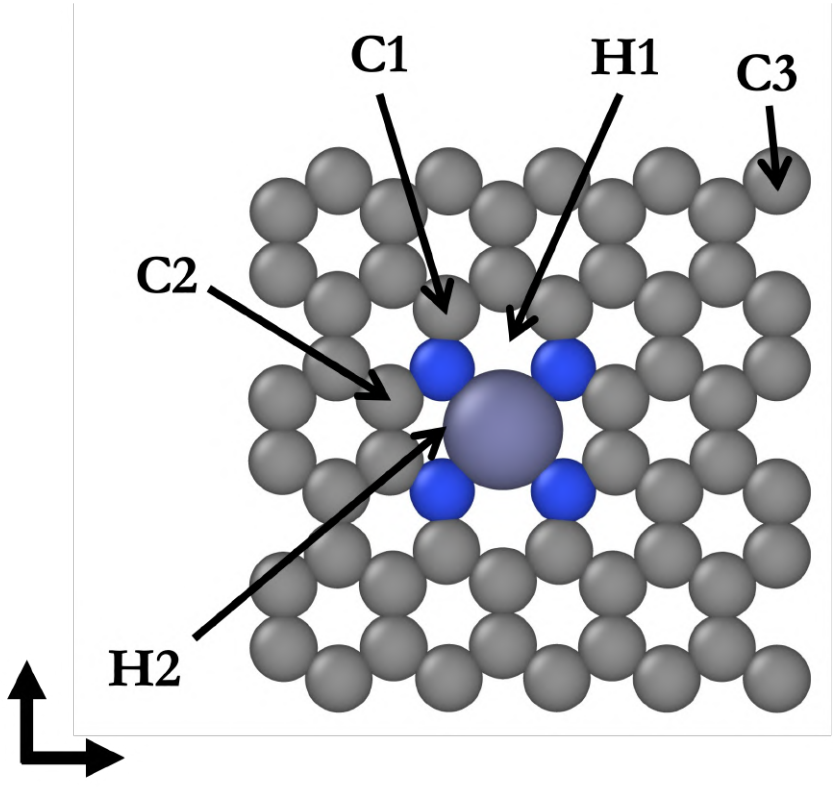

(c)

Figure 5.4: Structures modeled to explore frameworks with ZnN_4 transformed centers to planar coordinations. (a) Co-doped graphene with Zn and N. (b) Porphyrin-like structure. Color code: zinc in purple, nitrogen in blue, and carbon in gray. (c) Labels of the top and hollow sites for the two-dimensional frameworks.

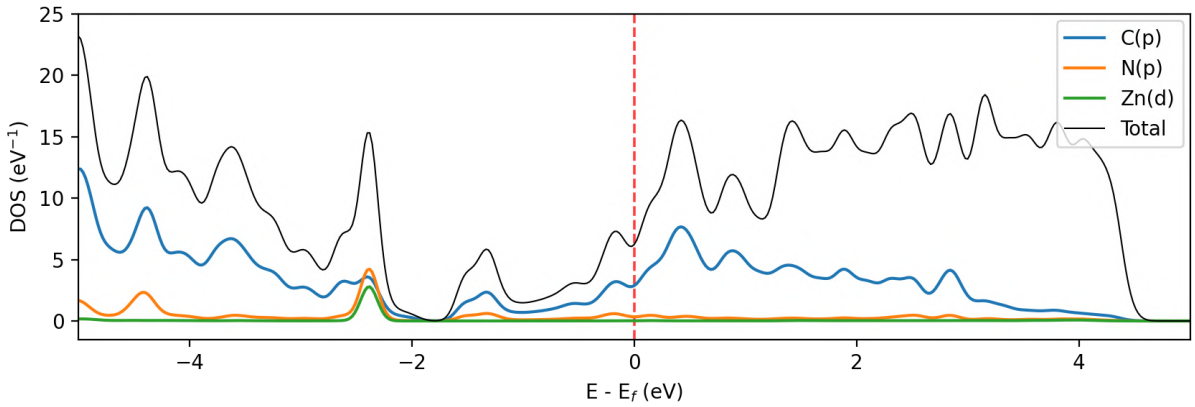

Figure 5.5: Total and projected density of states of doped graphene

Porphyrin-like

The second model considered was the porphyrin-like structure, illustrated in Figure 5.4b. Relaxations also led us to optimize the area of the sheet and showed a stable structure. Figure 5.6 shows the PDOS obtained for this structure, again with metallic behavior. However, with this structure with much more concentrated doping clusters, it is hard to see the baseline of graphene total DOS, as we could observe for doped graphene. Note that for this framework, orbitals available at the fermi level are from carbon and nitrogen.

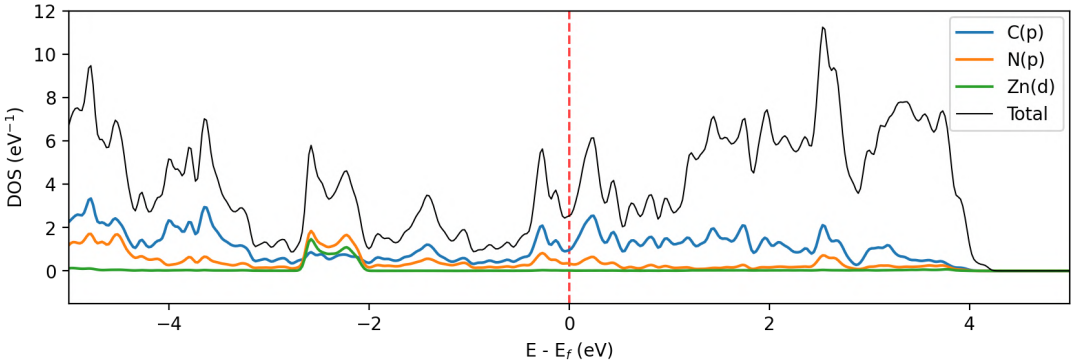

Figure 5.6: Total and projected density of states of porphyrin-like structure.

5.3.2 Carbon Dioxide Adsorption

With both frameworks properly relaxed and characterized electronically we can investigate carbon dioxide adsorption properties. For the doped graphene and porphyrin-like several different sites were explored. Initial configurations with CO_2 perpendicular and parallel to the sheet were explored. In parallel configurations, we considered sites where the center of mass of the molecule was aligned with each atom related to the doping cluster and with both hollows, i.e., Zn, N, C1, C2, H1, and H2, following Figure 5.4c labels.

A distance of 3.0 Å to the sheet was considered for all initial configurations. Parallel configurations were started with CO_2 aligned over the [001] axis. Two exceptions were considered, a configuration where the CO_2 molecule is centered in the Zn atom but in the diagonal, with the oxygens aligned with the N atoms (this configuration will be referred to as Zn-N bridge), and another configuration where the oxygens were aligned with H1 and H2 (this configuration will be referred as H-aligned). Perpendicular initial configurations also considered a distance of 3.0 Å from the sheet. All sites for the relevant atoms in the cluster and the hollows were explored. Representations of the sites are illustrated in Appendix D and Appendix E.

Table 5.2 shows the calculated adsorption energies at several sites and orientations explored. We can note a significant increase compared to the adsorption energy of pristine ZIF-8. However, the energies are negative, indicating attraction, and still considerable for adsorption. The most significant difference here is that sites near Zn also favor adsorption. In pristine ZIF-8, the tetrahedral coordination makes Zn inaccessible with largely positive energies in sites near the metallic site. Final relaxed positions of the adsorption sites are reported in Appendix D and Appendix E.

Table 5.2: Adsorption energies of CO_2 at doped graphene and porphyrin-like.

Site	Doped Graphene E_{ads} (eV)	Porphyrin-like E_{ads} (eV)
H1 perp.	-0.124	-0.076
H1 parallel	-0.201	-0.129
H2 perp.	-0.132	-0.084
H2 parallel	-0.223	-0.150
H-aligned	-0.206	-0.152
C1 perp.	-0.210	-0.069
C1 parallel	-0.229	-0.162
C2 perp.	-0.119	-0.076
C2 parallel	-0.228	-0.160
Zn perp.	-0.137	-0.089
Zn parallel	-0.188	-0.114
Zn-N bridge	-0.175	-0.103
N	-0.237	-0.169
Reference: Imidazole ring (no defect): -0.352 eV		

Note that we only have one site reported for N. Both parallel and perpendicular initial conditions led to the same preferable site. It is important to remark that for the porphyrin-like framework the energies are even higher when compared with graphene doped, this happens because of the repulsion between the CO_2 molecule and its image replicated to reproduce PBC. Despite the energies being even higher, the sites for Zn are accessible. The energies are compatible with a physisorption process.

For the doped graphene framework, the charge difference for the preferable site with

the molecule aligned with nitrogen can be seen in Figure 5.7. Yellow isosurfaces represent positive differences, while green represents negative differences. The color code for the atoms of the structure follows the conventional color code adopted throughout this work: purple for Zn atoms, blue for N, and grey for C. Isosurfaces are plotted for 0.002 e/Bohr^3. Note that near Zn, we have a negative distribution (illustrated in green), while N and C have a positive distribution (illustrated in yellow). The interaction changes the density distribution of carbons up to the second neighbors.

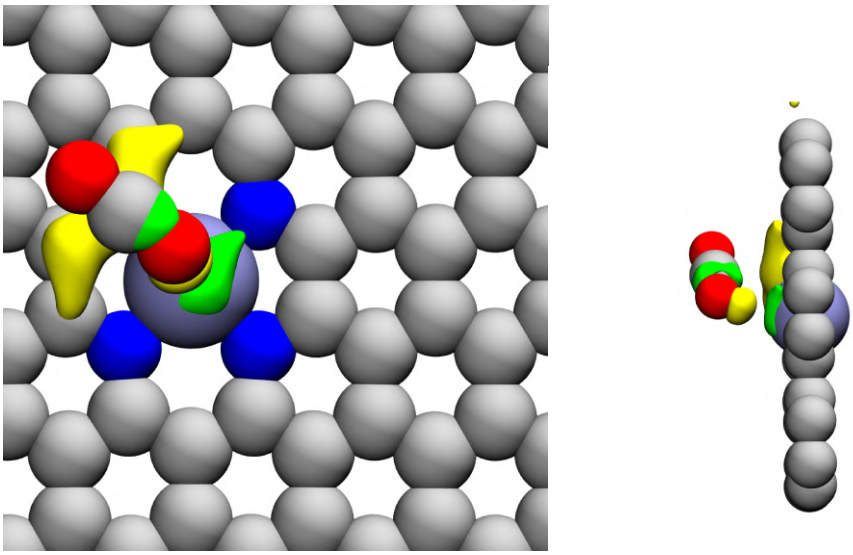

(a) (b)

Figure 5.7: Charge density difference for the adsorption of carbon dioxide in doped graphene preferable adsorption site, i.e., aligned with nitrogen. (a) Top view of the sheet. (b) Side view of the sheet. Color code: zinc in purple, nitrogen in blue, and carbon in gray. In yellow we have the positive isosurfaces, while in green the negative ones. Isosurfaces are plotted for a value of 0.002 e/Bohr^3

While for the porphyrin-like framework the charge difference can be seen in Figure 5.8. In yellow we have the positive isosurfaces, while in green the negative ones. Isosurfaces are plotted for a value of 0.003 e/Bohr^3. Note that once again, we see a negative density near Zn and a positive density near N and the first and second neighbors carbons. However, a negative distribution is also seen in C2 carbons away from the CO_2 molecule.

Considering those charge differences for the strongest interaction for each framework we can infer that the charge rearrangement is mostly local. Porphyrin-like frameworks, due to its size, have a slightly more global effect but still negligible when compared to the local redistribution of charge.

It is also interesting to point out that atoms from the frameworks were also able to move in the process of relaxation to find the preferable adsorption site. Even with this degree of freedom, atoms of the surface were not significantly pushed or pulled by guest molecules.

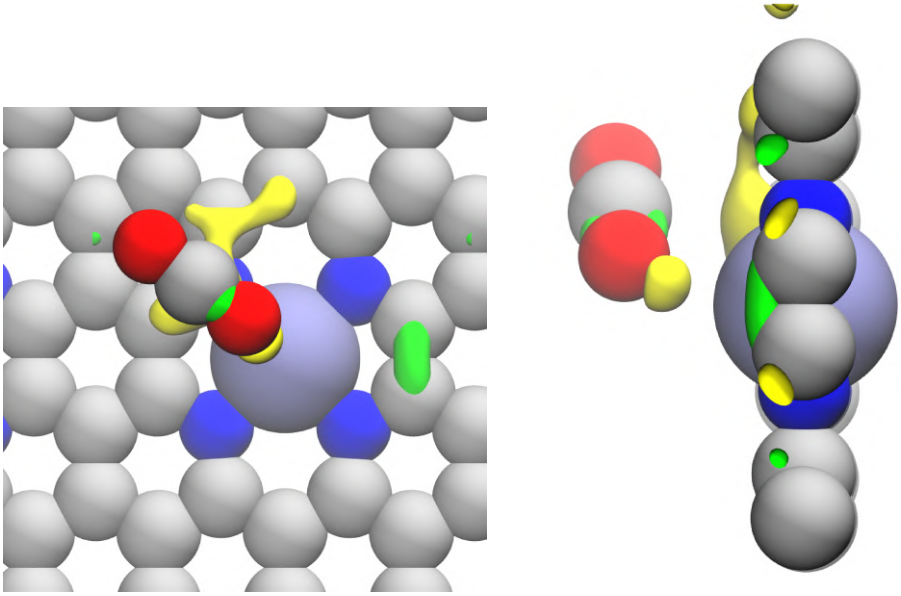

(a) (b)

Figure 5.8: Charge density difference for the adsorption of carbon dioxide in doped graphene preferable adsorption site, i.e., aligned with nitrogen. (a) Top view of the sheet. (b) Side view of the sheet. Color code: zinc in purple, nitrogen in blue, and carbon in gray. In yellow we have the positive isosurfaces, while in green the negative ones. Isosurfaces are plotted for a value of 0.003 e/Bohr^3

5.3.3 GCMC adsorption

Using DFT calculations we could investigate the interaction with one molecule of carbon dioxide and the frameworks explored, where we noted that adsorption energies were consistent with physisorption process. However, to understand more of the adsorption process in a larger scale we can use atomistic simulations as we did for pristine ZIF-8. With this methodology we can explore how many molecules the frameworks can adsorb, if the adsorption occurs in a single layer, and many more details of the dynamics of the system.

To understand if these possible new sites associated with Zn can increase the uptake of CO_2, we simulate the adsorption of CO_2 in a reservoir of 1 bar, at T = 303 K, using GCMC. In this way, we can compare the adsorption of the thermally treated structures from pristine ZIF-8. To use GCMC, we calculated the partial charge for each atomic species using DFT to compute for Coulombic interactions, while we used the FF for pristine ZIF-8 [26] to compute for Lennard-Jones interactions. It is important to remark that using this FF is an initial approximation of modelling the interaction of these new frameworks with carbon dioxide.

The protocol considered was first to calculate new partial charges for each framework. A replicated 5×5 structure was considered for both frameworks centered in the axis perpendicular to the surface. First we ran an equilibration of 1 $\times$ 10^6 steps using GCMC,

followed by a production phase of 5×10^6 steps where we insert CO_2 in a box with 50 Å of height. The position of the atoms from the molecule of CO_2 in the production phase will be averaged to build a density profile where we can identify layers of adsorption and finally count the number of molecules adsorbed. The partial charges obtained are reported in Table 5.3.

Table 5.3: Partial charges obtained with DFT for the models after thermal treatment at high temperatures.

Atom type	Doped graphene q (e)	Porphyrin-like q (e)
Zn	-1.1194	-1.1369
N	1.2733	1.2958
C1	-0.4430	-0.4386
C2	-0.5255	-0.5381
C3	-0.0022	-0.1295

Figure 5.9a illustrates one snapshot of the simulation. Constructing a density profile of the CO_2 molecules over the axis perpendicular to the surface, we can clearly identify the layers of adsorption, as Figure 5.9b suggests. Integrating over these layers of adsorption, we can obtain the number of molecules adsorbed in the two-dimensional structure considered.

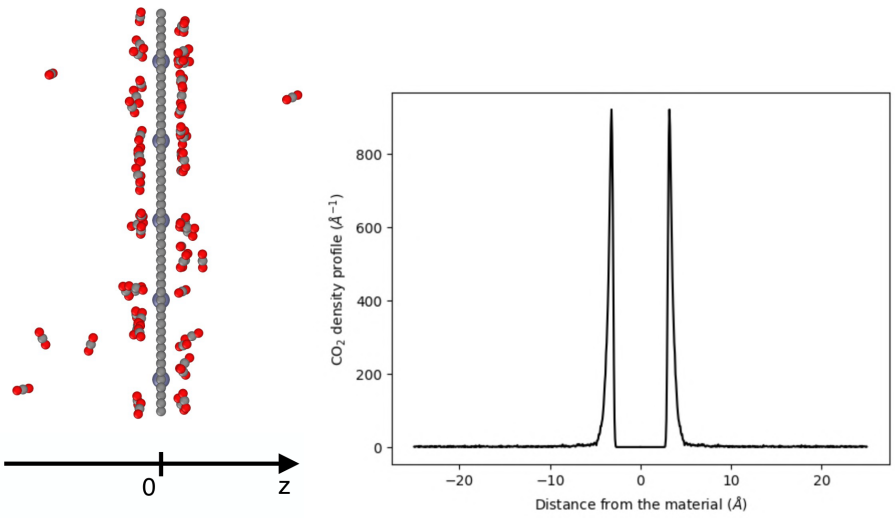

(a) (b)

Figure 5.9: (a) Snapshot of the GCMC simulation illustrating the z axis considered, the structure centered in z and the CO_2 atoms adsorbing. (b) Density profile of CO_2 along the z axis.

The total number of molecules adsorbed normalized by the number of Zn atoms in the system and by the weight of the material are reported in Table 5.4. Note that the two-dimensional structures adsorb approximately 15 to 18.5 times more CO_2 when we normalize by the number of Zn. Considering the normalization within the weight of the

material, the CO_2 uptake can reach an increase of approximately 136 times. However, the most appropriate normalization is considering the number of Zn atoms since the molecular composition of these thermal-induced structures is not equivalent to ZIF-8.

Table 5.4: Adsorbed CO_2 molecules in doped graphene and porphyrin-like structures in comparison with pristine ZIF-8 normalized by atoms of Zn and by weight.

	# molecules adsorbed/Zn	mols/kg
Doped graphene	2.2247	72.2305
Porphyrin-like	1.8040	58.5714
Pristine ZIF-8	0.1207	0.5306

This increase in CO_2 uptake indicates that thermally treated ZIF-8 might be a very promising material for capturing carbon with a very cheap and easy-to-scale-up production treatment. However, several properties of these thermally treated samples can impact adsorption, and our model does not take them into account. ZIF-8 can not be completely unrolled into two-dimensional sheets. Studies on the length of these sheets and how they are packed must be done. The cluster concentration of Zn and N must also be systematically explored.

Therefore, we conclude that thermal treatments are very promising regarding increasing the CO_2 uptake, reaching outstanding increases with this initial model that adapts ZIF-8 classical FF. It is also a very cheap and easy treatment to be done even at scaled up productions, making it even more promising. However, these initial approximations made in our first model still needs to be relaxed and a more detailed model must be designed to understand better the effects induced by these structural changes.

5.3.4 Conclusion

We have developed models to represent structures resulting from post-thermal treatments carried out at two temperature ranges. Treatments around 525 °C did not show significant changes in adsorption energy, indicating that methyl vacancies might not be the main cause of enhancing adsorption for this type of treatment. For treatments around 900 °C, where there is a transition to planar coordination between zinc and nitrogen, a combination of first-principles and atomistic calculations indicates a very promising enhancing in carbon capture. Our initial model indicates a possibility of increasing carbon uptake by 15 to 18.5 times compared to bulk ZIF-8.

Therefore, considering thermal treatments are cost-effective and have good scalability, treated ZIF-8 could effectively compete with amine absorption. ZIF-8, when subjected to these treatments, could serve as a suitable filler for incorporation into mixed-matrix membranes, enabling the design of an efficient and economically viable carbon capture membrane. Further research is required to better understand the formation of these

structures, including factors such as the spacing between layers in two-dimensional sheets and the concentration of ZnN clusters, which can significantly impact adsorption.

6 | Conclusions and Perspectives

In this work, we explore an alternative material to capture carbon from the post-combustion flue gas to tackle the urgent need to mitigate climate change. In particular, we explore the use of MOFs, specially ZIF-8, in membranes technology. We used first-principles calculations, using Density Functional Theory, together with atomistic simulations, using Monte Carlo and Molecular Dynamics to model pristine and thermally modified ZIF-8.

Initially, we report the results of simulations in pristine ZIF-8. Using first-principles calculations, we characterized ZIF-8 as a wide-gap semiconductor with a direct band gap of 3.964 eV. We explored CO_2 adsorption sites using nonlocal functionals for accounting for van der Waals interactions, a level of calculation improving the description available in the literature to study this framework. Besides obtaining a preferable adsorption site correlated with the organic linker, adsorption site calculations also led us to validate a classical force field regarding adsorption properties, with a proper description of the preferable site and adsorption energies.

Using this classical FF, we obtained adsorption isotherms for CO_2, CH_4, and N_2 using GCMC. From these simulations, we could infer from the local density of adsorbed atoms preferable sites in agreement with first-principles calculations. Moreover, a dual-sorption mode for CO_2 at higher pressures was observed, with carbon dioxide molecules nucleating at the center of the pores. Fitting the adsorption isotherms also lets us conclude that a dual-sorption mode is necessary to describe CO_2 adsorption properly. Considering binary mixtures, we validated the use of the IAST, comparing results using this theory with GCMC simulations. Additionally, from these binary mixtures, we calculate the selectivity regarding carbon capture, where bulk ZIF-8, despite presenting outstanding indicators, is still insufficient to be economically viable versus amine absorption.

At last, we model structures induced by post-thermal treatments at different temperature ranges. Experimental reports in the literature indicate these treatments as promising, considerably enhancing carbon uptake. Once again, combining first-principles and atomistic calculations, our model for structures treated near 900 °C, transitioning to planar coordination between Zn and N, indicates that carbon uptake might be increased 15 to 18.5 times the uptake in pristine ZIF-8.

Therefore, these thermally treated frameworks are promising to capture carbon and viably compete with amine absorption. It can designate ZIF-8 treated as a proper filler to

be used in mixed-matrix membranes, enabling a membrane design that can be efficient and economically viable to capture carbon. Despite this promising results, our initial models are approximations of the treated frameworks. More needs to be studied on the formation of these structures; the distance between layers of the two-dimensional sheets and the concentration of ZnN clusters can drastically affect adsorption.

With this work we have defined a protocol of simulations to characterize and validate interactions between gases and MOFs. One can continue this work exploring other greenhouse gases and other nanostructures to continue the extensive search to find proper and promising materials.

Suggested next steps are associated with understanding the interaction of N_2 with the ZIF-8 and the impacts of the thermal treatments in N_2 adsorption as well. Additionally, other ZnN cluster formations might be systematically studied. The adsorption of packed sheets can also be explored by understanding the impact of layers distance in CO_2/N_2 separation.

Bibliography

[1] IPCC. *Climate Change 2021: The Physical Science Basis. Contribution of Working Group I to the Sixth Assessment Report of the Intergovernmental Panel on Climate Change*, volume In Press. Cambridge University Press, Cambridge, United Kingdom and New York, NY, USA, 2021. DOI: 10.1017/9781009157896.

[2] IPCC. *Summary for policymakers.* In *Global Warming of 1.5°C. An IPCC Special Report on the impacts of global warming of 1.5°C above pre-industrial levels and related global greenhouse gas emission pathways, in the context of strengthening the global response to the threat of climate change, sustainable development, and efforts to eradicate poverty.* V. Masson-Delmotte, Z. P., H.-O. Portner, D. Roberts, J. Skea, P. Shukla, A. Pirani, W. Moufouma-Okia, C. Péan, R. Pidcock, S. Connors, J. Matthews, Y. Chen, X. Zhou, M. Gomis, E. Lonnoy, T. Maycock, M. Tignor, and T. Waterfield, editors. Cambridge University Press, Cambridge, United Kingdom and New York, NY, USA, 2018, 3-24. DOI: 10.1017/9781009157940.001.

[3] IPCC. *Summary for policymakers.* In *Climate Change 2021: The Physical Science Basis. Contribution of Working Group I to the Sixth Assessment Report of the Intergovernmental Panel on Climate Change.* V. Masson-Delmotte, P. Zhai, A. Pirani, S. Connors, C. Péan, S. Berger, N. Caud, Y. Chen, L. Goldfarb, M. Gomis, M. Huang, K. Leitzell, E. Lonnoy, J. Matthews, T. Maycock, T. Waterfield, O. Yelekçi, R. Yu, and B. Zhou, editors. Cambridge University Press, Cambridge, United Kingdom and New York, NY, USA, 2021, 3-32. DOI: 10.1017/9781009157896.001.

[4] J. Gibbins and H. Chalmers. Carbon capture and storage. *Energy Policy*, 36(12):4317–4322, 2008.

[5] P. Choudhary. Carbon Capture and Storage Program (CCSP): Final Report, Oct. 2016.

[6] J. Pires, F. Martins, M. Alvim-Ferraz, and M. Simões. Recent developments on carbon capture and storage: an overview. *Chemical engineering research and design*, 89(9):1446–1460, 2011.

[7] Q. Qian, P. A. Asinger, M. J. Lee, G. Han, K. Mizrahi Rodriguez, S. Lin, F. M. Benedetti, A. X. Wu, W. S. Chi, and Z. P. Smith. MOF-based membranes for gas separations. *Chemical reviews*, 120(16):8161–8266, 2020.

[8] V. M. A. Melgar, J. Kim, and M. R. Othman. Zeolitic imidazolate framework membranes for gas separation: a review of synthesis methods and gas separation performance. *Journal of Industrial and Engineering Chemistry*, 28:1–15, 2015.

[9] E. Adatoz, A. K. Avci, and S. Keskin. Opportunities and challenges of MOF-based membranes in gas separations. *Separation and Purification Technology*, 152:207–237, 2015.

[10] V. Vandeginste and K. Piessens. Pipeline design for a least-cost router application for CO_2 transport in the CO_2 sequestration cycle. *International Journal of Greenhouse Gas Control*, 2(4):571–581, 2008.

[11] B. Metz, O. Davidson, H. De Coninck, M. Loos, and L. Meyer. *IPCC special report on carbon dioxide capture and storage*. Cambridge: Cambridge University Press, 2005.

[12] R. W. Baker and K. Lokhandwala. Natural gas processing with membranes: an overview. *Industrial & Engineering Chemistry Research*, 47(7):2109–2121, 2008.

[13] M. Galizia, W. S. Chi, Z. P. Smith, T. C. Merkel, R. W. Baker, and B. D. Freeman. 50th anniversary perspective: polymers and mixed matrix membranes for gas and vapor separation: a review and prospective opportunities. *Macromolecules*, 50(20):7809–7843, 2017.

[14] S. E. M. Elhenawy, M. Khraisheh, F. AlMomani, and G. Walker. Metal-organic frameworks as a platform for CO_2 capture and chemical processes: adsorption, membrane separation, catalytic-conversion, and electrochemical reduction of CO_2. *Catalysts*, 10(11):1293, 2020.

[15] B. Chen, Z. Yang, Y. Zhu, and Y. Xia. Zeolitic imidazolate framework materials: recent progress in synthesis and applications. *Journal of Materials Chemistry A*, 2(40):16811–16831, 2014.

[16] D. Y. Heo, H. H. Do, S. H. Ahn, and S. Y. Kim. Metal-organic framework materials for perovskite solar cells. *Polymers*, 12(9):2061, 2020.

[17] M. Bergaoui, M. Khalfaoui, A. Awadallah-F, and S. Al-Muhtaseb. A review of the features and applications of zif-8 and its derivatives for separating CO_2 and isomers of C3-and C4-hydrocarbons. *Journal of Natural Gas Science and Engineering*, 96:104289, 2021.

[18] A. Deacon, L. Briquet, M. Malankowska, F. Massingberd-Mundy, S. Rudić, H. Cavaye, J. Coronas, S. Poulston, T. Johnson, et al. Understanding the ZIF-L to ZIF-8 transformation from fundamentals to fully costed kilogram-scale production. *Communications Chemistry*, 5(1):1–10, 2022.

[19] T. Yu, Q. Cai, G. Lian, Y. Bai, X. Zhang, X. Zhang, L. Liu, and S. Zhang. Mechanisms behind high CO_2/CH_4 selectivity using ZIF-8 metal organic frameworks with encapsulated ionic liquids: a computational study. *Chemical Engineering Journal*, 419:129638, 2021.

[20] S. He, L. Wu, X. Li, H. Sun, T. Xiong, J. Liu, C. Huang, H. Xu, H. Sun, W. Chen, et al. Metal-organic frameworks for advanced drug delivery. *Acta Pharmaceutica Sinica B*, 11(8):2362–2395, 2021.

[21] S. Rojas, A. Rodríguez-Diéguez, and P. Horcajada. Metal–organic frameworks in agriculture. *ACS Applied Materials & Interfaces*, 14(15):16983–17007, 2022.

[22] S. Dhaka, R. Kumar, A. Deep, M. B. Kurade, S.-W. Ji, and B.-H. Jeon. Metal–organic frameworks (MOFs) for the removal of emerging contaminants from aquatic environments. *Coordination Chemistry Reviews*, 380:330–352, 2019.

[23] H. P. Paudel, W. Shi, D. Hopkinson, J. A. Steckel, and Y. Duan. Computational modelling of adsorption and diffusion properties of co 2 and ch 4 in zif-8 for gas separation applications: a density functional theory approach. *Reaction Chemistry & Engineering*, 6(6):990–1001, 2021.

[24] J. Pérez-Pellitero, H. Amrouche, F. R. Siperstein, G. Pirngruber, C. Nieto-Draghi, G. Chaplais, A. Simon-Masseron, D. Bazer-Bachi, D. Peralta, and N. Bats. Adsorption of CO_2, CH_4, and N_2 on zeolitic imidazolate frameworks: experiments and simulations. *Chemistry–A European Journal*, 16(5):1560–1571, 2010.

[25] D. Liu, Y. Wu, Q. Xia, Z. Li, and H. Xi. Experimental and molecular simulation studies of CO_2 adsorption on zeolitic imidazolate frameworks: ZIF-8 and amine-modified ZIF-8. *Adsorption*, 19(1):25–37, 2013.

[26] X. Wu, J. Huang, W. Cai, and M. Jaroniec. Force field for ZIF-8 flexible frameworks: atomistic simulation of adsorption, diffusion of pure gases as CH_4, H_2, CO_2 and N_2. *RSC Advances*, 4(32):16503–16511, 2014.

[27] L. Hertäg, H. Bux, J. Caro, C. Chmelik, T. Remsungnen, M. Knauth, and S. Fritzsche. Diffusion of CH_4 and H_2 in ZIF-8. *Journal of Membrane Science*, 377(1-2):36–41, 2011.

[28] P. Krokidas, M. Castier, S. Moncho, E. Brothers, and I. G. Economou. Molecular simulation studies of the diffusion of methane, ethane, propane, and propylene in ZIF-8. *The Journal of Physical Chemistry C*, 119(48):27028–27037, 2015.

[29] R. J. Verploegh, A. Kulkarni, S. E. Boulfelfel, J. C. Haydak, D. Tang, and D. S. Sholl. Screening diffusion of small molecules in flexible zeolitic imidazolate frameworks using a dft-parameterized force field. *The Journal of Physical Chemistry C*, 123(14):9153–9167, 2019.

[30] T. Weng and J. Schmidt. Flexible and transferable ab initio force field for zeolitic imidazolate frameworks: ZIF-FF. *The Journal of Physical Chemistry A*, 123(13):3000–3012, 2019.

[31] T. Chen and T. A. Manz. A collection of forcefield precursors for metal–organic frameworks. *RSC advances*, 9(63):36492–36507, 2019.

[32] A. H. Mashhadzadeh, A. Taghizadeh, M. Taghizadeh, M. T. Munir, S. Habibzadeh, A. Salmankhani, F. J. Stadler, and M. R. Saeb. Metal–Organic Framework (MOF) through the lens of molecular dynamics simulation: current status and future perspective. *Journal of Composites Science*, 4(2):75, 2020.

[33] S. Gadipelli, W. Travis, W. Zhou, and Z. Guo. A thermally derived and optimized structure from ZIF-8 with giant enhancement in CO_2 uptake. *Energy & Environmental Science*, 7(7):2232–2238, 2014.

[34] Q. Wang, T. Ina, W.-T. Chen, L. Shang, F. Sun, S. Wei, D. Sun-Waterhouse, S. G. Telfer, T. Zhang, and G. I. Waterhouse. Evolution of zn (ii) single atom catalyst sites during the pyrolysis-induced transformation of zif-8 to n-doped carbons. *Science Bulletin*, 65(20):1743–1751, 2020.

[35] K. Capelle. A bird's-eye view of density-functional theory. *Brazilian journal of physics*, 36:1318–1343, 2006.

[36] R. M. Dreizler and E. K. Gross. *Density functional theory: an approach to the quantum many-body problem*. Springer Science & Business Media, 2012.

[37] R. G. Parr and Y. Weitao. *Density functional theory of atoms and molecules*. Oxford University Press, 1994.

[38] M. Born and J. Oppenheimer. Zur Quantentheorie der Molekeln. *Annalen der Physik*, 389(20):457–484, 1927.

[39] J. C. Slater. A simplification of the hartree-fock method. *Physical review*, 81(3):385, 1951.

[40] R. J. Bartlett and D. M. Silver. Some aspects of diagrammatic perturbation theory. *International Journal of Quantum Chemistry*, 9(S9):183–198, 1975.

[41] I. Shavitt. The method of configuration interaction. In *Methods of electronic structure theory*, pages 189–275. Springer, 1977.

[42] W. Kohn and L. J. Sham. Self-consistent equations including exchange and correlation effects. *Physical review*, 140(4A):A1133, 1965.

[43] P. Hohenberg and W. Kohn. Inhomogeneous electron gas. *Physical review*, 136(3B):B864, 1964.

[44] P. A. Dirac. Note on exchange phenomena in the thomas atom. In *Mathematical proceedings of the Cambridge philosophical society*, volume 26 of number 3, pages 376–385. Cambridge University Press, 1930.

[45] R. G. Parr. Density functional theory of atoms and molecules. In *Horizons of Quantum Chemistry: Proceedings of the Third International Congress of Quantum Chemistry Held at Kyoto, Japan, October 29-November 3, 1979*, pages 5–15. Springer, 1980.

[46] D. M. Ceperley and B. J. Alder. Ground state of the electron gas by a stochastic method. *Physical review letters*, 45(7):566, 1980.

[47] J. P. Perdew, K. Burke, and M. Ernzerhof. Generalized gradient approximation made simple. *Physical review letters*, 77(18):3865, 1996.

[48] A. Becke. Density-functional thermochemistry. III. The role of exact exchange. *Chem. Phys*, 98:5648, 1993.

[49] C. Lee, W. Yang, and R. G. Parr. Development of the Colle-Salvetti correlation-energy formula into a functional of the electron density. *Physical review B*, 37(2):785, 1988.

[50] S. H. Vosko, L. Wilk, and M. Nusair. Accurate spin-dependent electron liquid correlation energies for local spin density calculations: a critical analysis. *Canadian Journal of physics*, 58(8):1200–1211, 1980.

[51] P. J. Stephens, F. J. Devlin, C. F. Chabalowski, and M. J. Frisch. Ab initio calculation of vibrational absorption and circular dichroism spectra using density functional force fields. *The Journal of physical chemistry*, 98(45):11623–11627, 1994.

[52] C. Adamo and V. Barone. Toward reliable density functional methods without adjustable parameters: the PBE0 model. *The Journal of chemical physics*, 110(13):6158–6170, 1999.

[53] S. Grimme. Density functional theory with London dispersion corrections. *Wiley Interdisciplinary Reviews: Computational Molecular Science*, 1(2):211–228, 2011.

[54] S. Grimme, A. Hansen, J. G. Brandenburg, and C. Bannwarth. Dispersion-corrected mean-field electronic structure methods. *Chemical reviews*, 116(9):5105–5154, 2016.

[55] S. Grimme. Semiempirical GGA-type density functional constructed with a long-range dispersion correction. *Journal of computational chemistry*, 27(15):1787–1799, 2006.

[56] S. Grimme, J. Antony, S. Ehrlich, and H. Krieg. A consistent and accurate ab initio parametrization of density functional dispersion correction (dft-d) for the 94 elements h-pu. *The Journal of chemical physics*, 132(15):154104, 2010.

[57] D. G. Smith, L. A. Burns, K. Patkowski, and C. D. Sherrill. Revised damping parameters for the d3 dispersion correction to density functional theory. *The journal of physical chemistry letters*, 7(12):2197–2203, 2016.

[58] M. Dion, H. Rydberg, E. Schröder, D. C. Langreth, and B. I. Lundqvist. Van der Waals density functional for general geometries. *Physical review letters*, 92(24):246401, 2004.

[59] J. Klimeš, D. R. Bowler, and A. Michaelides. Van der Waals density functionals applied to solids. *Physical Review B*, 83(19):195131, 2011.

[60] I. Hamada. Van der Waals density functional made accurate. *Physical Review B*, 89(12):121103, 2014.

[61] J. Klimeš and A. Michaelides. Perspective: Advances and challenges in treating van der Waals dispersion forces in density functional theory. *The Journal of chemical physics*, 137(12), 2012.

[62] P. Schwerdtfeger. The pseudopotential approximation in electronic structure theory. *ChemPhysChem*, 12(17):3143–3155, 2011.

[63] D. Hamann, M. Schlüter, and C. Chiang. Norm-conserving pseudopotentials. *Physical Review Letters*, 43(20):1494, 1979.

[64] D. Vanderbilt. Soft self-consistent pseudopotentials in a generalized eigenvalue formalism. *Physical review B*, 41(11):7892, 1990.

[65] P. E. Blöchl. Projector augmented-wave method. *Physical review B*, 50(24):17953, 1994.

[66] O. K. Andersen. Linear methods in band theory. *Physical Review B*, 12(8):3060, 1975.

[67] G. Kresse and J. Furthmüller. Efficient iterative schemes for ab initio total-energy calculations using a plane-wave basis set. *Physical review B*, 54(16):11169, 1996.

[68] G. Kresse and D. Joubert. From ultrasoft pseudopotentials to the projector augmented-wave method. *Physical review b*, 59(3):1758, 1999.

[69] D. Frenkel and B. Smit. *Understanding molecular simulation: from algorithms to applications*, volume 1. Elsevier, 2001.

[70] M. P. Allen and D. J. Tildesley. *Computer simulation of liquids*. Oxford university press, 2017.

[71] W. L. Jorgensen and J. Tirado-Rives. Potential energy functions for atomic-level simulations of water and organic and biomolecular systems. *Proceedings of the National Academy of Sciences*, 102(19):6665–6670, 2005.

[72] H. A. Lorentz. Ueber die anwendung des satzes vom virial in der kinetischen theorie der gase. *Annalen der physik*, 248(1):127–136, 1881.

[73] D. Berthelot. Sur le mélange des gaz. *Comptes Rendus Hebdomadaires des Séances*, 126:1703–1855, 1898.

[74] J. G. Harris and K. H. Yung. Carbon dioxide's liquid-vapor coexistence curve and critical properties as predicted by a simple molecular model. *The Journal of Physical Chemistry*, 99(31):12021–12024, 1995.

[75] M. G. Martin and J. I. Siepmann. Transferable potentials for phase equilibria. 1. United-atom description of n-alkanes. *The Journal of Physical Chemistry B*, 102(14):2569–2577, 1998.

[76] J. J. Potoff and J. I. Siepmann. Vapor–liquid equilibria of mixtures containing alkanes, carbon dioxide, and nitrogen. *AIChE journal*, 47(7):1676–1682, 2001.

[77] L. Zhang, Z. Hu, and J. Jiang. Sorption-induced structural transition of zeolitic imidazolate framework-8: a hybrid molecular simulation study. *Journal of the American Chemical Society*, 135(9):3722–3728, 2013.

[78] T. Chokbunpiam, S. Fritzsche, C. Chmelik, J. Caro, W. Janke, and S. Hannongbua. Gate opening, diffusion, and adsorption of CO_2 and N_2 mixtures in ZIF-8. *The Journal of Physical Chemistry C*, 120(41):23458–23468, 2016.

[79] Y. Duan, C. Wu, S. Chowdhury, M. C. Lee, G. Xiong, W. Zhang, R. Yang, P. Cieplak, R. Luo, T. Lee, et al. A point-charge force field for molecular mechanics simulations of proteins based on condensed-phase quantum mechanical calculations. *Journal of computational chemistry*, 24(16):1999–2012, 2003.

[80] A. K. Rappé, C. J. Casewit, K. Colwell, W. A. Goddard III, and W. M. Skiff. UFF, a full periodic table force field for molecular mechanics and molecular dynamics simulations. *Journal of the American chemical society*, 114(25):10024–10035, 1992.

[81] T. A. Manz and D. S. Sholl. Chemically meaningful atomic charges that reproduce the electrostatic potential in periodic and nonperiodic materials. *Journal of Chemical Theory and Computation*, 6(8):2455–2468, 2010.

[82] P. P. Ewald. Die berechnung optischer und elektrostatischer gitterpotentiale. *Annalen der physik*, 369(3):253–287, 1921.

[83] E. Madelung. Das elektrische feld in systemen von regelmäßig angeordneten punktladungen. *Phys. Z*, 19(524):32, 1918.

[84] J. W. Eastwood, R. W. Hockney, and D. Lawrence. P3m3dp—the three-dimensional periodic particle-particle/particle-mesh program. *Computer Physics Communications*, 19(2):215–261, 1980.

[85] S. Ulam, R. Richtmyer, and J. Von Neumann. Statistical methods in neutron diffusion. *LAMS-551, Los Alamos National Laboratory*:1–22, 1947.

[86] N. Metropolis and S. Ulam. The monte carlo method. *Journal of the American statistical association*, 44(247):335–341, 1949.

[87] N. Metropolis, A. W. Rosenbluth, M. N. Rosenbluth, A. H. Teller, and E. Teller. Equation of state calculations by fast computing machines. *The journal of chemical physics*, 21(6):1087–1092, 1953.

[88] M. Kardar. *Statistical physics of particles*. Cambridge University Press, 2007.

[89] J. K. Shah, E. Marin-Rimoldi, R. G. Mullen, B. P. Keene, S. Khan, A. S. Paluch, N. Rai, L. L. Romanielo, T. W. Rosch, B. Yoo, et al. Cassandra: an open source monte carlo package for molecular simulation, 2017.

[90] J. K. Shah and E. J. Maginn. A general and efficient Monte Carlo method for sampling intramolecular degrees of freedom of branched and cyclic molecules. *The Journal of chemical physics*, 135(13):134121, 2011.

[91] J. I. Siepmann and D. Frenkel. Configurational bias monte carlo: a new sampling scheme for flexible chains. *Molecular Physics*, 75(1):59–70, 1992.

[92] W. C. Swope, H. C. Andersen, P. H. Berens, and K. R. Wilson. A computer simulation method for the calculation of equilibrium constants for the formation of physical clusters of molecules: Application to small water clusters. *The Journal of chemical physics*, 76(1):637–649, 1982.

[93] W. G. Hoover. Canonical dynamics: equilibrium phase-space distributions. *Physical review A*, 31(3):1695, 1985.

[94] A. P. Thompson, H. M. Aktulga, R. Berger, D. S. Bolintineanu, W. M. Brown, P. S. Crozier, P. J. in 't Veld, A. Kohlmeyer, S. G. Moore, T. D. Nguyen, R. Shan, M. J. Stevens, J. Tranchida, C. Trott, and S. J. Plimpton. LAMMPS - a flexible simulation tool for particle-based materials modeling at the atomic, meso, and continuum scales. *Comp. Phys. Comm.*, 271:108171, 2022.

[95] S. B. Novaković, G. A. Bogdanović, C. Heering, G. Makhloufi, D. Francuski, and C. Janiak. Charge-density distribution and electrostatic flexibility of zif-8 based on high-resolution x-ray diffraction data and periodic calculations. *Inorganic Chemistry*, 54(6):2660–2670, 2015.

[96] F. Birch. Finite elastic strain of cubic crystals. *Physical review*, 71(11):809, 1947.

[97] F. D. Murnaghan. The compressibility of media under extreme pressures. *Proceedings of the National Academy of Sciences*, 30(9):244–247, 1944.

[98] P. Vinet, J. R. Smith, J. Ferrante, and J. H. Rose. Temperature effects on the universal equation of state of solids. *Physical Review B*, 35(4):1945, 1987.

[99] D. E. Vanpoucke, K. Lejaeghere, V. Van Speybroeck, M. Waroquier, and A. Ghysels. Mechanical properties from periodic plane wave quantum mechanical codes: the challenge of the flexible nanoporous mil-47 (v) framework. *The Journal of Physical Chemistry C*, 119(41):23752–23766, 2015.

[100] Z. Li, M. Nevitt, and S. Ghose. Elastic constants of sodalite $Na_4Al_3Si_3O_12Cl$. *Applied Physics Letters*, 55(17):1730–1731, 1989.

[101] J. J. Williams, K. E. Evans, and R. I. Walton. On the elastic constants of the zeolite chlorosodalite. *Applied physics letters*, 88(2):021914, 2006.

[102] K. Fabrizio, K. N. Le, A. B. Andreeva, C. H. Hendon, and C. K. Brozek. Determining optical band gaps of MOFs. *ACS Materials Letters*, 4(3):457–463, 2022.

[103] R. Boulmene, K. Boussouf, M. Prakash, N. Komiha, M. M. Al-Mogren, and M. Hochlaf. Ab initio and dft studies on CO_2 interacting with Zn(q+)-Imidazole (q = 0, 1, 2) complexes: prediction of charge transfer through σ- or π- type models. *ChemPhysChem*, 17(7):994–1005, 2016.

[104] K. D. Vogiatzis, A. Mavrandonakis, W. Klopper, and G. E. Froudakis. Ab initio study of the interactions between CO_2 and N-containing organic heterocycles. *ChemPhysChem*, 10(2):374, 2009.

[105] B. Widom. Random sequential addition of hard spheres to a volume. *The Journal of Chemical Physics*, 44(10):3888–3894, 1966.

[106] L. Herrera, D. Do, and D. Nicholson. A monte carlo integration method to determine accessible volume, accessible surface area and its fractal dimension. *Journal of colloid and interface science*, 348(2):529–536, 2010.

[107] J. Qiu, X. Xu, B. Liu, Y. Guo, H. Wang, L. Yu, Y. Jiang, C. Huang, B. Fan, Z. Zeng, et al. Size-controllable synthesis of ZIF-8 and derived nitrogen-rich porous carbon for co2 and vocs adsorption. *Chemistryselect*, 7(36):e202203273, 2022.

[108] I. Langmuir. Vapor pressures, evaporation, condensation and adsorption. *Journal of the American Chemical Society*, 54(7):2798–2832, 1932.

[109] A. L. Myers and J. M. Prausnitz. Thermodynamics of mixed-gas adsorption. *AIChE journal*, 11(1):121–127, 1965.

[110] C. M. Simon, B. Smit, and M. Haranczyk. PyIAST: Ideal adsorbed solution theory (IAST) Python package. *Computer Physics Communications*, 200:364–380, 2016.

[111] A. Einstein. Uber die von der molekularkinetischen theorie der warme geforderte bewegung von in ruhenden flussigkeiten suspendierten teilchen (english translation: on the movement of small particles suspended in a stationary liquid demanded by the molecular-kinetic theory of heat). *Investigations on the Theory of the Brownian Movement, Dover, New York*, 1905.

[112] E. Pantatosaki, G. Megariotis, A.-K. Pusch, C. Chmelik, F. Stallmach, and G. K. Papadopoulos. On the impact of sorbent mobility on the sorbed phase equilibria and dynamics: a study of methane and carbon dioxide within the zeolite imidazolate framework-8. *The Journal of Physical Chemistry C*, 116(1):201–207, 2012.

[113] A.-K. Pusch, T. Splith, L. Moschkowitz, S. Karmakar, R. Biniwale, M. Sant, G. B. Suffritti, P. Demontis, J. Cravillon, E. Pantatosaki, et al. Nmr studies of carbon dioxide and methane self-diffusion in ZIF-8 at elevated gas pressures. *Adsorption*, 18(5):359–366, 2012.

[114] C. Chmelik. Characteristic features of molecular transport in MOF ZIF-8 as revealed by IR microimaging. *Microporous and Mesoporous Materials*, 216:138–145, 2015.

[115] W. Tang, E. Sanville, and G. Henkelman. A grid-based Bader analysis algorithm without lattice bias. *Journal of Physics: Condensed Matter*, 21(8):084204, 2009.

[116] S. Brandani, E. Mangano, and L. Sarkisov. Net, excess and absolute adsorption and adsorption of helium. *Adsorption*, 22(2):261–276, 2016.

[117] A. L. Myers and P. A. Monson. Physical adsorption of gases: the case for absolute adsorption as the basis for thermodynamic analysis. *Adsorption*, 20(4):591–622, 2014.

[118] H. Freundlich. *Kapillarchemie*. Akademische Verlagsgesellschaft mb H., 1922.

Appendices

A | Force Field Parameters

Gases

Three different gases were modeled, CO_2, CH_4, and N_2. Carbon dioxide molecules were modeled using the rigid EPM2 model [74], methane molecules were modeled with the TraPPE united-atom model [75], and nitrogen gas was modeled using the TraPPE three-site rigid model (two sites for the N atoms and one site at the center of mass labeled "M") to include quadrupole moment and charges [76]. Together with bond length information, all LJ parameters and Coulombic partial charges are given in Table A.1.

Table A.1: All the LJ parameters (ε, σ), Coulombic partial charges (q), and bond lengths used to model the greenhouse gases explored in this work (CO_2, CH_4, and N_2).

Molecule	Atom type	ε (K)	σ (Å)	q (e)
CO_2	C	28.129	2.757	0.6512
	O	80.507	3.033	-0.3256
	$d_{\text{C-O}}$ (Å) = 1.149			
CH4	CH4	148.000	3.730	0.0000
N_2	N	36.433	3.320	-0.4820
	M	0.000	0.000	0.9640
	$d_{\text{N-M}}$ (Å) = 0.550			

ZIF-8

We used the Force Field as proposed by Wu et al. [26]. The LJ parameters and Coulombic partial charges used to model ZIF-8 are given in Table A.2 following the label as illustrated in Figure A.1.

Table A.2: Parameters of the Wu et al. FF used to model ZIF-8 [26].

Bond type	K_b (kcal mol^{-1} Å^{-2})		b_0 (Å)
C1-C3	317.000		1.492
C3-N	488.000		1.339
C2-N	410.000		1.371
C2-H1	367.000		0.929
C2-C2	518.000		1.346
C1-H2	340.000		0.959
Zn-N	86.000		1.987
Angle type	**K_b (kcal mol^{-1} rad^{-2})**		**θ_0 (°)**
N-C3-N	70.000		112.17
N-C3-C1	70.000		123.89
C2-C2-N	70.000		108.67
C2-C2-H1	50.000		125.67
N-C2-H1	50.000		125.66
C3-C1-H2	50.000		109.44
C3-N-C2	70.000		105.24
C3-N-Zn	50.000		127.50
C2-N-Zn	35.000		128.00
N-Zn-N	10.500		109.47
H2-C1-H2	35.000		109.50
Dihedral type	**K_b (kcal mol^{-1})**	**n**	**ϕ_0 (°)**
C2-N-C3-N	4.800	2	180.0
C2-N-C3-C1	4.150	2	180.0
C3-N-C2-C2	4.800	2	180.0
C3-N-C2-H1	4.800	2	180.0
N-C2-C2-N	4.000	2	180.0
N-C2-C2-H1	4.000	2	180.0
H1-C2-C2-H1	4.000	2	180.0
Zn-N-C3-N	0.100	2	180.0
Zn-N-C3-C1	0.100	2	180.0
Zn-N-C2-C2	0.100	2	180.0
N-Zn-N-C3	0.174	3	0.0
N-Zn-N-C2	0.174	3	0.0
Improper type	**K_b (kcal mol^{-1} rad^{-2})**	**n**	**ψ_0 (°)**
N-C1-C3-N	1.100	2	180.0
C2-H1-C2-N	1.100	2	180.0
Atom type	**ε (K)**	**σ (Å)**	**q (e)**
Zn	39.630	2.462	0.6918
N	22.056	3.261	-0.3879
C1	33.587	3.431	-0.4526
C2	33.587	3.431	-0.0839
C3	33.587	3.431	0.4291
H1	14.049	2.571	0.1128
H2	14.049	2.571	0.1321

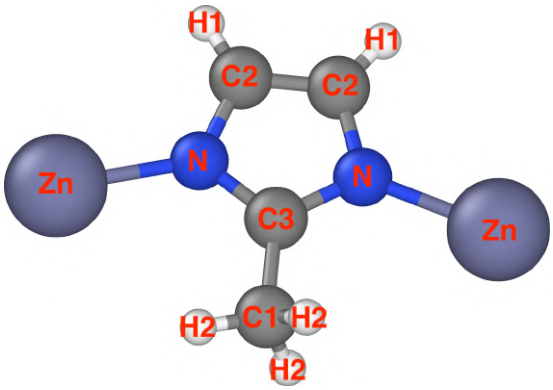

Figure A.1

Figure A.2: Labels considered for the ZIF-8 atoms throughout this work.

B | Shifted Chemical Potential and Partial Pressures for Mixtures

Here we present the calculated shifted chemical potentials and partial pressures for each species in each mixture explored in this work.

CO_2 and CH_4 mixtures

Table B.1: Shifted chemical potential (μ) and density at bulk phase (ρ) calculated for each species at different pressures (P). Monte Carlo at the NPT ensemble was used with the Widom insertion method for a reservoir containing a binary mixture of CO_2/CH_4 at an equimolar concentration.

P (bar)	μ_{CO_2} (kJ/mol)	ρ_{CO_2} (kg/m^3)	μ_{CH_4} (kJ/mol)	ρ_{CH_4} (kg/m^3)
0.1	-48.6	0.1	-44.8	0.03
0.5	-44.6	0.4	-40.8	0.2
1.0	-42.8	0.9	-39.0	0.3
5.0	-38.8	4.4	-35.0	1.6
10.0	-37.1	9.0	-33.2	3.3
20.0	-35.5	18.4	-31.5	6.7
50.0	-33.5	50.9	-29.3	18.5

Table B.2: Shifted chemical potential (μ) and density at bulk phase (ρ) calculated for each species at different molar concentrations of CH_4 (n_{CH_4}) with Monte Carlo at the NPT ensemble using the Widom insertion method for a reservoir containing a binary mixture of CO_2/CH_4 at a fixed pressure of 20 bar.

n_{H_4}	μ_{CO_2} (kJ/mol)	ρ_{CO_2} (kg/m^3)	μ_{CH_4} (kJ/mol)	ρ_{CH_4} (kg/m^3)
0.05	-33.9	36.2	-37.2	0.7
0.20	-34.3	30.2	-33.8	2.8
0.35	-34.8	24.2	-32.4	4.8
0.50	-35.5	18.5	-31.5	6.7
0.65	-36.3	12.8	-30.9	8.7
0.80	-37.8	7.3	-30.3	10.6
0.95	-41.2	1.8	-29.9	12.5

CO_2 and N_2 mixtures

Table B.3: Shifted chemical potential (μ) and density at bulk phase (ρ) calculated for each species at different pressures (P) with Monte Carlo at the NPT ensemble using the Widom insertion method for a reservoir containing a binary mixture of CO_2/N_2 at an equimolar concentration.

P (bar)	μ_{CO_2} (kJ/mol)	ρ_{CO_2} (kg/m^3)	μ_{N_2} (kJ/mol)	ρ_{N_2} (kg/m^3)
0.1	-48.6	0.1	-46.9	0.06
0.5	-44.6	0.4	-42.9	0.3
1.0	-42.8	0.9	-41.1	0.6
5.0	-38.8	4.4	-37.0	2.8
10.0	-37.1	8.9	-35.3	5.7
20.0	-35.5	18.1	-33.6	11.5
50.0	-33.5	47.7	-31.2	30.4

Table B.4: Shifted chemical potential (μ) and density at bulk phase (ρ) calculated for each species at different molar concentrations of CH_4 (n_{CH_4}) with Monte Carlo at the NPT ensemble using the Widom insertion method for a reservoir containing a binary mixture of CO_2/N_2 at a fixed pressure of 20 bar.

n_{CH_4}	μ_{CO_2} (kJ/mol)	ρ_{CO_2} (kg/m^3)	μ_{N_2} (kJ/mol)	ρ_{N_2} (kg/m^3)
0.05	-33.9	36.1	-39.2	1.2
0.20	-34.3	29.8	-35.8	4.8
0.35	-34.8	23.8	-34.4	8.2
0.50	-35.5	18.1	-33.6	11.5
0.65	-36.4	12.5	-32.9	14.8
0.80	-37.7	7.1	-32.4	18.0
0.95	-41.1	1.8	-32.0	21.2

C | Ideal Adsorbed Solution Theory

The Ideal Adsorbed Solution Theory (IAST) is a model used to predict mixture isotherms from unique species isotherms. It was developed by Myers and Prausnitz in 1965 [109]. It starts by assuming three hypotheses:

- Thermodynamic properties changes of the adsorbent are negligible in the adsorption process.
- All adsorbed species have the same surface area available.
- Gibbs definition of adsorption applies.

The third hypothesis is related to how adsorption isotherms measurements are quantified. There is a consensus that absolute adsorption must be used in IAST calculations instead of excess adsorption [116, 117]. It is also assumed that we have a function describing the unique species' isotherms. Usually, a model already established in the literature is used to fit data, like the Langmuir model [108]. It is also relevant to state that empirical models, like the Freundlich one [118], due to the non-linear behavior for low pressures, are not thermodynamically consistent. Therefore, the use of empirical models is not recommended in IAST.

At constant temperature, the first law of thermodynamics in differential form for the Gibbs free energy gives us:

$$-Ad\pi + \sum_i n_i d\mu_i = 0 \tag{C.1}$$

where volume and pressure are replaced by the area of the surface (A) and spreading pressure (π). The quantity adsorbed is given by n_i. Considering that component i acts as an ideal gas in the gas phase, the chemical potential is related to the partial pressure as:

$$d\mu_i = RTd\ln P_i \tag{C.2}$$

Assuming that the chemical potential must be the same in both phases at equilibrium, we should have the same relation for the adsorbed phase.

The Gibbs isotherm expression for a unique species is given by:

$$-Ad\pi_i + n_i^0 d\mu_i = 0 \tag{C.3}$$

where n_i^0 stands for the quantity adsorbed for the unique species. Using the expression for $d\mu_i$ given in Equation C.2 and integrating we get:

$$\frac{\pi_i A}{RT} = \int_0^{P_i^0} \frac{n_i^0}{P_i} dP_i \tag{C.4}$$

Thus, with the adsorption isotherm from unique species $n_i^0(P_i)$ modeled, one can solve the integral and calculate the spreading pressure.

Considering an ideal adsorbed solution, Raoult's law analogy gives us a relation between partial pressure and composition:

$$P_i = x_i P_i^0(\pi_i) \tag{C.5}$$

where P_i is the partial pressure in the gas phase of component i in the mixture, x_i the molar fraction of component i in the adsorbed phase, and $P_i^0(\pi_i)$ is the partial pressure of component i in the gas phase required to yield a spreading pressure π_i of pure species i in the adsorbed phase.

By the definition of P_i^0, the spreading pressure of the mixture π must be equal to the spreading pressures π_i of the pure components at pressure P_i^0. This means, for all components:

$$\pi = \pi_i(P_i^0) \tag{C.6}$$

For N components, Equation C.6 would give us $N-1$ equations, while Equation C.5 give us more N equations. P_i and the spreading pressures π_i as a function of P_i^0 are known, so our variables are x_i and P_i^0, resulting $2N$ variables. This means that with the additional constraint that $\sum_i x_i = 1$, we will have $2N$ equations and will be able to solve this non-linear system of equations.

Back to the Gibbs adsorption equation for the mixture (Equation C.1), it can be written:

$$A = \sum_i n_i \frac{\partial \mu_i}{\partial \pi} \tag{C.7}$$

to simplify this derivative, one can use the Gibbs expression for a pure component, assuming that in an ideal adsorbed solution, the chemical potentials would obey the same relation, resulting:

$$A = \sum_i n_i \frac{A}{n_i^0(P_i^0)} \tag{C.8}$$

dividing by n_T, the total moles of gas adsorbed, results:

$$\frac{1}{n_T} = \sum_i \frac{x_i}{n_i^0(P_i^0)} \tag{C.9}$$

Therefore, as x_i and P_i^0 are known to solve the system described above, and as n_i^0 is modeled as a function of pressure, one can calculate n_T. Then, the isotherms for the species in the mixtures can be constructed by calculating the quantity adsorbed of the component i in the mixture, given by:

$$n_i = x_i n_T \tag{C.10}$$

Since experimental data on the adsorption of mixtures are very hard to collect, our mixture's adsorption isotherms obtained from binary GCMC were compared with the ones estimated by IAST. In that way, a validation of this theory for MOFs, in particular, for ZIF-8, can be made.

D | Adsorption Sites: Doped Graphene

Illustrations of the adsorption sites of CO_2 in the doped graphene structure are reported. For each site we present top and side views of the two-dimensional sheet side by side. The order will follow adsorption energy as reported in Table 5.2.

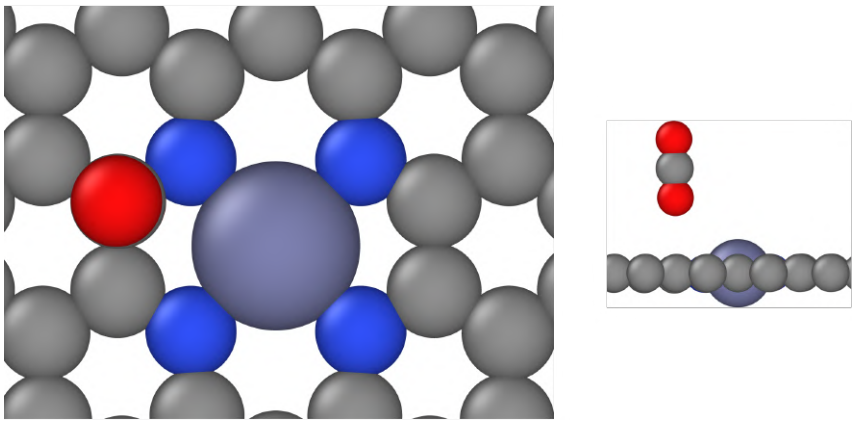

Figure D.1: C2 perp. $E_{ads} = -0.119$ eV

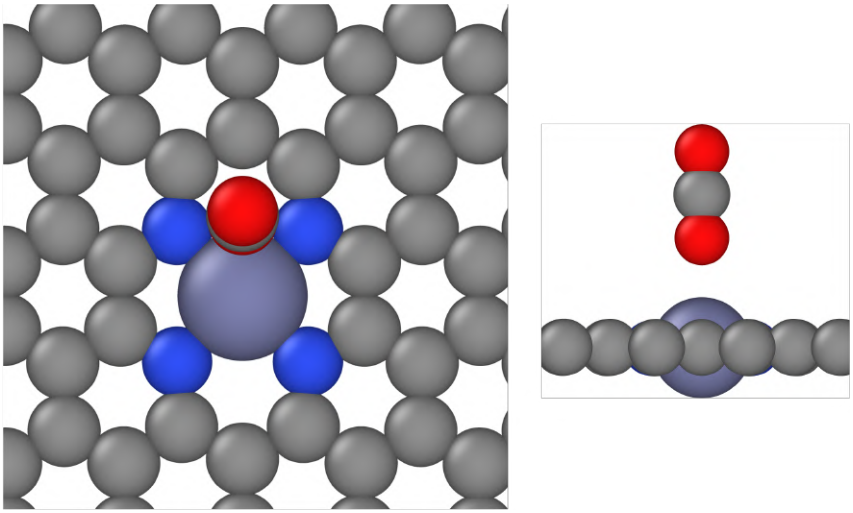

Figure D.2: H1 perp. $E_{ads} = -0.124$ eV

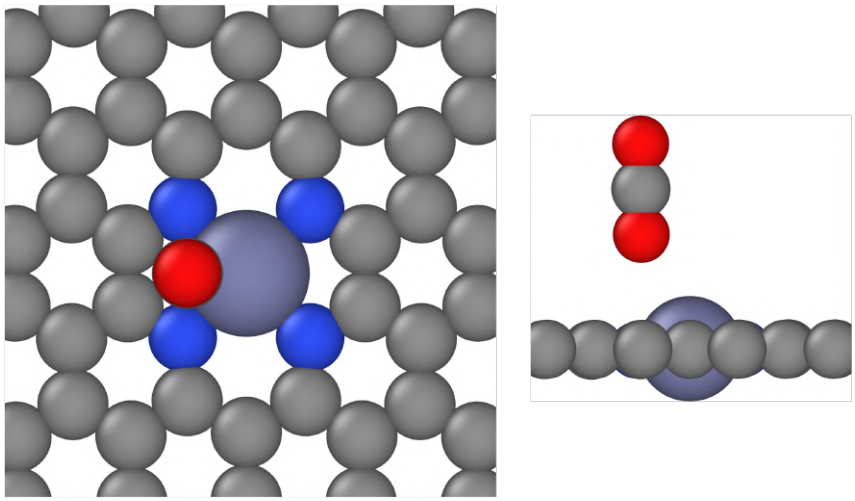

Figure D.3: H2 perp. $E_{ads} = -0.132$ eV

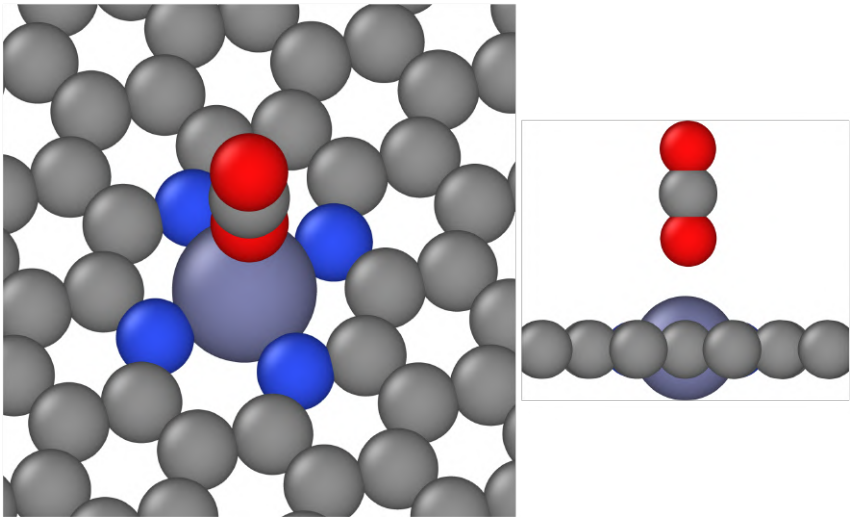

Figure D.4: Zn perp. $E_{ads} = -0.137$ eV

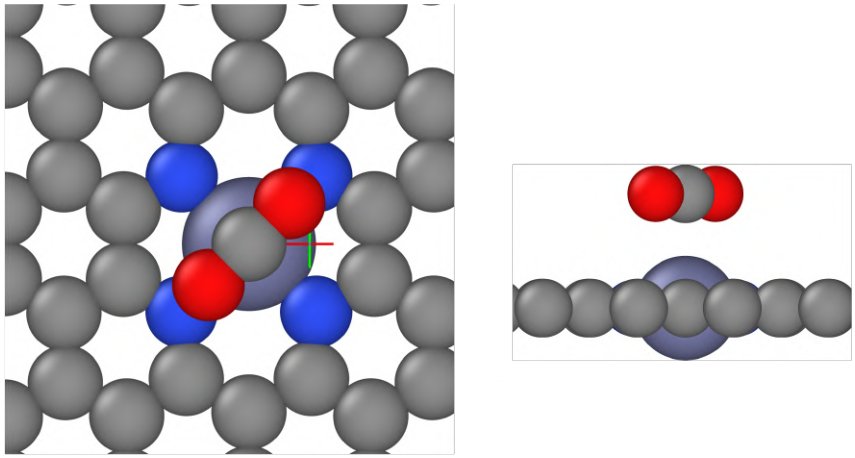

Figure D.5: Zn-N bridge $E_{ads} = -0.175$ eV

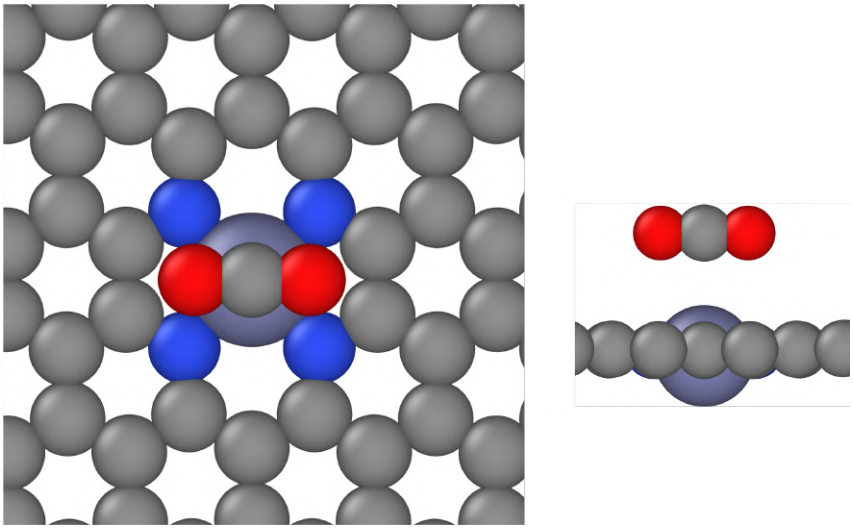

Figure D.6: Zn parallel $E_{ads} = -0.188$ eV

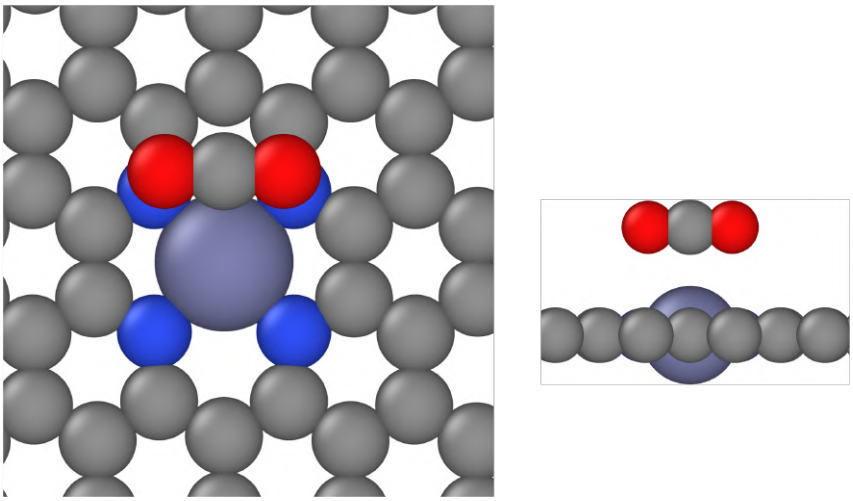

Figure D.7: H1 parallel $E_{ads} = -0.201$ eV

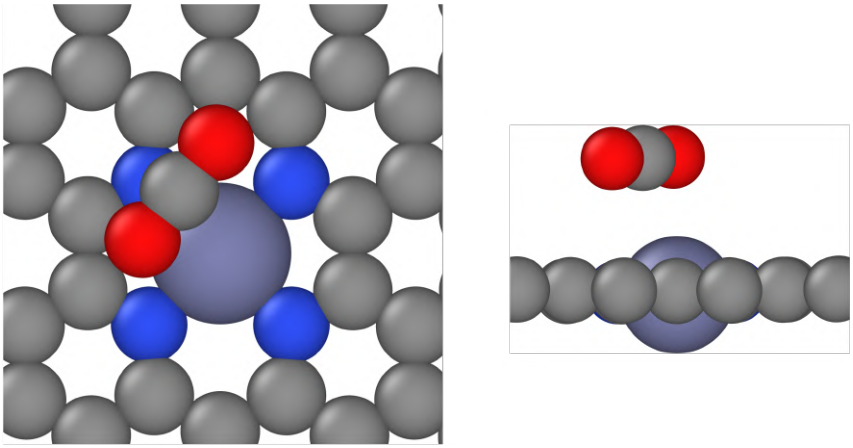

Figure D.8: H-aligned $E_{ads} = -0.206$ eV

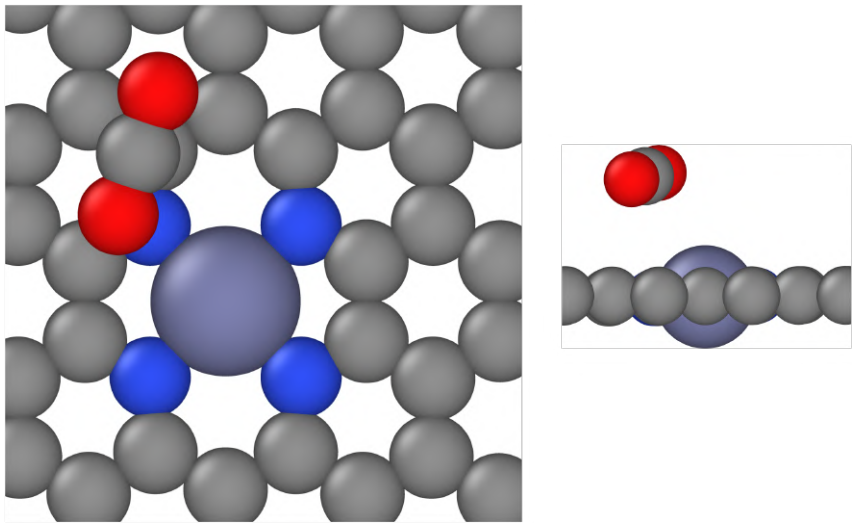

Figure D.9: C1 perp. $E_{ads} = -0.210$ eV

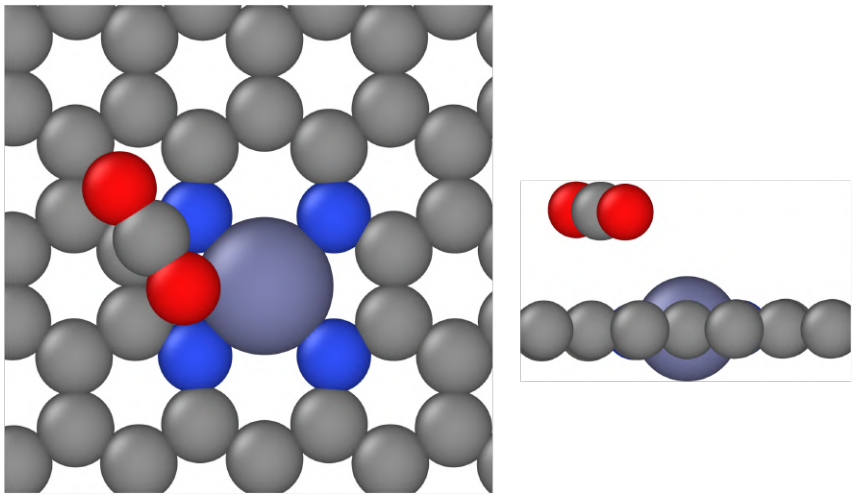

Figure D.10: H2 parallel $E_{ads} = -0.223$ eV

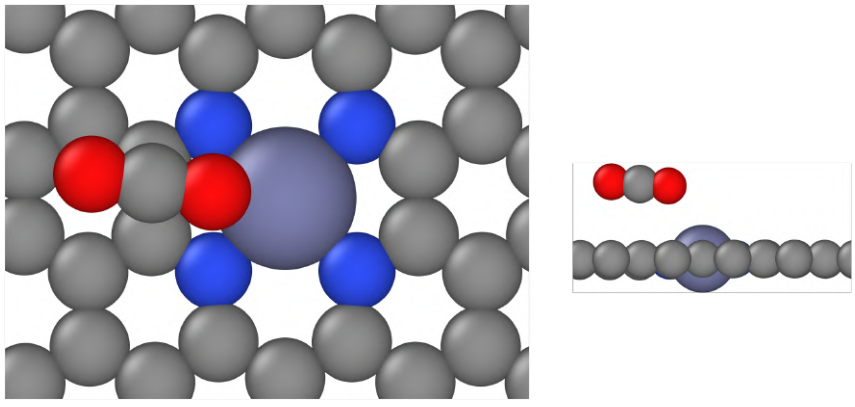

Figure D.11: C2 parallel $E_{ads} = -0.228$ eV

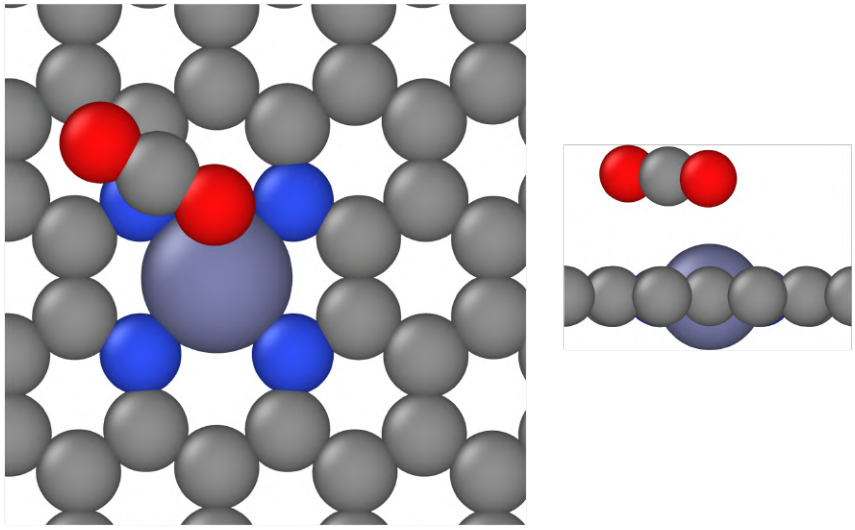

Figure D.12: C1 parallel $E_{ads} = -0.229$ eV

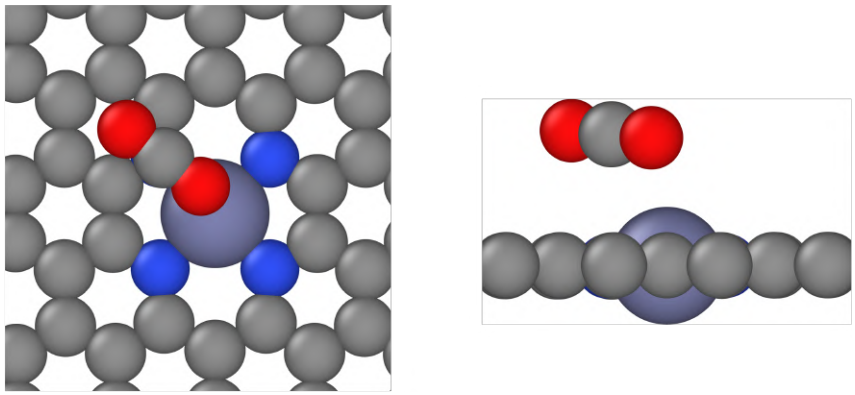

Figure D.13: N parallel $E_{ads} = -0.237$ eV

E | Adsorption Sites: Porphyrin-like

Illustrations of the adsorption sites of CO_2 in the porphyrin-like structure are reported. For each site we present top and side views of the two-dimensional sheet side by side. The order will follow adsorption energy as reported in Table 5.2.

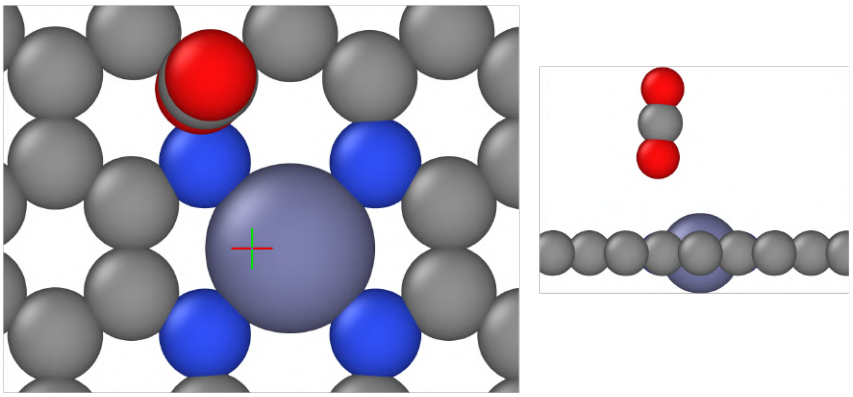

Figure E.1: C1 perp. $E_{ads} = -0.069$ eV

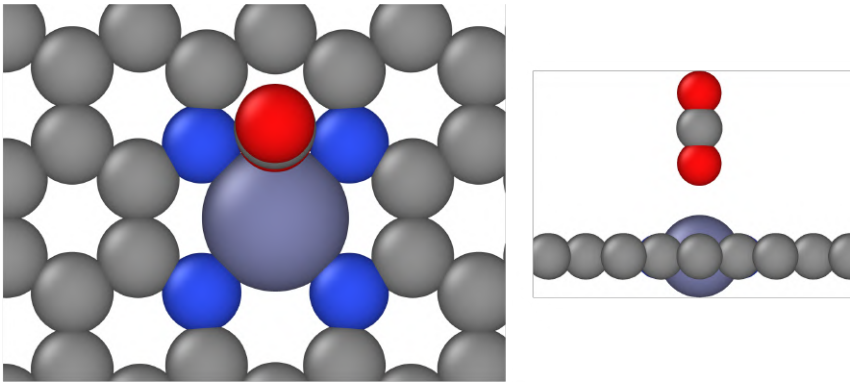

Figure E.2: H1 perp. $E_{ads} = -0.076$ eV

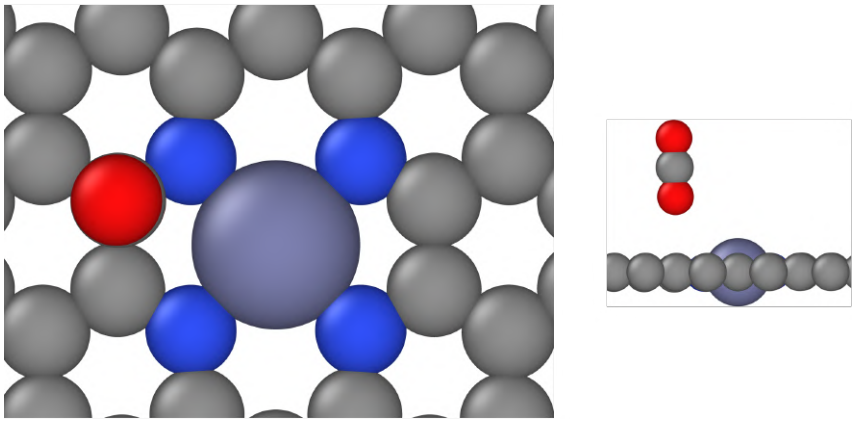

Figure E.3: C2 perp. $E_{ads} = -0.076$ eV

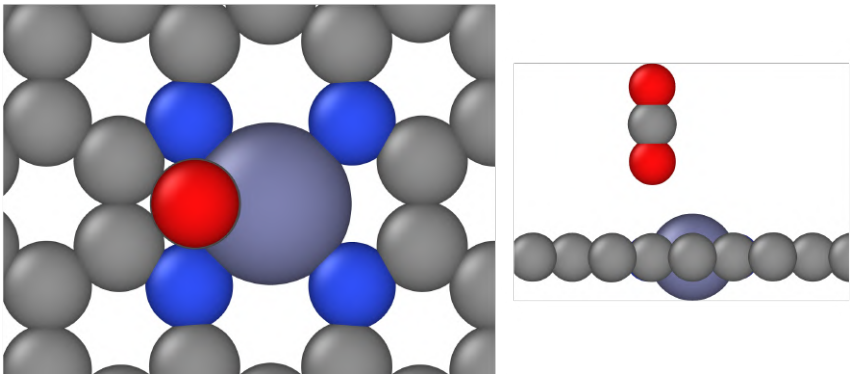

Figure E.4: H2 perp. $E_{ads} = -0.084$ eV

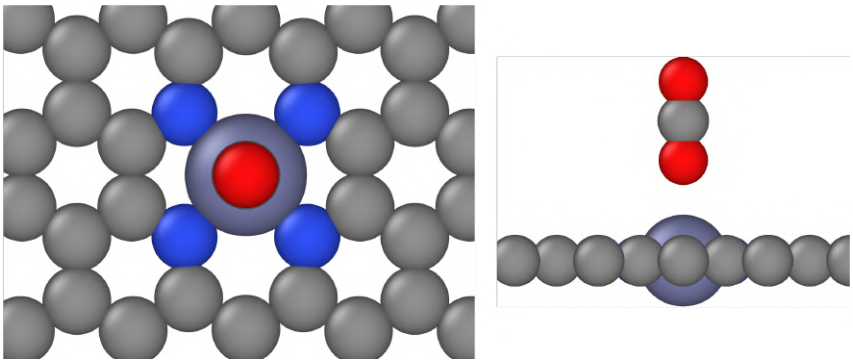

Figure E.5: Zn perp. $E_{ads} = -0.089$ eV

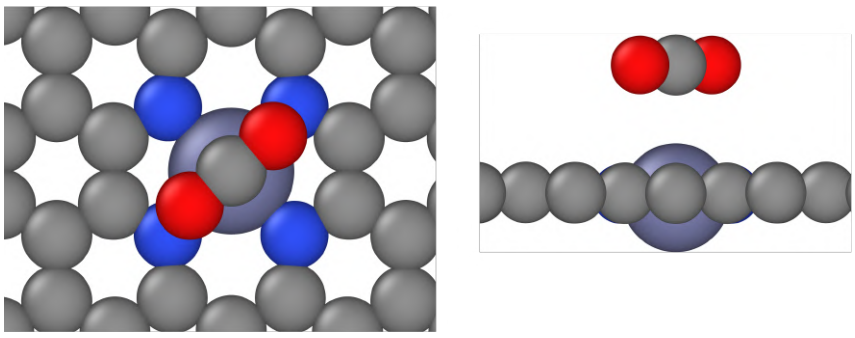

Figure E.6: Zn-N bridge $E_{ads} = -0.103$ eV

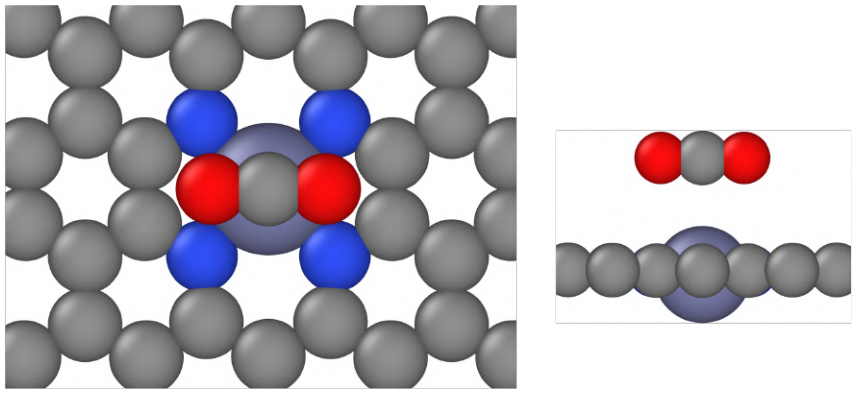

Figure E.7: Zn parallel $E_{ads} = -0.114$ eV

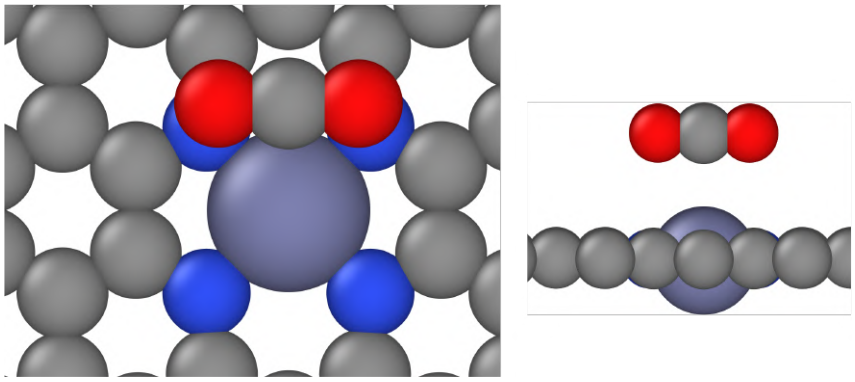

Figure E.8: H1 parallel $E_{ads} = -0.129$ eV

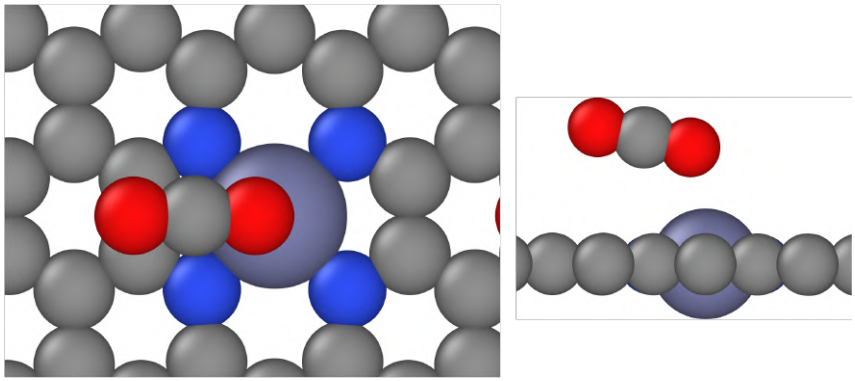

Figure E.9: H2 parallel $E_{ads} = -0.150$ eV

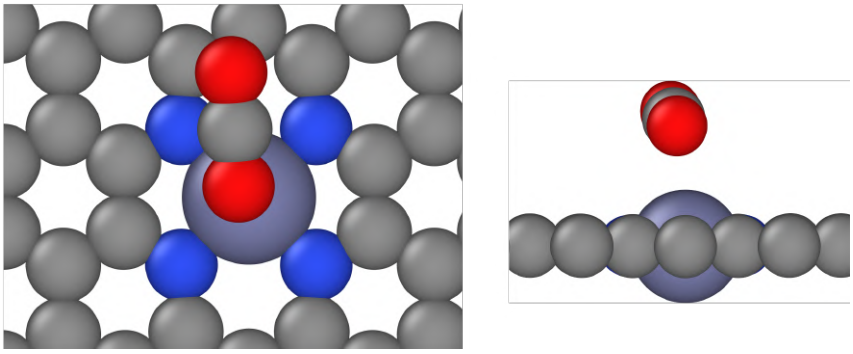

Figure E.10: H-aligned $E_{ads} = -0.152$ eV

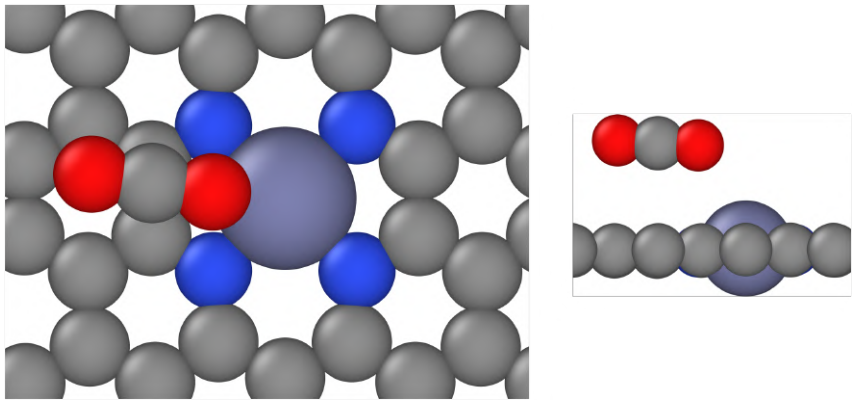

Figure E.11: C2 parallel $E_{ads} = -0.160$ eV

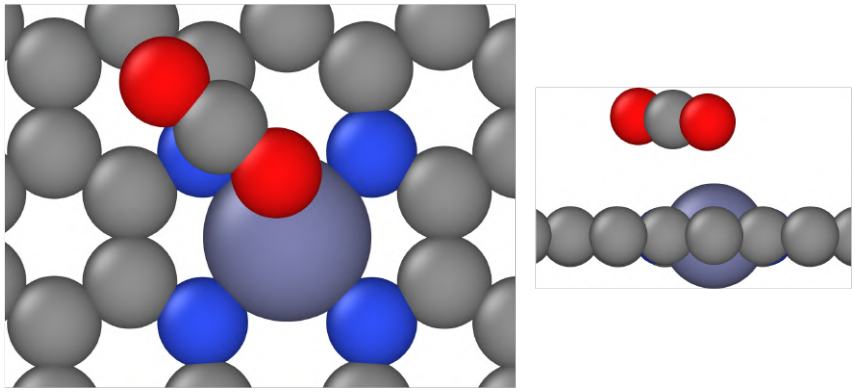

Figure E.12: C1 parallel $E_{ads} = -0.162$ eV

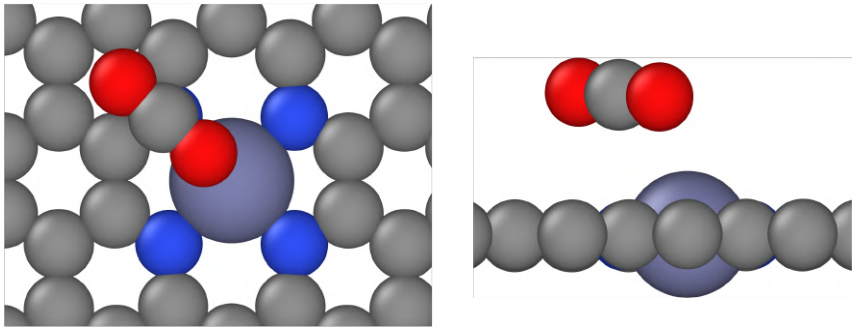

Figure E.13: N parallel $E_{ads} = -0.169$ eV